SCUOLA NORMALE SUPERIORE

Classe di Scienze

Corso di perfezionamento in Fisica

XXXVI ciclo

Electromagnetic Surface Waves at Anisotropic Interfaces: From Metamaterials to Fractional Quantum Hall Systems

Settore Scientifico Disciplinare FIS/03

Candidato
Daniele Battesimo PROVENZANO

Relatore

Prof. Giuseppe Carlo LA ROCCA

Anno accademico 2025/2026

Contents

Chapter 1

Introduction

1.1 Overview of Metamaterials and Plasmonics in the New Millennium

At the end of the twentieth century, it was widely believed that the electromagnetic phenomena derivable from Maxwell's equations had been exhaustively explored. Classical electrodynamics seemed a mature and complete theory, and the prospect of discovering fundamentally new optical effects appeared remote. However, the dawn of the new millennium revealed a striking reversal of this view. Advances in nanofabrication, materials science, and theoretical modeling uncovered that by structuring matter on scales comparable to or smaller than the wavelength of light, it was possible to engineer electromagnetic responses far beyond those found in nature. Out of this realization emerged the modern fields of *metamaterials* and *plasmonics*—disciplines that redefined the boundaries of light–matter interaction and inaugurated a new era of optics.

One of the first theoretical milestones was the 2000 paper by John B. Pendry entitled *Negative Refraction Makes a Perfect Lens*, in which a slab of material with negative refractive index was proposed to refocus not only propagating waves but also evanescent components, thereby overcoming the classical diffraction limit of imaging [Pendry, 2000]. This work built on earlier conceptual analysis of left-handed media by Veselago [Veselago, 1968], but the paper by Pendry served as a trigger for intense research in the domain of engineered materials with negative permittivity and/or permeability [Smith, Pendry, and Wiltshire, 2004].

In the early 2000s, experimental demonstrations of negative index behavior at microwave frequencies using split-ring resonators and conducting wires confirmed many of the predictions, initiating a wave of work extending the concept to terahertz, infrared and even visible frequencies [Smith, Pendry, and Wiltshire, 2004]. Parallel to these developments, the field of plasmonics, which studies the coupling of electromagnetic waves to collective electron oscillations in metals, matured into a prominent research area—facilitating ultra-tight confinement of light, strong field enhancement, and subwavelength phenomena [Halas, 2010].

During this period, metamaterials evolved from initial proof-of-concept negative-index designs into broader classes: for example, (bi-)anisotropic metamaterials,

hyperbolic metamaterials (with indefinite permittivity tensors), and epsilon-near-zero (ENZ) metamaterials. At the same time, plasmonics attracted much interest in both fundamental and applied directions: from novel nano-antenna structures, enhanced spectroscopy (e.g., surface-enhanced Raman scattering), to guiding and concentration of light at the nanoscale [Stockman, 2011].

A second wave of metamaterial research focused on imaging and sensing devices: the *superlens* concept was extended to metal-film superlenses, hyperlenses, and anisotropic metamaterial slabs enabling enhanced resolution or canalization of evanescent waves [Kim, 2015]. Simultaneously, plasmonic metamaterials emerged: hybrid systems leveraging both plasmonic resonances and metamaterial structure to tailor dispersion, enhance spontaneous emission, and control light–matter interaction at the nanoscale [Wang, Zhang, and Sun, 2022].

More recently, around the 2010s and beyond, the emphasis shifted from only exotic electromagnetic parameter values to integration, tunability, low-loss design, passive and active metadevices, and coupling to other platforms: silicon photonics, 2D materials (such as graphene), and quantum emitters. Thus, the new millennium has seen metamaterials and plasmonics evolve from curiosity-driven physics into more application-oriented directions and system integration.

The capabilities introduced by metamaterials and plasmonics have enabled new functionalities in imaging, sensing, light–matter interaction, wave-guiding, and signal processing. For imaging, the essential enabler has been the ability to manipulate both propagating and evanescent components, thereby enabling sub-diffraction imaging via superlenses or hyperlenses, as well as novel flat-optics and metasurface implementations [Kim, 2015]. In sensing, plasmonic resonances provide high local field enhancements and strong dependence of resonant frequency or phase on the surrounding environment's refractive index, enabling highly sensitive label-free biosensing, refractometry, and surface-enhanced spectroscopy.

Wave-guiding and routing at subwavelength scales is another key domain: plasmonic waveguides, metamaterial waveguides (including anisotropic and hyperbolic media), and metamaterial-based antennas have allowed miniaturized photonic circuits and enhanced coupling of light to nanoscale emitters. Moreover, metamaterials have enabled engineered Purcell enhancements, leading to high spontaneous-emission rates (important for quantum optics and nanolasers) especially via hyperbolic metamaterials with high photonic density of states.

Emerging directions include the integration of tunability and dynamic control (via phase-change materials, graphene, micro-electromechanical systems), topological photonics and non-reciprocal metamaterials, machine-learning-driven inverse design, and the merging of plasmonics/metamaterials with quantum technologies, 2D materials, biosystems and energy-harvesting platforms [Ali, Mitra, and Aïssa, 2022]. For example, the design of metamaterials for wireless power transfer (using magnetic superlenses) or for cloaking and transformation optics show that engineered electromagnetic response may serve for applications beyond classical optics [Lipworth et al., 2014].

In the domain of anisotropic media and photonic crystals, metamaterial and plasmonic concepts have been extended to layered and lattice-structured media. Hyperbolic metamaterials, anisotropic slabs, and engineered photonic crystals now allow canalization, high-k propagation, enhanced spontaneous emission and novel imaging/sensing modalities. These developments tie directly into the scope of the present work, which examines anisotropic slab-based metamaterials and their interface modes and dispersion.

As research continues, critical challenges remain: balancing confinement and loss, achieving broadband and low-loss operation at optical frequencies, scaling fabrication, and integrating into mainstream photonic platforms. Nonetheless, the progress of the last two decades promises an increasingly mature toolbox for controlling light and electromagnetic waves in engineered media.

1.2 Thesis Context and Structure

Within the broader landscape of modern photonics and metamaterial research, the work presented in this thesis situates itself at the intersection of anisotropic media, gyrotropy, and surface-wave physics. The central goal is to investigate how material anisotropy—when combined with magnetically induced nonreciprocity—can give rise to unconventional electromagnetic phenomena, such as unidirectional surface-wave propagation, tunable dispersion, and enhanced light confinement at subwavelength scales. These effects not only deepen the theoretical understanding of structured media but also open pathways toward new photonic devices where directionality, control, and miniaturization are key.

Following the historical developments of plasmonics and metamaterials outlined in the previous section, the remainder of this **introductory chapter** provides an overview of the main ingredients and physical systems involved in this thesis: hyperbolic media, gyrotropic media, photonic crystals, and electromagnetic surface waves. Each of these plays a distinct role in mediating the propagation, confinement, and symmetry properties of electromagnetic fields, and together they form the conceptual foundation upon which the subsequent chapters are built.

Chapter 2 establishes the theoretical framework required for understanding electromagnetic wave behavior in complex media. It begins by discussing the role of constitutive functions in macroscopic electrodynamics, emphasizing how their mathematical structure is constrained by universal physical symmetries such as time-reversal invariance, reciprocity, and energy conservation. Building upon these principles, the chapter develops a symmetry-based classification scheme that encompasses isotropic, anisotropic, and bi-anisotropic materials, offering a unified description of their electromagnetic response. The latter part of the chapter applies this framework to two original configurations designed to explore the interplay between reciprocity and energy conservation in surface-wave systems. The first configuration supports bidirectional propagation despite local energy imbalance,

while the second exhibits strictly unidirectional modes. Remarkably, both cases demonstrate that global energy conservation can be maintained under specific symmetry conditions. These examples provide a conceptual bridge between the general theory of constitutive relations and the practical realization of nonreciprocal surface phenomena.

Chapter 3 focuses on electromagnetic surface waves arising at interfaces and multilayered systems that combine gyrotropic and hyperbolic media. The coexistence of anisotropy and gyrotropy gives rise to new families of nonreciprocal surface modes characterized by directional energy flow, tilted field profiles, and tunable dispersion relations. Analytical derivations supported by numerical simulations reveal the conditions for their existence and demonstrate how their propagation can be dynamically controlled through an external magnetic field [Provenzano and La Rocca, 2023]. In addition to single-interface geometries, the chapter extends the analysis to one-dimensional photonic crystals composed of alternating gyroelectric and uniaxial layers. These periodic systems host hybrid surface and bulk states with adjustable group velocities—ranging from forward to backward propagation—depending on the degree of gyrotropy and the structural parameters. The resulting photonic band structure exhibits magnetically controllable gaps and surface-localized modes, providing a versatile platform for studying nonreciprocal light transport in anisotropic media [Provenzano and La Rocca, 2024].

Chapter 4 takes a forefront research system—a two-dimensional electron gas (2DEG) in the fractional quantum Hall (FQH) regime—as a case study to demonstrate how a fully microscopic quantum description can be translated into the macroscopic electromagnetic response functions employed throughout the previous chapters. Working in the lowest Landau level, the chapter develops a quadrupole–optical framework to investigate the collective excitations of the 2DEG, and connects long-wavelength density correlations to a neutral spin-2 "graviton" mode carrying a chiral quadrupole moment. The quantum description is then recast into the language of classical electrodynamics by extracting an effective, nonlocal susceptibility tensor that exhibits a gyrotropy-like in-plane structure and explicit spatial dispersion, thus linking microscopic graviton physics to macroscopic electromagnetic response. The emergence of spatial dispersion is particularly instructive, as it shows how internal geometric degrees of freedom in a strongly correlated quantum fluid manifest themselves as nonlocal constitutive relations at the classical level. Building on this microscopic-to-macroscopic mapping, Chapter 4 then proposes minimal cavity–electrodynamics setups designed to excite and detect the graviton through measurable shifts in the cavity eigenfrequencies. A perturbative estimate of the cavity shift reveals how the response scales with geometry and linewidth, thereby outlining practical routes to observation and providing design principles for resonant architectures that interface chiral quadrupole excitations with photonic modes. Since the theory of the fractional quantum Hall effect is conceptually distinct from the plasmonic and metamaterial themes developed in the previous chapters, no detailed introduction will be given at this stage. Instead, a dedicated overview of

the FQH framework will be presented at the beginning of Chapter 4.

Chapter 5 collects the main conclusions of the thesis and discusses the broader implications of the results, together with an outlook on possible future developments.

1.3 Anisotropic Media

Anisotropic media are materials whose electromagnetic response depends on the direction of the applied electromagnetic field. Unlike isotropic materials, characterized by a scalar permittivity ϵ and permeability μ, anisotropic media are described by second-rank tensors $\boldsymbol{\epsilon}$ and $\boldsymbol{\mu}$, which relate the electric displacement $\mathbf{D}$ and magnetic induction $\mathbf{B}$ to the electric and magnetic fields through

$$\mathbf{D} = \boldsymbol{\epsilon} \cdot \mathbf{E}, \qquad \mathbf{B} = \boldsymbol{\mu} \cdot \mathbf{H}.$$

As a result, the direction of $\mathbf{D}(\mathbf{H})$ is, in general, not parallel to that of $\mathbf{E}(\mathbf{B})$, leading to a range of rich optical phenomena such as birefringence, dichroism, and polarization-dependent propagation [Born and Wolf, 2019; Yariv and Yeh, 2002; Azzam and Bashara, 1977].

Anisotropic behaviors naturally occur in many crystalline solids and layered structures, but they can also be engineered artificially using metamaterials and photonic crystals. The ability to tailor the components of $\boldsymbol{\epsilon}$ and $\boldsymbol{\mu}$ has made anisotropy a powerful tool in modern photonics, enabling applications in polarization control [Saleh and Teich, 2019] and sub-diffraction imaging [Jacob, Alekseyev, and Narimanov, 2006; Liu et al., 2007].

In this thesis, the new results will be based exclusively on the electric response described by the dielectric tensor $\boldsymbol{\epsilon}$. However, in Chapter 2 the magnetic permeability $\boldsymbol{\mu}$ will also be considered, in order to discuss more general facts concerning electromagnetic symmetries.

1.3.1 Wave equation in anisotropic media

Consider an electromagnetic plane wave propagating through a homogeneous anisotropic medium along an arbitrary direction with respect to a given coordinate system. Let the wave vector be $\mathbf{k} = (k_x, k_y, k_z)$ and the associated electric and magnetic fields be

$$\mathbf{E}(\mathbf{r}, t) = \mathbf{E}_0 \, e^{i(\mathbf{k}\cdot\mathbf{r} - \omega t)} = \mathbf{E}_0 \, e^{i(k_x x + k_y y + k_z z - \omega t)}, \tag{1.1}$$

$$\mathbf{H}(\mathbf{r}, t) = \mathbf{H}_0 \, e^{i(\mathbf{k}\cdot\mathbf{r} - \omega t)} = \mathbf{H}_0 \, e^{i(k_x x + k_y y + k_z z - \omega t)}. \tag{1.2}$$

To determine the dispersion relation of the wave within the medium, Maxwell's equations should be written in the frequency domain. In the absence of sources, they

take the form

$$\begin{cases} \mathbf{k} \cdot \mathbf{D} = 0, \\ \mathbf{k} \cdot \mathbf{B} = 0, \\ \mathbf{k} \times \mathbf{E} = \omega\, \mathbf{B}, \\ \mathbf{k} \times \mathbf{H} = -\omega\, \mathbf{D}. \end{cases} \tag{1.3}$$

Combining Eq. (1.3) with the constitutive relations for an electrically anisotropic medium, one obtains the general wave equation

$$\sum_j \left[k^2 \delta_{ij} - k_i k_j - \frac{\omega^2}{c^2}\, \epsilon_{ij}(\omega) \right] E_j(\omega) = 0, \tag{1.4}$$

which can be expressed as the matrix equation

$$\begin{bmatrix} \epsilon_{xx}\frac{\omega^2}{c^2} - k_y^2 - k_z^2 & \epsilon_{xy}\frac{\omega^2}{c^2} + k_x k_y & \epsilon_{xz}\frac{\omega^2}{c^2} + k_x k_z \\ \epsilon_{yx}\frac{\omega^2}{c^2} + k_x k_y & \epsilon_{yy}\frac{\omega^2}{c^2} - k_x^2 - k_z^2 & \epsilon_{yz}\frac{\omega^2}{c^2} + k_y k_z \\ \epsilon_{zx}\frac{\omega^2}{c^2} + k_x k_z & \epsilon_{zy}\frac{\omega^2}{c^2} + k_y k_z & \epsilon_{zz}\frac{\omega^2}{c^2} - k_x^2 - k_y^2 \end{bmatrix} \begin{bmatrix} E_x \\ E_y \\ E_z \end{bmatrix} = 0. \tag{1.5}$$

Nontrivial solutions for the electric field exists only if the determinant of the coefficient matrix vanishes, leading to the so-called *Booker quartic*:

$$A\, k_z^4 + B\, k_z^3 + C\, k_z^2 + D\, k_z + E = 0, \tag{1.6}$$

where the five coefficients A, B, C, D, E depend on ϵ_{ij}, ω, k_x and k_y. The four solutions of this quartic equation represent the possible dispersion relations of plane electromagnetic waves that can propagate within the anisotropic medium. These solutions correspond to two forward and two backward-propagating modes, which is why anisotropic materials typically exhibit birefringence, as shown schematically in Fig. 1.1.[1]

Once the allowed k_z values are determined, substituting them into Eq. (1.5) yields the field components associated with each eigenmode. These solutions must satisfy the divergence condition

$$\sum_{i,j} k_i\, \epsilon_{ij}(\mathbf{k}, \omega)\, E_j(\mathbf{k}, \omega) = 0, \tag{1.7}$$

which follows directly from the first of Eq. (1.3). This theoretical framework forms the basis for the analysis developed throughout the entire thesis, serving as the foundation for understanding the electromagnetic response of all media involved.

[1] In isotropic media, the Booker quartic reduces to $(k_z^2 + \alpha)^2 = 0$, which has two double roots: $k_z = \pm\sqrt{-\alpha}$. In other words, the forward and backward propagation constants each have multiplicity two, so there is no splitting between different polarizations and birefringence does not occur in this case.

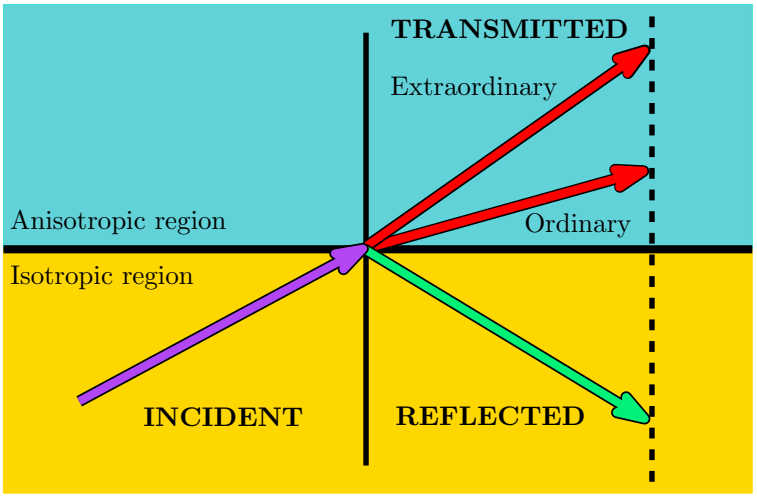

FIGURE 1.1: Schematic illustration of light refraction at the interface between an isotropic and an anisotropic medium. The incident beam generally splits into two transmitted rays, referred to as the ordinary and extraordinary waves.

1.4 Hyperbolic Metamaterials

Hyperbolic metamaterials (HMMs) constitute a remarkable class of artificial media that allow an unprecedented degree of control over the propagation of light at the nanoscale. Their unique property lies in the extreme anisotropy of their dielectric tensor, whose principal components have opposite signs. This configuration leads to an open hyperboloid dispersion relation, in contrast to the closed ellipsoidal isofrequency surface of ordinary anisotropic dielectrics. The resulting hyperbolic topology enables the propagation of electromagnetic modes with arbitrarily large momenta that would otherwise be evanescent in conventional media. By providing access to these high–wave vector modes, HMMs exhibit a broadband divergence of the photonic density of states (PDOS), which drastically modifies light–matter interactions. This property underlies a number of extraordinary optical phenomena such as negative refraction, sub-diffraction imaging, and large Purcell-factor enhancement of spontaneous emission. The conceptual significance of HMMs lies in their ability to engineer the dispersion relation of electromagnetic waves, thereby tailoring not just resonances but the very topology of the optical phase space. As such, they have emerged as a versatile platform for imaging, quantum photonics, and spontaneous emission control [Ferrari et al., 2014].

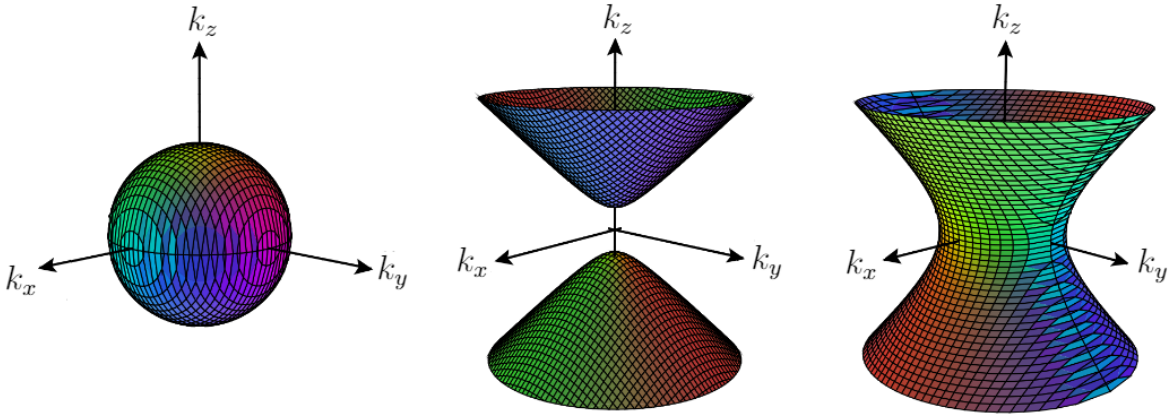

FIGURE 1.2: From left to right, examples of: spherical isofrequency surface relative to ordinary waves in uniaxial media; two-fold hyperboloid isofrequency surface for extraordinary waves in a Dielectric-Type HMM; one-fold hyperboloid isofrequency surface for extraordinary waves in a Metallic-Type HMM.

1.4.1 Basic electromagnetic description

Consider a uniaxial anisotropic medium described by the following dielectric tensor

$$\boldsymbol{\epsilon} = \begin{pmatrix} \epsilon_\perp & 0 & 0 \\ 0 & \epsilon_\perp & 0 \\ 0 & 0 & \epsilon_\parallel \end{pmatrix}. \tag{1.8}$$

In this case, Eq. (1.6) reduces to

$$\underbrace{\left(k_x^2 + k_y^2 + k_z^2 - \epsilon_\perp \frac{\omega^2}{c^2}\right)}_{TE-polarization\ (ordinary)} \underbrace{\left(\frac{k_x^2 + k_y^2}{\epsilon_\parallel} + \frac{k_z^2}{\epsilon_\perp} - \frac{\omega^2}{c^2}\right)}_{TM-polarization\ (extraordinary)} = 0. \tag{1.9}$$

If both $\epsilon_\perp, \epsilon_\parallel > 0$, then the two terms above correspond, respectively, to a spherical and an ellipsoidal isofrequency surface in the k-space. The first one describes ordinary waves, which are polarized in the xy plane (i.e. $E_z = 0$), hence the plane wave does not *feel* any anisotropy. Instead, the second one represents waves polarized in a plane containing the optical axis (extraordinary waves), characterized by $B_z = 0$. The situation changes substantially if we assume $\epsilon_\perp \epsilon_\parallel < 0$. As shown in Fig. 1.2, components with opposite sign result in a hyperboloidal isofrequency surface, hence media characterized by this feature are called *hyperbolic (meta)materials*.[2] As a consequence, there exist extraordinary waves with arbitrarily large wave vectors that have a propagating nature [Poddubny et al., 2013; Jacob et al., 2010], whereas

[2] In this thesis, in addition to discussing hyperbolic metamaterials, we will occasionally refer to *hyperbolic media* to indicate generic materials exhibiting hyperbolic dispersion, without specifying whether they are natural or artificially engineered.

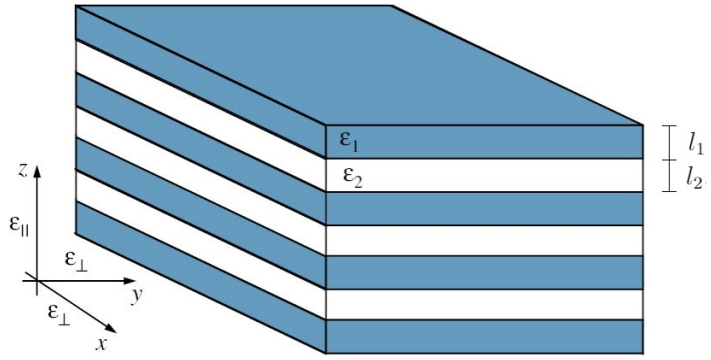

FIGURE 1.3: Outline of a ML structure used to realize a HMM.

in ordinary isotropic materials they would be evanescent because of the bounded isofrequency surface. There are two different kinds of (uniaxial) HMMs:

- **Dielectric** (or "Type 1 HMMs") if $\epsilon_\perp > 0$ and $\epsilon_\parallel < 0$, which correspond to a two-fold hyperboloid in the k-space;
- **Metallic** (or "Type 2 HMMs") if $\epsilon_\perp < 0$ and $\epsilon_\parallel > 0$, which correspond to a one-fold hyperboloid in the k-space.

Typical artificial realizations of HMMs include metal–dielectric multilayers and metallic nanowire arrays [Ferrari et al., 2014]. Their behavior can be accurately modeled using effective medium theory (EMT) when the period of the composite structure is much smaller than the operating wavelength [Sihvola, 1999]. However, for realistic geometries, deviations from EMT may arise due to spatial dispersion, nonlocal effects, and losses [Kidwai, Zhukovsky, and Sipe, 2012].

For a periodic multilayer of thicknesses l_1, l_2 and permittivities ϵ_1, ϵ_2 (interfaces normal to z), such as the one shown in Fig. 1.3, homogenization at scales $d \gg l_1 + l_2$ yields a uniaxial tensor with in-plane arithmetic average and out-of-plane harmonic average:

$$\epsilon_\perp = \epsilon_{xx} = \epsilon_{yy} = (1-f)\,\epsilon_1 + f\,\epsilon_2, \qquad \epsilon_\parallel = \epsilon_{zz} = \frac{1}{(1-f)/\epsilon_1 + f/\epsilon_2}, \tag{1.10}$$

where $f = l_2/(l_1 + l_2)$ is the fill fraction [Ferrari et al., 2014]. Choosing a dielectric $\epsilon_d > 0$ and a dispersive metal $\epsilon_m(\omega) < 0$ (e.g. described by a Drude model) allows $\epsilon_\perp$ and $\epsilon_\parallel$ to assume opposite signs over broad spectral and geometric ranges, realizing type-I or type-II hyperbolic response [Kidwai, Zhukovsky, and Sipe, 2012], as shown in Fig. 1.4(b). Outside those ranges, the same stack behaves as an effective dielectric ($\epsilon_\perp, \epsilon_\parallel > 0$) or an effective anisotropic metal ($\epsilon_\perp, \epsilon_\parallel < 0$).

Metal–dielectric multilayers, typically based on Ag/Al_2O_3 or Au/SiO_2, are the most widely used artificial HMMs in the visible and near-infrared ranges. They are compatible with established fabrication techniques but suffer from Ohmic losses and fabrication-induced roughness. Nanowire composites provide an alternative

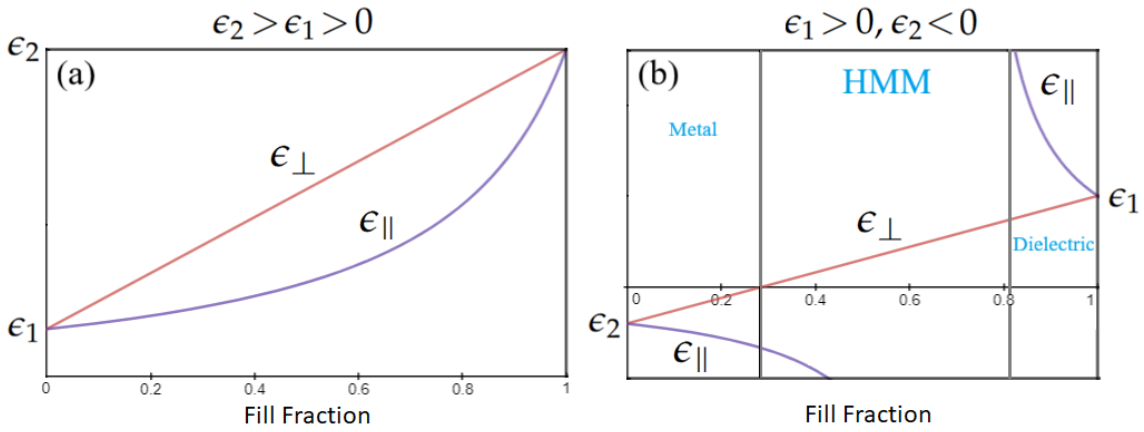

FIGURE 1.4: Permittivities of the ML structure as a function of the fill fraction f. (a) Case $\epsilon_2 > \epsilon_1 > 0$, describing an uniaxial dielectric. (b) Case $\epsilon_1 > 0$, $\epsilon_2 < 0$, with three different scenarios.

geometry that can achieve similar optical responses with different field distributions and tunability.

In addition to artificial composites, several natural crystals, such as hexagonal boron nitride (hBN), exhibit hyperbolic dispersion in specific spectral regions associated with phonon polaritons, offering an intrinsically low-loss platform for mid-infrared applications [Caldwell et al., 2014; Dai et al., 2015].

1.4.2 Wave propagation, high-k modes and negative refraction

As mentioned above, the open hyperboloid dispersion of HMMs allows coupling to electromagnetic modes with very large in-plane momenta, which are evanescent in free space. These high-k modes are associated with a broadband divergence of the photonic density of states, enhancing light–matter interactions in ways that are not limited to narrow resonances [Jacob et al., 2010]. A prominent experimental manifestation of this behavior is the optical topological transition, where a change in the sign of one tensor component leads to an abrupt modification of the local density of states and of the spontaneous emission lifetime of emitters placed near the metamaterial [Krishnamoorthy et al., 2012].

Design trade-offs include managing absorption losses, optimizing out-coupling of high-k modes, and ensuring that emitters or analytes are positioned within the near-field region where hyperbolic dispersion dominates. For spontaneous emission engineering, the emitter–surface separation must be carefully controlled to maximize radiative enhancement while minimizing quenching.

Another striking feature of HMMs is the capability of supporting *negative refraction*. When an electromagnetic wave impinges on an interface between an isotropic medium and a hyperbolic metamaterial, the Poynting vector and the wave vector can refract in opposite directions, as illustrated in the left panel of Fig. 1.5. This phenomenon enables beam steering and canalization effects similar to those that occur in isotropic negative-index media, but without requiring both permittivity

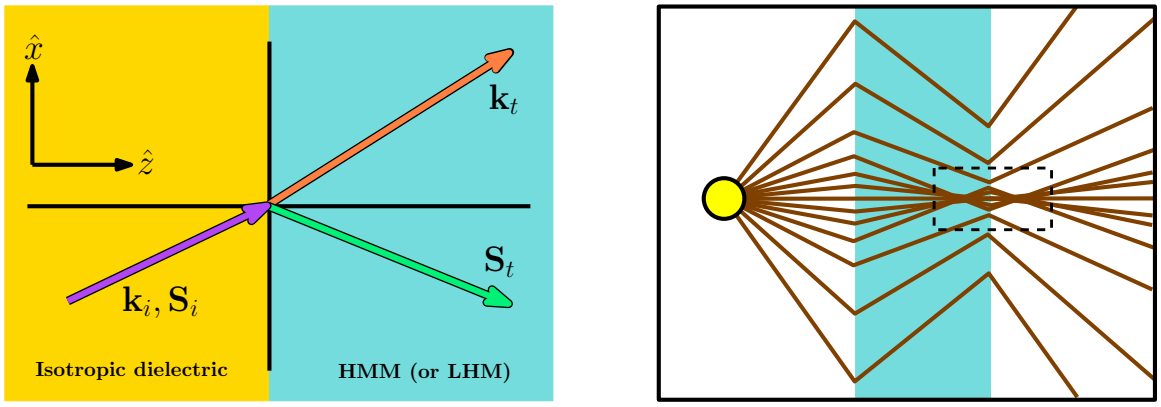

FIGURE 1.5: (*Left*) Schematic illustration of the refraction of the wave vector and the Poynting vector at the interface with a hyperbolic medium. (*Right*) Focusing of the rays emitted by a light source through a slab of hyperbolic material.

and permeability to be negative [Smith and Schurig, 2004]. As a consequence, a hyperbolic metamaterial slab can partially focus radiation, as shown in the right panel of Fig. 1.5, in a way closely analogous to the mechanism introduced by Pendry in his seminal work on perfect lenses [Pendry, 2000].

Experimental observations of broadband negative refraction have been reported using vertically aligned hyperbolic metamaterials operating across the visible spectrum [Cho et al., 2021; Bang, So, and Rho, 2019].

1.4.3 Hyperlensing and spontaneous emission control

The ability of HMMs to transform evanescent waves into propagating modes provides the basis for the concept of optical hyperlens. A hyperlens consists of a curved or cylindrical shell of a hyperbolic medium that converts subwavelength spatial information into propagating waves observable in the far field. This concept was first introduced theoretically in [Jacob, Alekseyev, and Narimanov, 2006] and was later demonstrated experimentally by Liu et al., who achieved the imaging of 150 nm features using a multilayered silver-alumina structure at visible wavelengths [Liu et al., 2007].

Unlike near-field superlenses that rely on surface plasmon resonances, hyperlenses exploit the propagation of high-k bulk modes, allowing for far-field operation and magnification of subwavelength features. The extension of this concept to natural hyperbolic materials, such as hBN, has enabled low-loss hyperlensing and sub-diffraction imaging in the mid-infrared spectral range through phonon-polariton modes [Caldwell et al., 2014; Dai et al., 2015; Li et al., 2015].

The large photonic density of states in HMMs leads to broadband enhancement of spontaneous emission rates. The Purcell factor, which measures the spontaneous emission rate relative to that in free space, can reach very high values due to the continuum of accessible high-k modes. Theoretically, the Purcell factor diverges in

the lossless, local EMT limit, though in practice it is limited by absorption, nonlocal response, and finite structural periodicity [Kidwai, Zhukovsky, and Sipe, 2012]. Experimental studies have confirmed large enhancements of emission rates and broadband modification of emitter lifetimes near metal–dielectric HMMs [Krishnamoorthy et al., 2012; Slobozhanyuk et al., 2015]. Optimized nanorod or multilayer geometries can balance radiative and nonradiative channels to achieve strong coupling and enhanced radiative yield.

1.5 Gyrotropic Media

Gyrotropy is the property of a medium in which the electromagnetic response becomes directionally dependent in a handed or rotationally asymmetric way, leading to effects such as optical rotation or circular birefringence. In gyrotropic media, $\boldsymbol{\epsilon}$ or $\boldsymbol{\mu}$ (or both) contain antisymmetric components responsible for rotation of the polarization or time-reversal symmetry breaking.

To avoid confusion with other sources, it is important to recall that throughout the historical development of electromagnetic theory in media, the term *gyrotropy* has often been used with different meanings, sometimes as a synonym for *magneto-optic effects*, *optical activity*, or even to describe *magnetoelectric coupling* in bianisotropic materials [Serdyukov et al., 2001b]. This has led to some ambiguity, with identical names being used to denote distinct effects and, conversely, different names referring to the same phenomenon.

In this thesis, we will consider only the form of gyrotropy associated with the anisotropy of the dielectric tensor $\boldsymbol{\epsilon}$, disregarding the magnetoelectric coupling characteristic of bianisotropic media and the effects related to the magnetic permeability tensor $\boldsymbol{\mu}$.

Furthermore, since this introductory section discusses both cases, we will distinguish between gyrotropy induced by external magnetic biases—here referred to as *induced gyrotropy*—and the one arising from intrinsic structural chirality, denoted as *natural gyrotropy* (also known as *natural optical activity*). In all subsequent chapters, any gyrotropic medium mentioned will be understood to exhibit induced gyrotropy, as natural gyrotropy will not be treated further.

1.5.1 Induced gyrotropy vs. natural gyrotropy

A typical example of induced gyrotropy arises in magneto-optic materials subject to a static magnetic bias $\mathbf{B}_{\text{ext}}$, where the permittivity tensor takes the form

$$\boldsymbol{\epsilon} = \begin{pmatrix} \epsilon & ig & 0 \\ -ig & \epsilon & 0 \\ 0 & 0 & \epsilon_z \end{pmatrix}, \tag{1.11}$$

with g the gyration parameter proportional to the external magnetic field, which in this case is oriented along $\hat{z}$. If $\mathbf{B}_{\text{ext}}$ is reversed, g changes sign. In such media, right- and left-circularly polarized eigenmodes propagating along the direction of the magnetic bias experience different refractive indices $n_{\pm}$, resulting in a rotation of the polarization plane by a certain angle, known as the Faraday effect [Zvezdin and Kotov, 1997; Landau and Lifshitz, 1984]. Another important configuration is the Voigt configuration, where the magnetic bias is perpendicular to the propagation direction. In this case, the eigenmodes are linearly polarized, and one observes linear birefringence and dichroism instead of circular birefringence. These behaviors are at the heart of gyrotropic phenomena and can be described within the same theoretical framework [Zvezdin and Kotov, 1997].

As will be discussed in more detail in Chapter 2, the presence of the external magnetic field breaks time-reversal symmetry and renders the system nonreciprocal. In this case, the rotation is nonreciprocal: its sense does not change when the propagation direction is reversed, as shown in Fig. 1.6(a), since it is fixed by the orientation of the magnetic field rather than by the wave vector. This makes such kind of gyrotropic media fundamental for realizing optical isolators, nonreciprocal devices that allow light transmission in one direction while blocking it in the opposite, essential, for instance, in protecting laser sources from back-reflected light.

In contrast, in naturally gyrotropic media, such as chiral crystals or optically active molecules, gyrotropy originates from structural asymmetry rather than from an external magnetic field. The dielectric response depends on the direction of propagation [Prosandeev et al., 2013], and the polarization rotation reverses when the light path is reversed, making the effect reciprocal, as illustrated in Fig. 1.6(b).

This form of gyrotropy has been known since the early nineteenth century and arises microscopically from coupling between electric-dipole, magnetic-dipole, and electric-quadrupole transitions [Landau and Lifshitz, 1984; Proskurin et al., 2017]. Recent theoretical developments have clarified the connection between natural optical activity, electromagnetic chirality, and the conservation of optical helicity, emphasizing the symmetry principles underlying reciprocal gyrotropy [Proskurin et al., 2017].

Induced and natural gyrotropy represent two distinct yet complementary manifestations of optical rotation. The distinction between them has important implications for the design of optical isolators and polarization-control devices [Jalas et al., 2013].

1.5.2 Experimental examples

Natural gyrotropy has been experimentally observed in a variety of crystalline and molecular systems that possess structural chirality or lack inversion symmetry. Classic examples include quartz, tellurium, and sodium chlorate, which exhibit measurable rotation of the polarization plane even in the absence of an external magnetic field [Proskurin et al., 2017]. The sign and magnitude of the optical rotation

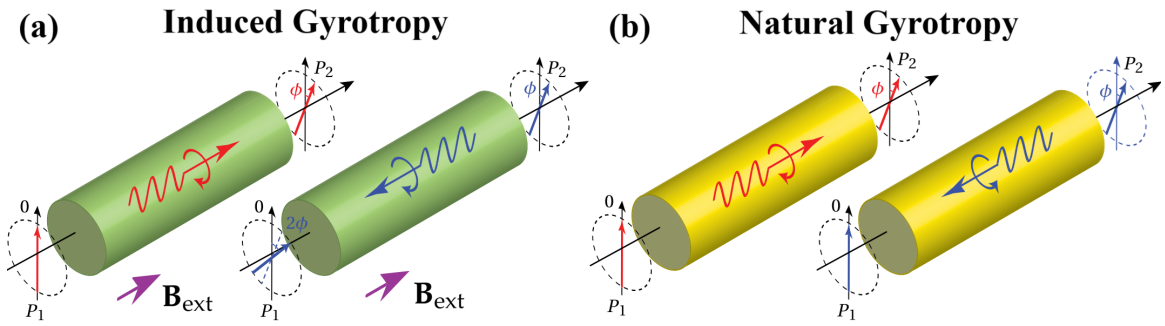

FIGURE 1.6: Difference between forward and backward propagation in media with (a) induced and (b) natural gyrotropy. In the first case, when the propagation direction is reversed, the sense of rotation does not change, and the polarization rotation angles accumulate with distance. In contrast, in naturally gyrotropic media, when the propagation direction is inverted, the sense of rotation also reverses, since it is linked to the wave vector **k**. As a result, the wave returns to its original polarization state. Figures are adapted from [Caloz et al., 2018].

depend on the handedness of the crystal lattice and on the propagation direction relative to the optical axis, allowing for the precise identification of enantiomorphs by polarimetric methods. In molecular solutions—such as those containing sugars, amino acids, or chiral organic molecules—the rotation per unit length depends on the concentration and wavelength and forms the basis of standard optical activity measurements and enantiomeric analysis in chemistry. More recently, chiral metamaterials and plasmonic nanostructures have been designed to reproduce and amplify natural optical activity at optical and near-infrared frequencies, offering controllable and enhanced polarization effects [Plum et al., 2009].

In the context of induced gyrotropy, ferromagnetic garnets remain the most important experimental platform. Yttrium iron garnet (YIG) and its bismuth or cerium-substituted variants exhibit a large rotation of polarization combined with low absorption losses, establishing them as benchmark materials for Faraday rotation experiments [Crossley and Day, 1969; Zvezdin and Kotov, 1997; Levy et al., 2019]. Thin films grown by liquid-phase epitaxy or sputtering achieve high crystalline quality and low optical scattering, while chemical substitution increases the gyration parameter and Verdet constant. Faraday rotation is typically measured with balanced polarimetry under variable magnetic bias, enabling the extraction of hysteresis loops and rotation–field dependencies [Levy et al., 2019].

In doped semiconductors and low-density plasmas, gyrotropy originates from free-carrier cyclotron resonances, producing strong rotation and ellipticity in the terahertz and infrared spectral regions [Zvezdin and Kotov, 1997]. These effects are probed experimentally using broadband terahertz time-domain spectroscopy or Fourier-transform infrared polarimetry, which also allow non-contact determination of carrier densities and mobilities. Two-dimensional materials, especially graphene, have shown giant field-tunable gyrotropy due to quantized cyclotron and inter-Landau-level transitions, with rotations of several degrees observed under

moderate magnetic fields in the terahertz and mid-infrared ranges [Crassee et al., 2011]. Artificially engineered metamaterials further enable the realization of effective gyrotropy without external magnetic bias, using controlled structural chirality and magnetoelectric coupling to emulate or enhance both natural and induced effects [Serdyukov et al., 2001a; Plum et al., 2009].

1.5.3 Applications

Gyrotropic media play a central role in modern photonics wherever polarization control and nonreciprocal light propagation are required. The most prominent example is the aforementioned optical isolator, which combines gyrotropy-induced polarization rotation with polarizers to ensure one-way transmission and suppression of back-reflected light. Related components include circulators, polarization rotators, and variable phase shifters. In integrated photonic platforms, thin films of Ce:YIG and related garnets have been incorporated into silicon and silicon nitride waveguides to realize chip-scale isolators and circulators [Srinivasan and Stadler, 2022]. Such devices are key to achieving robust, reflection-immune signal routing in on-chip optical communication systems.

Field-tunable gyrotropy in semiconductors and graphene enables compact modulators and sensors operating in the terahertz and infrared regimes. The ability to dynamically control the rotation angle through gate voltage or external bias opens possibilities for reconfigurable photonic components and magnetically controlled polarization converters [Crassee et al., 2011]. Natural gyrotropy, on the other hand, underpins polarimetric metrology and analytical chemistry, where the wavelength-dependent rotation serves as a sensitive probe of molecular chirality, crystalline handedness, and optical activity.

From a fundamental perspective, induced gyrotropy provides a practical route to break time-reversal symmetry in photonic structures, enabling unidirectional modes and nonreciprocal propagation analogous to electronic quantum Hall systems. In parallel, dispersion-engineered gyrotropic materials, both natural and artificial, offer enhanced control over polarization and group velocity, paving the way for compact, loss-optimized photonic devices with intrinsic directionality [Srinivasan and Stadler, 2022; Serdyukov et al., 2001a].

1.6 Photonic Crystals

Photonic crystals are structures in which the refractive index is periodically modulated on the scale of the optical wavelength. The spatial periodicity produces Bragg scattering for electromagnetic waves, giving rise to photonic band structures with allowed and forbidden frequency ranges, in direct analogy to electronic band structures in solids [Joannopoulos et al., 2008; Yablonovitch, 1987; John, 1987]. Depending on the dimensionality of the periodic modulation, photonic crystals

are commonly classified as one-dimensional (multilayers and Bragg mirrors), two-dimensional (periodic patterning in a slab or membrane), and three-dimensional (fully periodic in all spatial directions). When the refractive-index contrast and geometry are appropriate, complete photonic band gaps may form, forbidding propagation for all polarizations and directions within a finite frequency interval [Joannopoulos et al., 2008].

The dispersion relation of photonic crystals can be tailored by lattice constant, filling fraction, and refractive-index contrast, allowing phenomena such as slow light, superprism angular dispersion, supercollimation, and negative refraction within certain bands [Kosaka et al., 1998; Notomi, 2000; Russell, 2003]. Local modifications of the periodic lattice—by removing or altering rows of holes or rods—create line defects (waveguides) and point defects (nanocavities) that confine and guide light with mode volumes near the diffraction limit and quality factors that can exceed one million in carefully engineered designs [Akahane et al., 2003; Mekis et al., 1996]. Photonic crystal slabs, which employ two-dimensional in-plane periodicity combined with vertical index guiding, offer strong dispersion engineering in compact, planar geometries compatible with microfabrication [Painter et al., 1999].

The origin and significance of photonic band gaps were established in the seminal works of Yablonovitch and John, who showed that periodic dielectric structures can inhibit spontaneous emission and localize light in appropriately designed or disordered lattices [Yablonovitch, 1987; John, 1987]. Since then, the field has advanced from one-dimensional mirrors to sophisticated two- and three-dimensional architectures, including inverse-opal and woodpile structures with near-infrared band gaps fabricated by top-down lithography or bottom-up self-assembly [Noda et al., 2000]. In parallel, photonic crystal fibers extend the concept to waveguides with periodic microstructured claddings, enabling endless single-mode guidance, large-mode area designs, and strong light–matter interaction for sensing [Russell, 2003; Knight, 2003].

1.6.1 Experimental examples and applications in imaging and sensing

Experimentally, two-dimensional photonic crystal slabs in high-index materials such as silicon and III–V semiconductors have emerged as versatile platforms. Their in-plane periodicity and out-of-plane index guiding enable compact waveguides with sharp bends of low loss and high-Q point-defect nanocavities suitable for on-chip light sources, filtering, and nonlinear optics [Mekis et al., 1996; Akahane et al., 2003; Imada et al., 1999]. Three-dimensional structures, including fully periodic woodpile crystals and inverse-opal networks, have demonstrated band gaps in the near-infrared and the potential for embedding active emitters inside a photonic band-gap environment [Noda et al., 2000]. In fiber form, photonic-crystal claddings enable unique guidance regimes, dispersion control, and large overlap between guided modes and analytes for sensing [Russell, 2003; Knight, 2003].

In imaging, photonic crystals offer functionality distinct from traditional refractive optics. Angular dispersion in the superprism regime enables wavelength and angle separation with high sensitivity for compact spectrometers and beam steering [Kosaka et al., 1998]. Negative refraction within specific photonic bands has been used to demonstrate flat-lens focusing and imaging without bulk negative-index media, including microwave demonstrations of focusing and near-field simulations and experiments of subwavelength features in carefully engineered lattices [Notomi, 2000; Parimi et al., 2003; Luo et al., 2004]. Photonic crystal slabs further support guided-resonance effects that can enhance field confinement near the surface, a property that is exploited in surface-sensitive imaging and label-free biosensing.

In sensing, the high field confinement and sharp dispersive features of photonic-crystal defects translate into strong spectral responses to small refractive-index changes. Point-defect nanocavities with high quality factor and small mode volume have been used to realize label-free detection of biomolecules and gases; shifts in cavity resonance or changes in the transmission of line-defect waveguides provide the readout mechanism [Skivesen et al., 2007; Lee and Fauchet, 2007]. Two-dimensional photonic crystal slabs configured as guided-mode resonance sensors provide large surface fields and narrow spectral features, enabling compact, low-volume assays with multiplexed readout [Lee and Fauchet, 2007]. Photonic crystal fibers also serve as robust sensing platforms in which the microstructured cladding channels can be filled with liquids or gases, achieving long interaction lengths and high sensitivity for chemical and environmental monitoring [Russell, 2003; Knight, 2003].

In Chapter 3, we will analyze original configurations consisting of one-dimensional photonic crystals made of anisotropic slabs, investigating both their band structures and their allowed surface modes [Provenzano and La Rocca, 2024].

1.7 The Goos–Hänchen Effect

When a light beam with finite transverse extent and linear polarization impinges on a planar interface between two optical media under conditions of total internal reflection (TIR), the point at which the reflected beam emerges does not coincide with the geometrical point of incidence predicted by ray optics. Instead, the reflected beam undergoes a lateral displacement along the interface — a phenomenon known as the *Goos–Hänchen shift* (GHS). This effect, illustrated in Fig. 1.7, reveals the limitations of geometrical optics in describing beam behavior at interfaces and highlights the necessity of a wave-optical treatment.

The GHS was first observed experimentally by Fritz Goos and Hilda Hänchen in 1947 using a glass prism and thin-film interference techniques [Goos and Hänchen, 1947]. A quantitative theoretical description was later provided by Artmann [Artmann, 1948], who employed the stationary phase method to show that the lateral

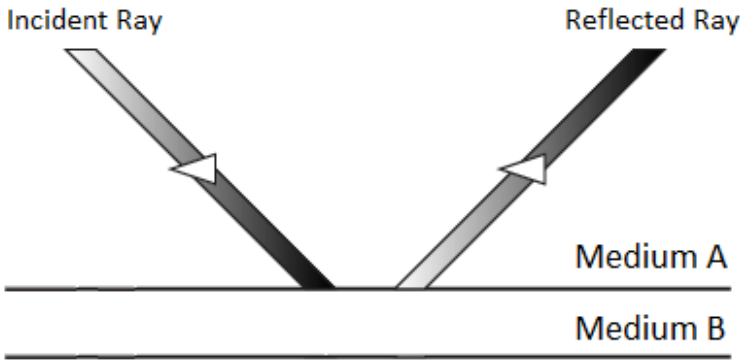

FIGURE 1.7: Schematic representation of the Goos–Hänchen shift at the interface between two media.

shift S_{GH} of the reflected beam is related to the derivative of the phase of the reflection coefficient:

$$S_{GH} = -\frac{\mathrm{d}\varphi}{\mathrm{d}k_{\parallel}}. \tag{1.12}$$

Here, φ is the phase of the complex reflection coefficient r, and $k_{\parallel}$ is the component of the wave vector parallel to the interface. For a slab of thickness d, the reflection coefficient can be expressed as

$$r(\omega, d, \theta) = |r(\omega, d, \theta)|\, e^{i\varphi(\omega,d,\theta)},$$

where the phase is expressed as

$$\varphi(\omega, d, \theta) = \mathrm{Im}\left[\log r(\omega, d, \theta)\right].$$

Assuming that the incident medium is isotropic with permittivity ϵ_1, the parallel component of the wave vector is

$$k_{\parallel} = \frac{\omega}{c}\sqrt{\epsilon_1}\sin\theta.$$

Substituting into Eq. (1.12) and applying the chain rule yields

$$\begin{aligned} S_{GH} &= -\frac{1}{(\omega/c)\sqrt{\epsilon_1}\cos\theta}\,\frac{\mathrm{d}\varphi}{\mathrm{d}\theta} \\ &= -\frac{\lambda_{\mathrm{inc}}}{2\pi\sqrt{\epsilon_1}\cos\theta}\,\frac{\mathrm{d}\ \mathrm{Im}[\log r]}{\mathrm{d}\theta}. \end{aligned} \tag{1.13}$$

This expression shows that the GHS depends critically on the angular dispersion of the reflection phase and becomes most pronounced near particular incidence angles. Two angular regimes are especially relevant:

- **Critical angle** ($\theta_c = \arcsin(n_2/n_1)$): beyond this angle, total internal reflection occurs and the reflection coefficient becomes complex. The rapid phase variation of r near θ_c produces a large lateral displacement.

- **Brewster angle**: for TM-polarized waves, the reflection coefficient vanishes at the Brewster angle ($|r_{TM}| \to 0$). Although the amplitude tends to zero, the phase of r undergoes a steep variation. In absorbing media, this condition is generalized as the pseudo-Brewster angle, since perfect zero reflection is not achieved [Lai and Chan, 2002].

Under ordinary conditions, the GHS is positive and typically on the order of the wavelength, $S_{GH} \sim \lambda$ [Artmann, 1948]. However, several studies have shown that the shift can also become negative. Negative GHS values have been reported, for example, at interfaces between conventional dielectrics and metamaterials with negative refractive index [Qing and Chen, 2004; Shadrivov, Sukhorukov, and Kivshar, 2003], or in lossy dielectric slabs near the pseudo-Brewster angle for TM polarization [Wang, Chen, and Zhu, 2005].

In certain configurations, the magnitude of the shift can exceed the wavelength by several orders of magnitude. These cases, referred to as giant Goos–Hänchen shifts (GGHS), occur when the phase of the reflection coefficient varies rapidly with angle or frequency, typically near resonant or dispersive conditions. GGHS have been demonstrated in multilayer systems, waveguide resonances, and photonic crystals, where interference and field localization effects greatly amplify the lateral displacement [He, Yi, and He, 2006; Wang, Chen, and Zhu, 2005]. Such large shifts are of practical interest for sensing and beam steering applications, due to their high sensitivity and tunability.

Among advanced optical materials, photonic crystals offer a versatile platform for manipulating the GHS. Their periodic dielectric modulation gives rise to photonic band gaps and slow-light regions with strong phase dispersion. Near the band edges or in the vicinity of surface modes, the group velocity of the reflected wave can approach zero or even become negative, leading to both giant and negative shifts [He, Yi, and He, 2006; Soboleva, Moskalenko, and Fedyanin, 2012]. The geometry, lattice constant, and defect modes of the photonic crystal can be engineered to control both the amplitude and the sign of the shift, providing a powerful means of tailoring light propagation in integrated photonic devices.

In Chapter 3, we will investigate the GHS in a one-dimensional photonic crystal composed of anisotropic layers. As will be shown, the sign and magnitude of the shift depend sensitively on the anisotropy and constitutive parameters of the constituent media, leading to either positive or negative lateral displacements depending on the specific configuration [Provenzano and La Rocca, 2024].

1.8 Electromagnetic Surface Waves

Electromagnetic surface waves (ESWs) are solutions of Maxwell's equations that remain confined to the interface between two dissimilar media. Unlike bulk electromagnetic waves, which propagate freely in homogeneous materials, surface modes exhibit evanescent field components that decay exponentially away from

the interface, concentrating the electromagnetic energy in a narrow region near the boundary. Their fields are characterized by a complex wave vector, whose real part corresponds to propagation along the interface and whose imaginary part describes exponential decay perpendicular to it.

Since the pioneering work of Jonathan Zenneck in 1907 [Zenneck, 1907], ESWs have attracted the attention of numerous researchers due to their strong field localization and potential applications in sub-wavelength optics and sensing.

The existence of surface modes requires that at least one of the adjoining media supports an evanescent field in the direction normal to the interface. This typically occurs when one of the materials exhibits a negative or anisotropic dielectric response, or when dissipation and dispersion play a significant role. The prototypical and most studied example is the *Surface Plasmon Polariton* (SPP), a coupled electromagnetic–charge-density mode that propagates along the boundary between a dielectric and a metal with negative real permittivity at optical frequencies [Raether, 1988; Maier, 2007].

At a simple boundary between two homogeneous, isotropic, and lossless dielectric media, the conditions for field localization are not met, and no nontrivial surface eigenmodes exist. By contrast, when absorption, anisotropy, or material dispersion enter the picture, these limitations are relaxed and localized surface modes can appear. Depending on the material properties and geometry, several distinct classes of surface waves are possible.

- **Surface Plasmon Polaritons (SPPs):** TM-polarized modes that propagate along metal–dielectric interfaces, arising from the coupling between light and collective oscillations of free electrons. Their dispersion relation lies below the light line of the dielectric, resulting in a phase velocity smaller than that of light in the same medium. The degree of confinement and propagation length depend strongly on the dielectric functions of both media [Raether, 1988; Maier, 2007].

- **Dyakonov Surface Waves (DSWs):** hybrid-polarized, lossless modes existing at the interface between an isotropic dielectric and a uniaxial or biaxial anisotropic crystal. Unlike SPPs, they occur entirely in dielectric systems and can propagate only within a narrow angular range determined by the principal axes of anisotropy [D'yakonov, 1988; Takayama et al., 2009].

- **Zenneck Waves (ZWs):** TM-polarized modes that exist at the interface between a lossless dielectric and a lossy dielectric or semiconductor. Their fields are tilted with respect to the interface normal, and the mode attenuates along the propagation direction due to absorption in the lossy medium [Collin, 2004].

- **Tamm Waves (TWs)** and **Bloch Surface Waves (BSWs):** modes supported at the interface between a periodic dielectric multilayer (a one-dimensional photonic crystal) and a homogeneous dielectric. Depending on the polarization, they may exist in either TE or TM configurations. These modes originate

from photonic bandgap confinement and can exhibit low propagation losses compared to metal-based plasmons [Yeh, Yariv, and Hong, 1977; Kavokin, Shelykh, and Malpuech, 2005; Liscidini and Sipe, 2009].

- **Spoof Plasmons:** engineered surface modes supported by periodically structured conductors that mimic the dispersion and confinement of optical plasmons at microwave or terahertz frequencies. Their effective plasma frequency and confinement can be tuned by geometry, extending plasmonic behavior to spectral regions where natural plasmons do not exist [Pendry, Martín-Moreno, and García-Vidal, 2004].

From a theoretical standpoint, electromagnetic surface waves arise as solutions to the boundary-value problem for Maxwell's equations, where the tangential components of the electric and magnetic fields are continuous across the interface. For TM-polarized modes, this requirement yields the well-known dispersion relation

$$\frac{\epsilon_1}{\sqrt{k_{\parallel}^2 - \epsilon_1 \frac{\omega^2}{c^2}}} + \frac{\epsilon_2}{\sqrt{k_{\parallel}^2 - \epsilon_2 \frac{\omega^2}{c^2}}} = 0,$$

where $k_{\parallel}$ is the propagation constant along the interface, ω is the angular frequency, and ϵ_1, ϵ_2 are the permittivities of the two media. A surface mode can exist only when ϵ_1 and ϵ_2 have opposite real parts, ensuring exponential decay of the fields in both media. This condition is satisfied at metal–dielectric interfaces in the visible and near-infrared spectral regions, where metals exhibit negative real permittivity [Raether, 1988; Maier, 2007].

SPPs and their dielectric counterparts, such as Dyakonov and Bloch surface waves, have been experimentally demonstrated across a broad range of material platforms and frequencies. Their strong field confinement at interfaces enhances local electromagnetic density of states and enables control of optical modes at subwavelength scales [Zayats, Smolyaninov, and Maradudin, 2005; Liscidini and Sipe, 2009]. These properties have led to numerous implementations of surface-wave-based architectures for signal routing, field localization, and coupling in planar photonic structures.

The sharp dependence of the surface-wave dispersion on the refractive index of the surrounding medium is exploited in a variety of sensing configurations. In surface plasmon resonance (SPR) spectroscopy, the resonance wavelength or angle shifts with minute changes in analyte refractive index, allowing label-free chemical and biological detection with very high sensitivities down to 10^{-6} refractive index units [Homola, 2008; Anker et al., 2008]. Bloch surface waves in dielectric multilayers offer a low-loss alternative to metallic SPR sensors, combining high quality factors with simpler fabrication and improved environmental stability [Liscidini and Sipe, 2009].

Electromagnetic surface waves also support enhanced optical nonlinearities and near-field coupling effects, which are useful for Raman spectroscopy, fluorescence

enhancement, and nanoscale imaging. By tuning the dispersion and confinement through material selection or structural design, it is possible to engineer spectral response, propagation length, and mode overlap to suit specific applications in sensing, communications, and integrated photonics.

Two comprehensive overviews of ESWs can be found in [Polo and Lakhtakia, 2011; Polo, Mackay, and Lakhtakia, 2013].

In Chapters 2 and 3, we will analyze original configurations that enable the propagation of new types of ESWs under specific conditions.

Chapter 2

Symmetries of Constitutive Functions and Classification of Media

This chapter explores the foundational concepts of constitutive functions in macroscopic electrodynamics. It begins by examining the role of these functions, which depend on the specific properties of the material, yet share universal characteristics shaped by symmetries such as time-reversal, Lorentz reciprocity, and energy conservation. These symmetries, rooted in principles like causality and thermodynamic equilibrium, govern the structure of response functions across different materials. The chapter then transitions to the classification of materials based on these symmetries, proposing a systematic framework for understanding various media, from isotropic to complex anisotropic materials, and eventually bi-anisotropic materials. By presenting this classification, the chapter highlights how symmetries dictate the behavior of materials under electromagnetic influence and provides a comprehensive framework for studying the electromagnetic properties of different media. Finally, we study two original configurations to illustrate the effects of reciprocity in electromagnetic systems. While one configuration supports bidirectional surface wave propagation despite local energy imbalance, the other allows only unidirectional surface modes, yet both can achieve global energy conservation under specific conditions.

2.1 Introduction

Constitutive functions describe how materials respond to external electromagnetic fields and form the backbone of macroscopic electrodynamics. Their structure allows us to predict the evolution of electromagnetic phenomena in matter. Although these functions are specific to each medium, depending on its structural and interaction properties, they also exhibit universal features resulting from both fundamental principles, such as causality and thermodynamic equilibrium, and symmetries. This chapter focuses on the three principal symmetries that affect the form of response functions: time-reversal, Lorentz reciprocity, and energy conservation symmetry. Time-reversal symmetry describes the behavior of physical systems under temporal inversion, whereas Lorentz reciprocity ensures that the transmission of signals between two points in space remains invariant when their

positions are exchanged. Finally, energy conservation guarantees that the energy absorbed, reflected or transmitted by a material cannot exceed the energy supplied by the external electromagnetic field. The aim of this chapter is to analyze how these symmetries shape the structure of response functions. This aspect has been addressed in previous reviews, especially in [Asadchy et al., 2020] and [Caloz et al., 2018]. Here, we provide a less in-depth treatment, but adopt a more transparent approach. Furthermore, we describe a classification scheme for electromagnetic media, which is based on their adherence to or deviation from these symmetries. This classification provides a robust foundation for understanding the behavior of different classes of materials, from isotropic to bi-anisotropic ones.

Before diving into the main discussion, it is crucial to make two key clarifications in order to prevent potential misunderstandings.

- As throughout the entire thesis, the following discussion is based on the plane wave representation $\exp\{[+i(\mathbf{k}\cdot\mathbf{r}-\omega t)]\}$. It is important to clarify such an aspect because the sign in the exponent affects, among other factors, the sign of the imaginary part of the response functions. For example, in the current representation, lossy dielectrics have $\mathrm{Im}[\epsilon] > 0$, whereas the same materials would be characterized by $\mathrm{Im}[\epsilon] < 0$ in the (-) representation.

- There are multiple formalisms used to describe electromagnetic fields in matter. This stems from the fact that Maxwell's equations remain invariant under specific transformations of polarization and magnetization. Although infinitely many gauges are possible in theory, two formalisms stand out as the most practical and widely used: the standard formalism, also known as the *EBDH approach*, and the asymmetric formalism, also referred to as the *EBD approach* or the *Landau approach*, where the vector $\mathbf{H}$ loses its conventional significance since the relative permeability reduces to the identity. The equivalence of the two approaches is addressed in Appendix A, but we recommend reading this chapter first to align with the notation. The subsequent discussion, as well as the entire thesis, adopts the standard formalism widely used in western literature.

As is customary in any comprehensive treatment of electrodynamics, it is helpful to begin with Maxwell's equations. Their most general differential form is

$$\begin{cases} \nabla\cdot\mathbf{D} = \rho_\mathrm{e} + \rho_\mathrm{f}, \\ \nabla\cdot\mathbf{B} = 0, \\ \nabla\times\mathbf{E} = -\frac{\partial\mathbf{B}}{\partial t}, \\ \nabla\times\mathbf{H} = \mathbf{J}_\mathrm{e} + \mathbf{J}_\mathrm{f} + \frac{\partial\mathbf{D}}{\partial t}, \end{cases} \tag{2.1}$$

where ρ_e and $\mathbf{J}_\mathrm{e}$ are the external sources, whereas ρ_f and $\mathbf{J}_\mathrm{f}$ are the sources relative to free carriers. The constitutive relations, which relate the induced fields $\mathbf{D}$ and

$\mathbf{H}$ to the fundamental fields $\mathbf{E}$ and $\mathbf{B}$,[1] are determined by the specific properties of the material under examination. In conventional media, electric and magnetic-nature fields do not influence each other, hence constitutive relations are of the form $\mathbf{D} = f(\mathbf{E})$ and $\mathbf{H} = f(\mathbf{B})$. In contrast, in bi-(an)isotropic media, electric excitations can induce magnetic fields and vice versa. This results in the constitutive relations being expressed as $\mathbf{D}, \mathbf{H} = f(\mathbf{E}, \mathbf{B})$, with the simplest form being[2]

$$\begin{aligned} \mathbf{D} &= \boldsymbol{\epsilon} \cdot \mathbf{E} + \boldsymbol{\xi} \cdot \mathbf{B}, \\ \mathbf{H} &= \boldsymbol{\zeta} \cdot \mathbf{E} + \boldsymbol{\mu}^{-1} \cdot \mathbf{B}, \end{aligned} \tag{2.2}$$

where $\boldsymbol{\epsilon}$ and $\boldsymbol{\mu}$ are the dielectric and magnetic tensors, respectively, while $\boldsymbol{\xi}$ and $\boldsymbol{\zeta}$ are additional tensors that account for the so-called *magneto-electric coupling*. Thus, it can be said that every material in nature is characterized by at least two constitutive functions.[3] Often, their determination involves branches of Physics other than Electromagnetism: they can be modeled by using methods of Quantum Mechanics, such as the Fermi golden rule for atomic transitions, or Physical Kinetics, such as the well-known models of Drude and Lorentz.

Unfortunately, or perhaps fortunately, constitutive functions are not mere constants that depend only on the nature of the medium, but also on the characteristics of the electromagnetic fields that permeate them. In the case of electromagnetic waves propagating in linear media, the generic constitutive function element $\mathfrak{R}_{ij}$ can be written as[4]

$$\mathfrak{R}_{ij} = f\left(\omega, \mathbf{k}\right), \tag{2.3}$$

where ω and $\mathbf{k}$ are, respectively, the frequency and wave vector.[5] Moreover, such

[1] Despite the fact that constitutive relations between the four fields $\mathbf{E}$, $\mathbf{B}$, $\mathbf{D}$ and $\mathbf{H}$ are interchangeable—meaning that any pair can be expressed in terms of the others—$\mathbf{E}$ and $\mathbf{B}$ are considered the fundamental fields, as they represent the macroscopic average of the fields appearing in the microscopic Maxwell's equations. By contrast, the induced fields $\mathbf{D}$ and $\mathbf{H}$ have no microscopic counterparts.

[2] Equation (2.2) expresses the constitutive equations in the so-called *Boys-Post* form [Mackay and Lakhtakia, 2019]. The same equations can be rearranged to the alternative form $(\mathbf{D}, \mathbf{B}) = g(\mathbf{E}, \mathbf{H})$, known as *Tellegen representation*. The theory of electromagnetic waves propagating in bi-(an)isotropic media was first developed by J. A. Kong in the late 1960s [Cheng and Kong, 1968; Kong, 1970; Kong, 1972]. The reader may find more insights in [Polo, Mackay, and Lakhtakia, 2013], [Lindell et al., 1994] and [Semchenko, Tretyakov, and Serdyukov, 1996].

[3] In the literature, an additional constitutive function often appears even for simpler media: the conductivity σ, which relates $\mathbf{J}_f$ to the electric field. While, for stationary fields, it effectively acts as a third constitutive function, in the case of electromagnetic waves, as considered here, it can be absorbed into the dielectric function due to the form of Eq. (2.1). As suggested by the RHS of Ampère-Maxwell equation, the effective dielectric tensor becomes $\boldsymbol{\varepsilon} \equiv \boldsymbol{\epsilon} + \frac{i}{\omega}\boldsymbol{\sigma}$. However, the principal axes of $\boldsymbol{\epsilon}$ and $\boldsymbol{\sigma}$ do not generally coincide, except for highly symmetric materials. Thus, it is not trivial to find a coordinate system wherein $\boldsymbol{\varepsilon}$ has a diagonal structure.

[4] In the case of nonlinear media, the response functions may also depend on the amplitude of the applied field and on various combinations of the frequencies ω_i of the interacting waves. This gives rise to phenomena such as harmonic generation or wave mixing [Boyd, 2008]. In this thesis, we will not deal with nonlinear optics effects.

[5] In Eq. (2.3), the dependencies on ω and $\mathbf{k}$ are referred to as *temporal* and *spatial dispersions*, respectively. Such effects are due to temporal and spatial non-localities, as it will be shown in

functions may also vary in space and time and have complex values. Their real and imaginary parts are related to each other by Kramers-Kronig relations, arising from the principle of causality [Landau and Lifshitz, 1984]. In the case of $\boldsymbol{\epsilon}$ and $\boldsymbol{\mu}$, imaginary parts are related to the presence of absorption or gain.

As for isotropic media, which are characterized by dielectric and magnetic scalar functions, a widely used classification is based on the values of the real parts of ϵ and μ. Depending on their sign, six different types of media can be distinguished, as illustrated in Fig. 2.1. Unusual effects can arise even in this simple case: for instance, in Negative-Index Materials (NIMs) the Poynting vector is antiparallel to the wave vector[6] [Veselago, 1968]. By analyzing more complex media, new fascinating phenomena emerge, such as birefringence and Faraday rotation. In this case, however, the dimension of the parameter space is so large that a classification based on the signs of the response tensor elements becomes impractical. The literature offers numerous classifications of anisotropic media, most of which are either unclear or lack pedagogical and explanatory value. This chapter will ultimately present what the author regards as the only classification truly worthy of note. It is based on the three fundamental symmetries of electromagnetism: time-reversal, Lorentz reciprocity, and energy conservation, which will be discussed in Section 2.3.

2.2 Linear Response Theory

Restricting the discussion to linear media,[7] the induced fields are superpositions of effects associated with external perturbations, expressed through convolution integrals. Hence, for a generic (bi-)anisotropic linear medium, the induced field can be written as

$$D_i(\mathbf{r},t) = \sum_j \int_{-\infty}^{+\infty} \mathrm{d}t' \int \mathrm{d}\mathbf{r}' \left[\epsilon_{ij}\left(\mathbf{r},\mathbf{r}',t,t'\right) E_j\left(\mathbf{r}',t'\right) + \xi_{ij}\left(\mathbf{r},\mathbf{r}',t,t'\right) B_j\left(\mathbf{r}',t'\right) \right], \tag{2.4}$$

where the kernels $\epsilon_{ij}\left(\mathbf{r},\mathbf{r}',t,t'\right)$ and $\xi_{ij}\left(\mathbf{r},\mathbf{r}',t,t'\right)$ carry the information about the response of the medium to external non-homogeneous, non-stationary electric and magnetic fields. An analogous relation can be written for $H_i(\mathbf{r},t)$, but this

Section 2.2: the medium's response at point $\mathbf{r}$ and time t may depend on the value of the external perturbation at point $\mathbf{r}' \neq \mathbf{r}$ and at a previous time $t' < t$. The theory of response functions affected by spatial dispersion was widely developed in the 20$^{\text{th}}$ century by Soviet physicists, such as Landau, Agranovic [Agranovich and Ginzburg, 1984] and Fedorov [Semchenko, Tretyakov, and Serdyukov, 1996]. A practical case of spatial dispersion will be discussed in Chapter 4, in the setting of planar configurations under an external magnetic field realizing the fractional quantum Hall effect.

[6] The Poynting vector $\mathbf{S} \equiv \mathbf{E} \times \mathbf{H}$ defines the direction of energy flow within the medium and it is identified as the direction of the ray in geometric optics. As illustrated in Fig. 2.1, the energy flow in NIMs is directed opposite to the wave vector, leading to a negative group velocity. Mathematically, this phenomenon is equivalent to describing such media using a negative refractive index. While the ray is always parallel or antiparallel to the wave vector $\mathbf{k}$ in isotropic media, this is no longer true in a generic anisotropic material, where $\mathbf{k}$ is parallel to the forms $\mathbf{E} \times \mathbf{B}$ and $\mathbf{D} \times \mathbf{H}$ [Wang, 2015].

[7] This assumption is generally valid provided that the field intensities remain sufficiently small.

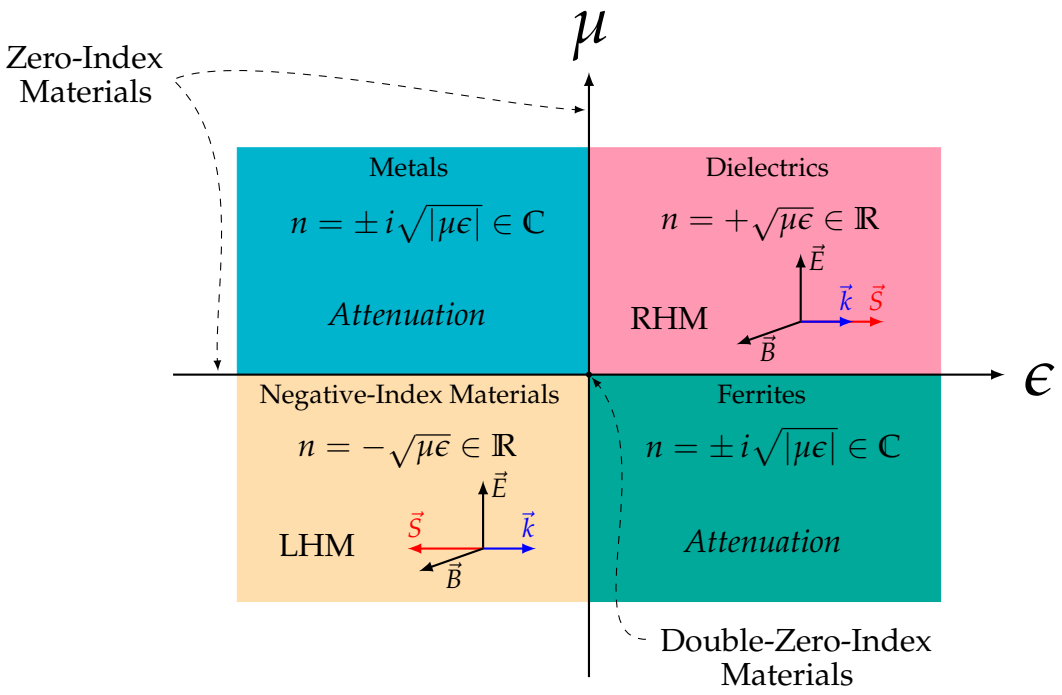

FIGURE 2.1: Classification of isotropic materials, based on the real parts of their response functions.

section is restricted to the electric case for the sake of clarity. All kernels must obey the causality principle [Melrose and McPhedran, 1991], hence they are null if $t' > t$ because the medium cannot respond before the external fields have acted. This implies that the contribution from the integration interval $[t, +\infty]$ vanishes. As for spatial integration, the finite nature of signal propagation speed imposes integration on the bounded region $|\mathbf{r} - \mathbf{r}'| \leq c\,|t - t'|$. However, spatial integration can be performed on the entire sample because the response functions quickly drop to zero as $|\mathbf{r} - \mathbf{r}'|$ becomes large.

The physical meaning of the convolution integrals in Eq. (2.4) is that the medium response at the position $\mathbf{r}$ and the instant t depends on the fields values in its surroundings and at previous instants of time as well. The latter is due to the rearrangement of charges and currents of the medium, which is caused by field variations. This phenomenon does not occur instantaneously but lasts a finite time τ_r, called *relaxation time*. In Eq. (2.4), the time integration interval is on the order of the relaxation time of the system, because the kernels rapidly decrease to zero as $t - t' \gg \tau_r$. Furthermore, if the properties of the medium do not change with time, i.e. the medium is stationary, then all times t are equivalent and the kernels depend only on the difference $t - t'$, which means

$$\mathfrak{R}_{ij}\left(\boldsymbol{r}, \boldsymbol{r}', t, t'\right) = \mathfrak{R}_{ij}\left(\boldsymbol{r}, \boldsymbol{r}', t - t'\right).$$

On the other hand, the dependence on other spatial positions is due to insertions in the medium, which can be natural or artificially implanted to obtain desired

electromagnetic properties. The larger the field variations in space, the stronger the non-local effects. In addition, the kernels decrease considerably at distances $\left|\mathbf{r}-\mathbf{r}'\right|$ that are large compared to the intrinsic characteristic length of the material.[8] In a homogeneous medium, the response functions depend only on the difference $\mathbf{r}-\mathbf{r}'$ due to space-translation invariance, thus

$$\mathfrak{R}_{ij}\left(\boldsymbol{r},\boldsymbol{r}',t,t'\right)=\mathfrak{R}_{ij}\left(\boldsymbol{r}-\boldsymbol{r}',t,t'\right).$$

Therefore, in stationary and homogeneous linear media,[9] Eq. (2.4) becomes

$$D_i(\mathbf{r},t)=\sum_j\int_{-\infty}^{+\infty}\mathrm{d}t'\int\mathrm{d}\mathbf{r}'\left[\epsilon_{ij}\left(\mathbf{r}-\mathbf{r}',t-t'\right)E_j\left(\mathbf{r}',t'\right)+\xi_{ij}\left(\mathbf{r}-\mathbf{r}',t-t'\right)B_j\left(\mathbf{r}',t'\right)\right], \tag{2.5}$$

The spatial and temporal invariance of the system suggests the use of the plane wave expansion via Fourier transforms:

$$\mathbf{F}(\mathbf{r},t)=\int\mathrm{d}\omega\int\mathrm{d}\mathbf{k}\;\mathcal{F}(\mathbf{k},\omega)\;e^{i(\mathbf{k}\cdot\mathbf{r}-\omega t)}, \tag{2.6}$$

where $\mathbf{F}$ represents the generic vector field. Physically speaking, Fourier's expansion gives all possible plane waves allowed to propagate in the medium and Fourier's coefficients $\mathcal{F}(\mathbf{k},\omega)$ specify the field amplitudes of these plane waves. Introducing the Fourier expansion also for response tensors yields

$$\mathfrak{R}_{ij}(\mathbf{r}-\mathbf{r}',t-t')=\int\mathrm{d}\omega\int\mathrm{d}\mathbf{k}\;\mathfrak{R}_{ij}(\mathbf{k},\omega)\;e^{i[\mathbf{k}\cdot(\mathbf{r}-\mathbf{r}')-\omega(t-t')]}.$$

Using the convolution properties of Fourier's transforms, Eq. (2.5) becomes

$$\mathcal{D}_i(\mathbf{k},\omega)=\sum_j\epsilon_{ij}(\mathbf{k},\omega)\,\mathcal{E}_j(\mathbf{k},\omega)+\sum_j\xi_{ij}(\mathbf{k},\omega)\,\mathcal{B}_j(\mathbf{k},\omega)\quad\Longrightarrow\quad\mathcal{D}=\boldsymbol{\epsilon}\cdot\mathcal{E}+\boldsymbol{\xi}\cdot\mathcal{B}, \tag{2.7}$$

which is exactly the constitutive relation in Boys-Post representation, as given in Eq. (2.2). In the rest of the chapter, the fundamental symmetry properties of the response functions will be demonstrated for anisotropic media in general, while only the final results will be provided for bi-anisotropic media.

[8] Examples of characteristic lengths are the lattice constant for crystals, the mean free path of electrons in metals and the Debye length for plasmas.

[9] In the particular case where kernels can be written as

$$\mathfrak{R}_{ij}\left(\mathbf{r}-\mathbf{r}',t-t'\right)=\mathfrak{R}_{ij}\,\delta\left(\mathbf{r}-\mathbf{r}'\right)\delta\left(t-t'\right),$$

the response fields in $(\mathbf{r},t)$ only depend on the external fields applied in the same point and at the same time. Hence, such media are not affected by spatial and temporal non-localities.

2.3 Electromagnetic Symmetries and Constitutive Functions

As mentioned in the previous section, the structure of response dyadics in specific classes of media can be derived on the basis of general physics principles. Generally, each response function is complex and its real and imaginary parts obey Kramers-Kronig relations, which are direct consequences of the causality principle. In the following chapters we consider both dispersive and non-dispersive response functions for our models. The latter are sufficient to explain part of the physical phenomena that take place in matter, even though they may lead to apparent paradoxes. As an example, the average electromagnetic energy density for time-harmonic fields in a transparent anisotropic medium is given by Brillouin's formula [Jackson, 1999]:

$$\langle w_{\mathrm{em}} \rangle = \frac{1}{4}\,\mathbf{E}^* \cdot \frac{\partial(\omega \boldsymbol{\epsilon}(\omega))}{\partial \omega} \cdot \mathbf{E} + \frac{1}{4}\,\mathbf{H}^* \cdot \frac{\partial(\omega \boldsymbol{\mu}(\omega))}{\partial \omega} \cdot \mathbf{H}. \tag{2.8}$$

If we consider a simple non-dispersive isotropic left-handed medium [Veselago, 1968] where $\epsilon, \mu < 0$, Eq. (2.8) would return a negative value for the average electromagnetic energy, which has no physical meaning. As mentioned above, the problem lies in the lack of dependence on the frequency, which lets $\frac{\partial(\omega\epsilon)}{\partial\omega} = \epsilon < 0$. The apparent paradox is fixed by introducing temporal dispersion: in the transparent region, Kramers-Kronig relations imply the inequality $\frac{\partial(\omega\epsilon(\omega))}{\partial\omega} > 0$ which holds for *any* dispersive dielectric function [Landau and Lifshitz, 1984; Fabrizio and Morro, 2003]. Thus, the positiveness of electromagnetic energy is ensured.

In the rest of the thesis, we will primarily use the results of the temporal-dispersion theory, but they can be generalized to the case where spatial dispersion is also present. For example, the expression for the electromagnetic energy density remains the same as Eq. (2.8), while the Poynting vector becomes [Toptygin and Levina, 2016; Costa, Silveirinha, and Alù, 2011]

$$\mathbf{S}_i = \frac{1}{2\mu_0}\,\mathrm{Re}\left\{\left(\mathbf{E} \times \mathbf{B}^*\right)_i\right\} - \frac{1}{4}\omega\,\mathbf{E}^* \cdot \frac{\partial \boldsymbol{\varepsilon}_{\mathrm{eff}}}{\partial k_i}(\omega, \mathbf{k}) \cdot \mathbf{E},$$

where the tensor $\boldsymbol{\varepsilon}_{\mathrm{eff}}$ contains information about both the electric and magnetic response [Landau and Lifshitz, 1984; Toptygin, 2015], as briefly described in Appendix A. In this case, the interface conditions for electromagnetic fields at the boundaries between different materials may be different from the usual ones: their nature can be significantly altered by the derivatives that appear within the constitutive relations. Interface conditions must account for the spatial derivatives of the fields reflecting the non-local response of the medium, leading to more complex boundary conditions [Semchenko, Tretyakov, and Serdyukov, 1996; Serdyukov et al., 2001b; Agranovich and Ginzburg, 1984].

In the following paragraphs, we will discuss how energy conservation, reciprocity,

and time-reversal symmetry modify the structure of electromagnetic response functions affected by temporal dispersion.

2.3.1 Energy conservation

It is well known that, in the absence of free carriers, Maxwell's equations lead to the following energy balance equation:

$$-\nabla \cdot (\mathbf{E} \times \mathbf{H}) = \mathbf{E} \cdot \frac{\partial \mathbf{D}}{\partial t} + \mathbf{H} \cdot \frac{\partial \mathbf{B}}{\partial t}, \tag{2.9}$$

which can be written as

$$-\nabla \cdot \mathbf{S}(\mathbf{r}, t) = \frac{\partial}{\partial t} \left[w_{\text{em}}(\mathbf{r}, t) \right] + q(\mathbf{r}, t), \tag{2.10}$$

where $\mathbf{S}$ stands for the Poynting vector, w_{em} represents the electromagnetic energy density and q is the dissipated energy per unit volume and time. Let us consider an electromagnetic field that is generated at a certain time and eventually decays back to zero. By integrating Eq. (2.10) over time, the electromagnetic energy density term vanishes, as it is zero at both $t = \pm\infty$. Thus, we obtain

$$\Delta Q(\mathbf{r}) \equiv \int_{-\infty}^{+\infty} q(\mathbf{r}, t) \mathrm{d}t = -\int_{-\infty}^{+\infty} \nabla \cdot \mathbf{S}(\mathbf{r}, t)\, \mathrm{d}t = \int_{-\infty}^{+\infty} \left(\mathbf{E} \cdot \frac{\partial \mathbf{D}}{\partial t} + \mathbf{H} \cdot \frac{\partial \mathbf{B}}{\partial t} \right) \mathrm{d}t. \tag{2.11}$$

The sign of ΔQ determines if the medium is lossless ($\Delta Q = 0$), lossy ($\Delta Q > 0$) or active ($\Delta Q < 0$). Using the frequency representation for electromagnetic fields, we write the fields as functions of their temporal Fourier transform

$$\mathbf{E}(\mathbf{r}, t) = \frac{1}{2\pi} \int_{-\infty}^{+\infty} \mathrm{d}\omega\, \mathcal{E}(\omega)\, e^{-i\omega t}, \qquad \mathbf{D}(\mathbf{r}, t) = \frac{1}{2\pi} \int_{-\infty}^{+\infty} \mathrm{d}\omega'\, \mathcal{D}\left(\omega'\right)\, e^{-i\omega' t},$$

and thus find

$$\mathbf{E} \cdot \frac{\partial \mathbf{D}}{\partial t} = -\frac{i}{(2\pi)^2} \int_{-\infty}^{+\infty} \mathrm{d}\omega \int_{-\infty}^{+\infty} \mathrm{d}\omega'\, \omega'\, \mathcal{E}(\omega) \cdot \boldsymbol{\epsilon}\left(\omega'\right) \cdot \mathcal{E}\left(\omega'\right) e^{-i\left(\omega+\omega'\right)t}.$$

Repeating the same derivation for the magnetic fields, the dissipated energy density becomes

$$\begin{aligned} \Delta Q = -\frac{i}{(2\pi)^2} \int_{-\infty}^{+\infty} \mathrm{d}\omega \int_{-\infty}^{+\infty} \mathrm{d}\omega'\, \omega' \Big\{ & \mathcal{E}(\omega) \cdot \boldsymbol{\epsilon}\left(\omega'\right) \cdot \mathcal{E}\left(\omega'\right) + \\ & + \mathcal{H}(\omega) \cdot \boldsymbol{\mu}\left(\omega'\right) \cdot \mathcal{H}\left(\omega'\right) \Big\} \int_{-\infty}^{+\infty} \mathrm{d}t\, e^{-i\left(\omega+\omega'\right)t}. \end{aligned} \tag{2.12}$$

After performing the time integral in Eq. (2.12), we integrate with respect to ω and obtain

$$\Delta Q = -\frac{i}{2\pi}\int_{-\infty}^{+\infty} \mathrm{d}\omega'\, \omega' \left\{ \mathcal{E}(-\omega')\cdot\boldsymbol{\epsilon}\left(\omega'\right)\cdot\mathcal{E}\left(\omega'\right) + \mathcal{H}\left(-\omega'\right)\cdot\boldsymbol{\mu}\left(\omega'\right)\cdot\mathcal{H}\left(\omega'\right) \right\}. \tag{2.13}$$

Instead, integrating with respect to ω' leads to

$$\Delta Q = +\frac{i}{2\pi}\int_{-\infty}^{+\infty} \mathrm{d}\omega\, \omega \left\{ \mathcal{E}(\omega)\cdot\boldsymbol{\epsilon}\left(-\omega\right)\cdot\mathcal{E}\left(-\omega\right) + \mathcal{H}\left(\omega\right)\cdot\boldsymbol{\mu}\left(-\omega\right)\cdot\mathcal{H}\left(-\omega\right) \right\}. \tag{2.14}$$

All fields in the $(\mathbf{r}, t)$-representation are real quantities. Hence, all the entries of the kernels in Eq. (2.5) and in its magnetic counterpart are so. This implies

$$\mathcal{E}(-\omega) = \mathcal{E}^*(\omega), \qquad \mathcal{H}(-\omega) = \mathcal{H}^*(\omega), \qquad \mathfrak{R}_{ij}\left(\mathbf{r}, -\omega\right) = \mathfrak{R}_{ij}^*\left(\mathbf{r}, \omega\right).$$

By adding Eqs. (2.13) and (2.14) and applying the relations just derived, we obtain

$$2\Delta Q = -\frac{i}{2\pi}\int_{-\infty}^{+\infty} \mathrm{d}\omega\, \omega \left\{ \mathcal{E}^*\cdot\boldsymbol{\epsilon}\cdot\mathcal{E} - \mathcal{E}\cdot\boldsymbol{\epsilon}^*\cdot\mathcal{E}^* + \mathcal{H}^*\cdot\boldsymbol{\mu}\cdot\mathcal{H} - \mathcal{H}\cdot\boldsymbol{\mu}^*\cdot\mathcal{H}^* \right\}, \tag{2.15}$$

where we dropped the frequency dependence because now all quantities depend on ω. Finally, the identity for vector-matrix multiplications $\mathbf{v}\cdot\mathbf{M}^*\cdot\mathbf{v}^* = \mathbf{v}^*\cdot\mathbf{M}^\dagger\cdot\mathbf{v}$ yields

$$\Delta Q = -\frac{i}{4\pi}\int_{-\infty}^{+\infty} \mathrm{d}\omega\, \omega \left\{ \mathcal{E}^*\cdot\left[\boldsymbol{\epsilon} - \boldsymbol{\epsilon}^\dagger\right]\cdot\mathcal{E} + \mathcal{H}^*\cdot\left[\boldsymbol{\mu} - \boldsymbol{\mu}^\dagger\right]\cdot\mathcal{H} \right\},$$

where the symbol † stands for the conjugate transpose. Since this last relation must hold for all values of $\mathcal{E}$ and $\mathcal{H}$, ΔQ is zero if and only if $\boldsymbol{\epsilon} = \boldsymbol{\epsilon}^\dagger$ and $\boldsymbol{\mu} = \boldsymbol{\mu}^\dagger$. In such cases, the average electromagnetic energy density for temporally dispersive materials is given by Eq. (2.8).

2.3.2 Lorentz reciprocity

In electromagnetism, a system is said to be *reciprocal* if the response at point A due to a source located at point B is identical to the response at B due to an identical source located in A. This symmetry under the exchange of sources and fields plays a fundamental role in wave propagation and electromagnetic systems. However, certain systems exhibit non-reciprocity, meaning they allow preferential signal transmission in one direction. A classic example is the diode, which allows current flow primarily in one direction while blocking it in the reverse direction. A further notable class of non-reciprocal systems is *topological insulators*, where edge states have a preferential direction of propagation [Hasan and Kane, 2010; Kou et al.,

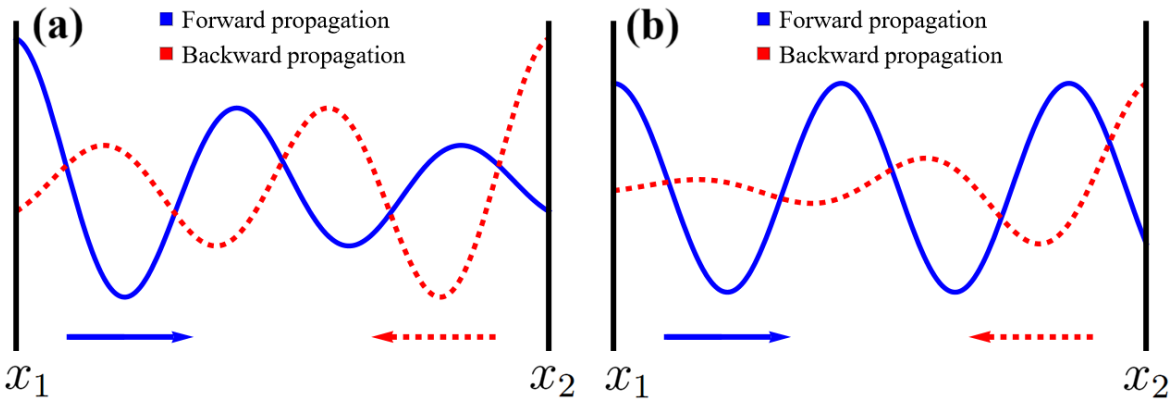

FIGURE 2.2: Comparison between the electromagnetic fields of forward and backward modes propagating (a) in a reciprocal medium and (b) in a non-reciprocal medium. Given the same initial conditions, modes in a reciprocal medium end up with the same amplitude. In contrast, this does not generally hold in non-reciprocal media.

2017]. The core difference between reciprocal and non-reciprocal propagation is schematically illustrated in Fig. 2.2.

To understand whether a system is reciprocal or not, let us consider a homogeneous medium with two sources $\mathbf{s}_a$ and $\mathbf{s}_b$ and the fields they generate in space, $\mathbf{F}_a$ and $\mathbf{F}_b$, respectively. The reaction of the field $\mathbf{F}_a$ on the source $\mathbf{s}_b$ is defined as

$$< \mathbf{F}_a, \mathbf{s}_b > \equiv \int_V \mathbf{J}_b \cdot \mathbf{E}_a \, \mathrm{d}V, \tag{2.16}$$

where V is a generic volume in space. If the reaction is symmetrical under the swap $a \rightleftharpoons b$, the system is said to be *Lorentz-reciprocal*. With the help of the divergence theorem and Maxwell's equations in the frequency domain, it can be shown that [Serdyukov et al., 2001b]

$$\begin{aligned} < F_a, \mathbf{s}_b > - < F_b, \mathbf{s}_a > &= \int_V \left(\mathbf{J}_b \cdot \mathbf{E}_a - \mathbf{J}_a \cdot \mathbf{E}_b \right) \mathrm{d}V = \\ &= \int_S \left(\mathbf{E}_a \times \mathbf{H}_b - \mathbf{E}_b \times \mathbf{H}_a \right) \cdot \mathrm{d}\mathbf{S} + \\ &+ i\omega \int_V \left(\mathbf{D}_a \cdot \mathbf{E}_b - \mathbf{D}_b \cdot \mathbf{E}_a + \mathbf{B}_b \cdot \mathbf{H}_a - \mathbf{B}_a \cdot \mathbf{H}_b \right) \mathrm{d}V, \end{aligned} \tag{2.17}$$

where S is the surface surrounding the volume V and $\mathrm{d}\mathbf{S}$ is the infinitesimal surface vector, which points outwards. Hence, exploiting the first equality, we deduce that the system enclosed in V is reciprocal if all sources lie outside.

In linear anisotropic media, the second term in Eq. (2.17) becomes

$$i\omega \int_V \left[\mathbf{E}_b \cdot \left(\boldsymbol{\epsilon} - \boldsymbol{\epsilon}^T \right) \cdot \mathbf{E}_a + \mathbf{H}_a \cdot \left(\boldsymbol{\mu} - \boldsymbol{\mu}^T \right) \cdot \mathbf{H}_b \right] \mathrm{d}V, \tag{2.18}$$

where $\boldsymbol{\epsilon}^T$ and $\boldsymbol{\mu}^T$ are the transpose constitutive tensors. The above relations must hold for every couple of electric and magnetic fields, hence the system enclosed in V is reciprocal if both $\boldsymbol{\epsilon} = \boldsymbol{\epsilon}^T, \boldsymbol{\mu} = \boldsymbol{\mu}^T$ and the surface integral is zero. The latter condition can be achieved in three scenarios.

1. All media within the volume V are characterized by symmetric constitutive tensors and all sources lie outside V. For example, any portion of an empty space is reciprocal.

2. Some sources lie inside the (bounded) volume V and the fields on the surface S obey the relation[10]
$$\mathbf{E}_{\parallel} = \boldsymbol{Z} \cdot (\hat{\mathbf{n}} \times \mathbf{H}), \tag{2.19}$$
where $\mathbf{E}_{\parallel}$ is the electric field component parallel to the boundary, $\boldsymbol{Z}$ is the surface impedance dyadic of the boundary [Lindell, 1992], which is symmetric, and $\hat{\mathbf{n}}$ is the normal to the surface. In such case, the surface integral becomes
$$\int_S (\mathbf{E}_a \times \mathbf{H}_b - \mathbf{E}_b \times \mathbf{H}_a) \cdot \hat{\mathbf{n}} \mathrm{d}S = \int_S \mathbf{H}_b \cdot \left(\boldsymbol{Z} - \boldsymbol{Z}^T\right) \cdot \mathbf{H}_a \mathrm{d}S,$$
which is null because we assumed that the impedance is symmetric.

3. All sources lie inside the (unbounded) volume V. We can enclose the system in an infinite-radius sphere, which extends in a homogeneous isotropic medium, i.e. vacuum. In such region of space, far away from the sources, the fields obey the relation $\mathbf{H} = \sqrt{\epsilon_0/\mu_0}\, \hat{\mathbf{r}} \times \mathbf{E}$ for spherical waves, where $\hat{\mathbf{r}}$ is the radial unit vector. This relation has the very same mathematical form of Eq. (2.19), hence the surface integral on the sphere is null.[11]

To sum up, the surface integral is very likely to be null in ordinary systems. Hence, the system enclosed in V is reciprocal if all media that comprise it can be described by symmetric constitutive tensors.

2.3.3 Time-reversal symmetry

In the framework of Electrodynamics, a system is said to be time-reversal symmetric if both Maxwell's equations and constitutive relations are satisfied when fields and sources are time-reversed [Caloz et al., 2018]. This happens only when the constitutive tensors fulfill particular conditions.

[10] For instance, this relation characterizes the fields on the boundaries of perfect conductors. In the familiar isotropic case, low values of Z correspond to good electric conductors, whereas high values correspond to good magnetic conductors.

[11] As suggested in [Asadchy et al., 2020], a further proof of such result is based on the so-called *limiting absorption principle* [Schulenberger and Wilcox, 1971]. Assuming a small imaginary part for the dielectric constant of the surrounding space, all fields will exponentially decay and thus the surface integral will vanish as the boundary goes to infinity. By taking the limit $\mathrm{Im}\,\epsilon \to 0$, the surface integral remains null [Nosich, 1994]. Such result also holds in the case of radiative fields.

In the time-domain representation, the action of the time-reversal operator on any real function is

$$\mathcal{T}\{f(t)\} = \pm f(-t),$$

where the $\pm$ sign depends on the parity of the physical quantity $f(t)$, which can be either a scalar or a vector. An intuitive explanation of the parity of physical quantities under the time-reversal transformation is now provided. As the quantity $f(t)$ evolves, we freeze time and rewind it backwards by an infinitesimal amount $\mathrm{d}t$. If $f(t-\mathrm{d}t) = f(t)$, then $f(t)$ is symmetric. If $f(t-\mathrm{d}t) = -f(t)$, then $f(t)$ is antisymmetric. For instance, the velocity of a body changes direction when time is rewound backwards. Hence, it is odd under time-reversal. By definition, time is odd under time-reversal. The position vector $\mathbf{r}$ and its even time-derivatives are time-reversal symmetric functions, whereas its odd time-derivatives are antisymmetric. Keeping this in mind, let us consider Maxwell's equations in the time domain:

$$\begin{cases} \nabla \cdot \mathbf{D} = \rho_{\mathrm{e}} + \rho_{\mathrm{f}}, \\ \nabla \cdot \mathbf{B} = 0, \\ \nabla \times \mathbf{E} = -\frac{\partial \mathbf{B}}{\partial t}, \\ \nabla \times \mathbf{H} = \mathbf{J}_{\mathrm{e}} + \mathbf{J}_{\mathrm{f}} + \frac{\partial \mathbf{D}}{\partial t}. \end{cases} \tag{2.20}$$

Just by looking at the equations, it is easy to understand that ρ, $\mathbf{E}$ and $\mathbf{D}$ have the same parity, which must differ from $\mathbf{J}$, $\mathbf{B}$ and $\mathbf{H}$. This means that there are only two ways to apply self-consistent time-reversal transformations that preserve the form of Eq. (2.20). However, since scalar quantities such as charge and mass are likely to be constant under time-reversal transformation, the same should be true for ρ. Hence, the only transformations which make sense are

$$\mathcal{T}\{\rho(t), \mathbf{E}(t), \mathbf{D}(t)\} = +\rho(-t), \mathbf{E}(-t), \mathbf{D}(-t),$$

$$\mathcal{T}\{\mathbf{J}(t), \mathbf{B}(t), \mathbf{H}(t)\} = -\mathbf{J}(-t), \mathbf{B}(-t), \mathbf{H}(-t).$$

Thus, in the time-domain representation, electric-nature fields are time-reversal symmetric, whereas magnetic ones are odd. As for the frequency domain representation, time-reversing the Fourier transform $\mathcal{F}(\omega)$ results in conjugating the function itself:

$$\mathcal{T}\{\mathcal{F}(\omega)\} = \mathcal{T}\left\{\int_{-\infty}^{+\infty} f(t)\, e^{i\omega t}\mathrm{d}t\right\} = \int_{-\infty}^{+\infty} \pm f(-t)\, e^{i\omega t}\, \mathrm{d}t = \tag{2.21}$$

$$= \int_{+\infty}^{-\infty} \pm f(t')\, e^{-i\omega t'}(-\mathrm{d}t') = \pm\, \mathcal{F}(-\omega) = \pm\, \mathcal{F}^*(\omega). \tag{2.22}$$

Therefore, for electromagnetic quantities,

$$\mathcal{T}\{\rho(\omega), \mathcal{E}(\omega), \mathcal{D}(\omega)\} = +\rho^*(\omega), +\mathcal{E}^*(\omega), +\mathcal{D}^*(\omega),$$

$$\mathcal{T}\{\mathcal{J}(\omega), \mathcal{B}(\omega), \mathcal{H}(\omega)\} = -\mathcal{J}^*(\omega), -\mathcal{B}^*(\omega), -\mathcal{H}^*(\omega).$$

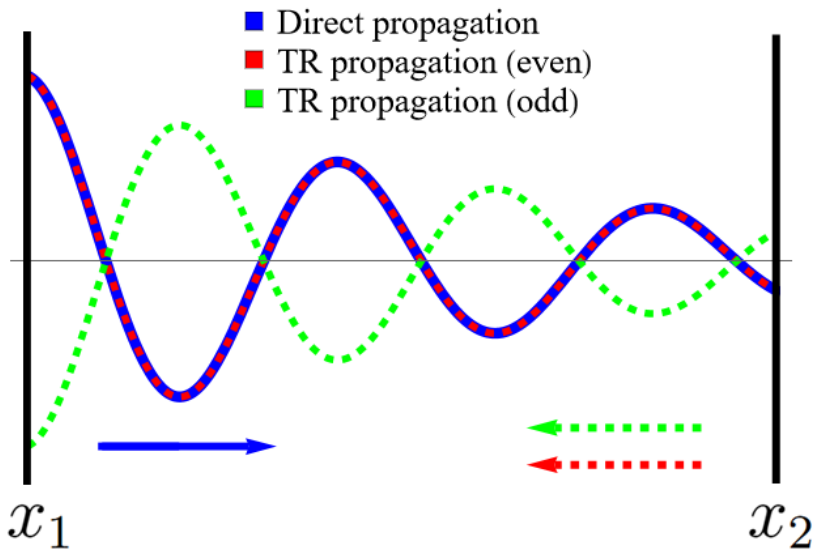

FIGURE 2.3: Comparison of the electromagnetic fields for forward and backward modes propagating in a time-reversal symmetric medium. Upon time-reversal, quantities with odd symmetry change sign.

Let us apply the time-reversal operator to the constitutive relations:

$$\mathcal{T}\{\mathcal{D}(\omega)\} = \epsilon_0 \mathcal{T}\{\boldsymbol{\epsilon}(\omega)\} \cdot \mathcal{T}\{\mathcal{E}(\omega)\} \quad \Longrightarrow \quad \mathcal{D}^*(\omega) = \epsilon_0 \mathcal{T}\{\boldsymbol{\epsilon}(\omega)\} \cdot \mathcal{E}^*(\omega).$$

Comparing the last equation to the complex conjugate of the same constitutive relation, one finds $\mathcal{T}\{\boldsymbol{\epsilon}(\omega)\} = \boldsymbol{\epsilon}^*(\omega)$. Since the same holds for the permeability tensor, the system is time-reversal symmetric if and only if $\boldsymbol{\epsilon}(\omega) = \boldsymbol{\epsilon}^*(\omega)$ and $\boldsymbol{\mu}(\omega) = \boldsymbol{\mu}^*(\omega)$. Thus, time-reversal symmetry is reached if all the entries of such matrices are real.

It is important to clarify that the notion of time-reversal symmetry discussed in this thesis is not directly related to the thermodynamic implications of the Onsager-Casimir relations. Since they were historically associated with time-reversal symmetry, a distinct term has been introduced to avoid confusion. The symmetry connected to the Onsager-Casimir relations is referred to as Restricted Time-Reversal Symmetry (RTRS), and it differs fundamentally from the actual TRS [Altman and Suchy, 2011]. The main distinction lies in the extent to which time-reversal is applied: in true TRS, time is reversed globally—affecting not only Maxwell's equations but also the evolution of all quantities and processes coupled to the system, such as external biases and collisional losses of matter. In contrast, RTRS reverses time only within the field equations. As a consequence, losses become gain under TRS, while under RTRS they remain losses [Asadchy et al., 2020]. Therefore, throughout this thesis, whenever TRS is mentioned, it refers exclusively to the true TRS, and not to RTRS.

2.4 General Classification of Media

Restricting to anisotropic-dielectric media, the three symmetry conditions found in the previous sections are

$$\begin{aligned} \epsilon_{ij} &= \epsilon_{ji}^* && \text{Energy Conservation (EC),} \\ \epsilon_{ij} &= \epsilon_{ji} && \text{Lorentz Reciprocity (LR),} \\ \epsilon_{ij} &= \epsilon_{ij}^* && \text{Time-Reversal Symmetry (TRS).} \end{aligned}$$

It is straightforward to verify that, for any matrix, these conditions are interdependent: if any two are satisfied, the third must also hold. For example, any medium that is both lossless and Lorentz-reciprocal supports the propagation of fields that obey TRS. Conversely, if one of these conditions is violated, at least one more must also fail. A notable example is gyrotropic media, which are non-reciprocal yet lossless. Their dielectric tensor is hermitian but contains complex off-diagonal elements, preventing them from allowing TRS and LR.

Therefore, based on the features described above, all possible media—real or hypothetical—can be classified according to the scheme shown in Fig. 2.4, as briefly outlined in [Buddhiraju et al., 2020]. Based on the three fundamental symmetries, only five types of media exist: those that exhibit only one symmetry (red, blue and green subsets), those that possess all three (central dark intersection) and those that lack any symmetry (surrounding white region). Notably, mathematics does not allow for the existence of media that exhibit exactly two symmetries. Let us briefly discuss the structure of the dielectric tensor in all subsets. In what follows, all Greek letters except ϵ, μ, ξ and ζ represent real parameters.

The most general form of the dielectric tensor for a medium where electromagnetic energy is conserved is

$$\boldsymbol{\epsilon}_{\mathrm{EC}} = \begin{pmatrix} \alpha & \eta + i\kappa & \upsilon + i\nu \\ \eta - i\kappa & \beta & \rho + i\sigma \\ \upsilon - i\nu & \rho - i\sigma & \gamma \end{pmatrix} \tag{2.23}$$

The finite-dimensional spectral theorem states that any hermitian matrix can be diagonalized - by rotating the coordinate system - and the resulting diagonal matrix has only real elements. Thus, in any homogeneous material, the conservation of energy implies that the amplitude of modes is preserved in time and space, except in one case. Let us take this opportunity to debunk a common misconception regarding the difference between the presence of losses and attenuation: the former implies the latter, but the latter is not always caused by the former. For example, energy is conserved in an isotropic medium with $\alpha = \beta = \gamma \leq 0$, yet electromagnetic waves cannot propagate in its bulk because the components of their wave vectors have complex values. Thus, at the interface with such a medium, refracted electromagnetic waves experience attenuation, leading to the phenomenon of evanescence. In

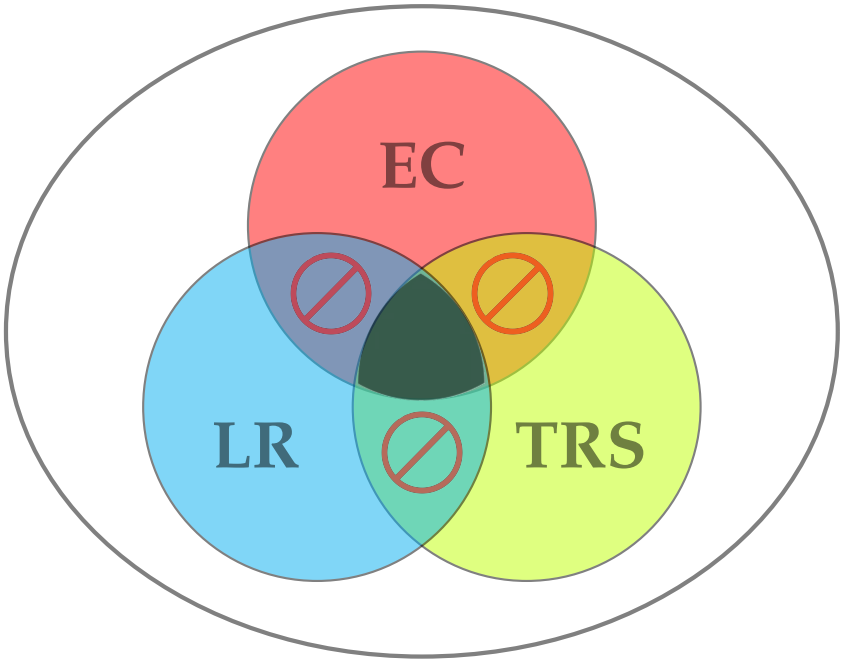

FIGURE 2.4: Subsets of electromagnetic media. Intersections between two colored subsets are forbidden, whereas the three-way intersection is allowed and corresponds to media where all three symmetries are preserved. Media that lack any symmetry lay in the white region within the large set.

this case, attenuation is not caused by losses, but is related to the total reflection of incident waves. In contrast, waves propagating in homogeneous media belonging to the other subsets, except the central intersection, undergo attenuation or exponential growth, caused by loss and gain, respectively. This is not necessarily true in inhomogeneous media: for instance, in the case of bulk waves, an alternating sequence of lossy and active slabs can support the propagation of a constant-amplitude wave over large distances [Arlouski and Novitsky, 2024]. Likewise, for surface modes, under specific conditions, an electromagnetic surface wave can travel along the interface between two half-spaces — one lossy and one with gain — without experiencing attenuation or exponential growth. Such phenomenon will be analyzed in Section 2.5.

For the blue and green subsets, the most general form of the dielectric tensor in each case is given by

$$\epsilon_{\text{LR}} = \begin{pmatrix} \alpha + i\lambda & \eta + i\kappa & \upsilon + i\nu \\ \eta + i\kappa & \beta + i\tau & \rho + i\sigma \\ \upsilon + i\nu & \rho + i\sigma & \gamma + i\phi \end{pmatrix}, \tag{2.24}$$

and

$$\epsilon_{\text{TRS}} = \begin{pmatrix} \alpha & \eta & \upsilon \\ \chi & \beta & \rho \\ \psi & \omega & \gamma \end{pmatrix}. \tag{2.25}$$

In both cases, the dyadics are not hermitian. If they can be diagonalized, their eigenvalues are generally complex, corresponding to decaying or growing waves. Combining the all three symmetries results in the following form

$$\boldsymbol{\epsilon}_{\mathrm{ALL}} = \begin{pmatrix} \alpha & \eta & \upsilon \\ \eta & \beta & \rho \\ \upsilon & \rho & \gamma \end{pmatrix}, \tag{2.26}$$

which describe general lossless crystals unaffected by (natural) gyrotropy. The last type of materials, namely those that lack any of the three symmetries, are generally described by 18 parameters, corresponding to the product of 9 matrix elements and two parts - real and imaginary. Obviously, it is necessary to emphasize that the latter are strictly related to each other by the Kramers-Kronig relations.

As for isotropic media, the limited degrees of freedom allow for only two possible scenarios. Since constitutive functions are diagonal tensors, all isotropic media inherently satisfy LR, regardless of the presence of losses or gain. However, losses and gain do influence the remaining two symmetry conditions: if $\mathrm{Im}[\epsilon, \mu] = 0$, both EC and TRS hold simultaneously (central dark region in Fig. 2.4); whereas if $\mathrm{Im}[\epsilon, \mu] \neq 0$, neither condition is satisfied (blue subset).

Finally, conditions are more stringent in the general case of a bi-anisotropic material. In addition to the constraints on $\boldsymbol{\epsilon}$ and $\boldsymbol{\mu}$, which are the same as in the anisotropic case, the magneto-electric coupling tensors must satisfy [Serdyukov et al., 2001b]

$$\begin{aligned} \boldsymbol{\xi}^{\dagger} = \boldsymbol{\zeta} \quad &\text{or} \quad \xi^{*}_{ji} = \zeta_{ij} && \text{EC}, \\ \boldsymbol{\xi}^{T} = -\boldsymbol{\zeta} \quad &\text{or} \quad \xi_{ji} = -\zeta_{ij} && \text{LR}, \\ \boldsymbol{\xi}^{*} = -\boldsymbol{\xi}, \quad \boldsymbol{\zeta}^{*} = -\boldsymbol{\zeta} \quad &\text{or} \quad \xi^{*}_{ij} = -\xi_{ij}, \quad \zeta^{*}_{ij} = -\zeta_{ij} && \text{TRS}. \end{aligned}$$

2.5 The Effects of Reciprocity

The purpose of this final section is to describe two novel configurations that illustrate the effects of reciprocity, which among the three electromagnetic symmetries is the most elusive and least intuitive.

Configurations similar to those examined here, characterized by the interplay between loss and gain, have been investigated in previous works, though restricted to bulk modes [Buddhiraju et al., 2020; Lannebère et al., 2025]. In this section, however, we provide an analysis of surface modes.

The first configuration involves two isotropic half-spaces with loss and gain, meaning they only satisfy Lorentz reciprocity. In fact, it is shown that the propagation of surface waves is identical for both forward and backward modes. Conversely, the second configuration consists of two media that do not possess any of the three

symmetries. As a result, only one type of mode, either forward or backward, can propagate.

Interestingly, in both cases, despite the fact that energy is not conserved locally, it is possible to find globally stable modes. This means that, under specific parameter conditions, energy is globally conserved when loss and gain are balanced.

2.5.1 Reciprocal system, bidirectional propagation

Consider two homogeneous and isotropic half-spaces, whose dielectric constants at a given frequency ω are given by $\epsilon_+ = \alpha + i\beta$ and $\epsilon_- = \gamma + i\delta$, where α, β, γ and δ are real numbers. The interface between the two half-spaces lies along the plane $z = 0$, as illustrated in Fig. 2.5. Since $\epsilon_\pm \in \mathbb{C}$, energy is not conserved locally, which means that the bulk modes grow or decay depending on the sign of the respective imaginary parts. However, at the interface, the interplay between loss and gain may lead to a balance between these effects, allowing the propagation of surface modes with constant amplitude, contrary to Zenneck waves [Zenneck, 1907]. Thus, the upcoming analysis aims to determine the values of the parameters defining the dielectric constants that permit the propagation of non-decaying electromagnetic waves along the interface. Naturally, the case $\beta = \delta = 0$ will be excluded, as it corresponds to SPPs, which propagate if $\alpha\gamma < 0$ and $\alpha < -\gamma$.

Referring to Fig. 2.5, let us consider a TM mode characterized by the magnetic field

$$\mathbf{H}_\pm = (H_0, 0, 0)\, e^{i(\mathbf{k}_\pm \cdot \mathbf{r} - \omega t)},$$

where the wave vectors are

$$\mathbf{k}_\pm = \begin{cases} (0, k_y, k_z^+) & z > 0, \\ (0, k_y, k_z^-) & z < 0. \end{cases}$$

As for the standard SPP, the components of the wave vectors can be shown to be [Maier, 2007]

$$k_y = \pm\sqrt{\frac{\epsilon_+\epsilon_-}{\epsilon_+ + \epsilon_-}}\,\frac{\omega}{c}, \tag{2.27a}$$

$$k_z^+ = \pm\frac{\epsilon_+}{\sqrt{\epsilon_+ + \epsilon_-}}\,\frac{\omega}{c}, \tag{2.27b}$$

$$k_z^- = \pm\frac{\epsilon_-}{\sqrt{\epsilon_+ + \epsilon_-}}\,\frac{\omega}{c}. \tag{2.27c}$$

Since the form of $\epsilon_\pm$ is the most general possible for isotropic media, the double sign in Eq. (2.27a) implies a fundamental property of this type of interface: if propagation to the right is allowed, propagation to the left will also be allowed. Moreover, the two kinds of propagation are spatial-inversion symmetric: this is precisely the definition of reciprocity. Indeed, as shown at the end of Section 2.4, all isotropic media are reciprocal. However, this generally does not hold for anisotropic media. In both the

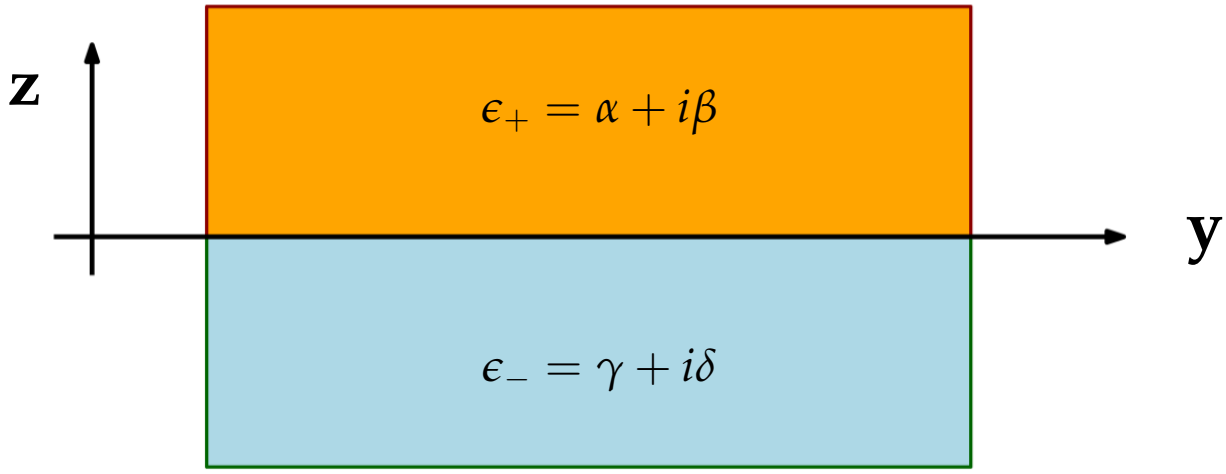

FIGURE 2.5: Interface between two generic isotropic half-spaces.

following example and the next chapter, we will analyze non-reciprocal cases where surface wave propagation is not symmetric under spatial inversion.

Since we are looking for a propagating surface wave, we have to impose that the quantity inside the square root in Eq. (2.27a) is real and positive. Real and imaginary parts can be written as

$$\mathrm{Re}\left[\frac{\epsilon_+\epsilon_-}{\epsilon_+ + \epsilon_-}\right] = \frac{\gamma(\alpha^2-\beta^2)+\alpha(\gamma^2-\delta^2)-2\beta\delta(\alpha+\gamma)}{(\alpha+\gamma)^2+(\beta+\delta)^2}, \tag{2.28}$$

$$\mathrm{Im}\left[\frac{\epsilon_+\epsilon_-}{\epsilon_+ + \epsilon_-}\right] = \frac{\beta(\delta^2-\gamma^2)+\delta(\beta^2-\alpha^2)-2\alpha\gamma(\beta+\delta)}{(\alpha+\gamma)^2+(\beta+\delta)^2}. \tag{2.29}$$

It can be seen that the numerator in the LHS in Eq. (2.29) is null if $\beta = -\delta$ and $\alpha = \pm\gamma$. Among such conditions, $\alpha = -\gamma$ also allows the denominator to be null, so it is not a suitable choice. Thus, Eq. (2.28) becomes

$$\mathrm{Re}\left[\frac{\epsilon_+\epsilon_-}{\epsilon_+ + \epsilon_-}\right] = \frac{\alpha^2+\beta^2}{2\alpha}, \tag{2.30}$$

so we require $\alpha > 0$. Moreover, the z-components become

$$k_z^+ = \pm\frac{1}{\sqrt{2\alpha}}\,(\alpha+i\beta)\,\frac{\omega}{c}, \tag{2.31}$$

$$k_z^- = \pm\frac{1}{\sqrt{2\alpha}}\,(\alpha-i\beta)\,\frac{\omega}{c}. \tag{2.32}$$

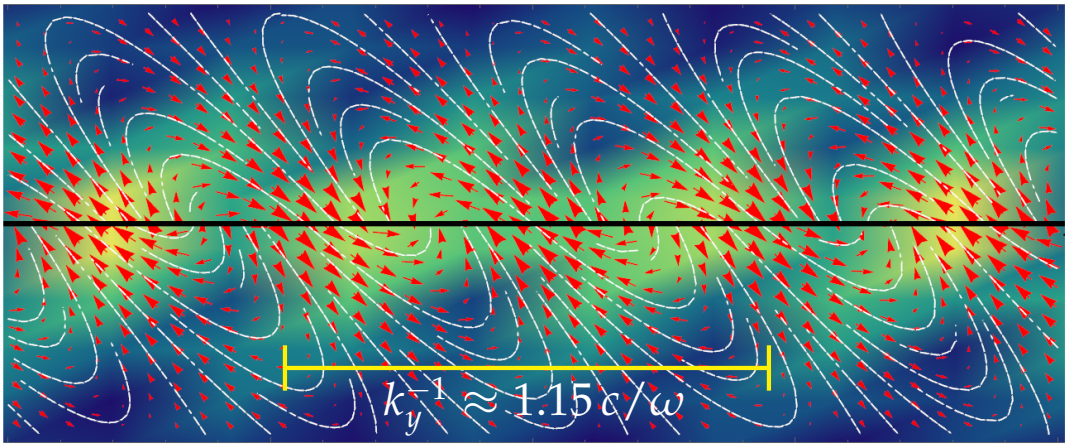

FIGURE 2.6: Electric field distribution for rightward propagation with $\alpha = 1$ and $\beta = 0.5$.

Finally, since the confinement conditions translate into $\mathrm{Im}[k_z^+] > 0$ and $\mathrm{Im}[k_z^-] < 0$, the mode sought is characterized by

$$k_y = \pm\sqrt{\frac{\alpha^2+\beta^2}{2\alpha}}\,\frac{\omega}{c}, \quad k_z^{\pm} = \frac{1}{\sqrt{2\alpha}}\,(\alpha \pm i\beta)\,\frac{\omega}{c} \quad \text{with } \alpha > 0, \text{ if } \beta > 0, \tag{2.33}$$

$$k_y = \pm\sqrt{\frac{\alpha^2+\beta^2}{2\alpha}}\,\frac{\omega}{c}, \quad k_z^{\pm} = -\frac{1}{\sqrt{2\alpha}}\,(\alpha \pm i\beta)\,\frac{\omega}{c} \quad \text{with } \alpha > 0, \text{ if } \beta < 0. \tag{2.34}$$

The electric field distribution is shown in Fig. 2.6. Notably, unlike SPPs, the field lines are tilted relative to the vertical direction. This behavior is precisely in line with Zenneck's prediction of his eponymous waves, which propagate along the interface between a lossy metal and a lossless dielectric.

An additional peculiarity of these modes is related to the energetic aspect. In the case $\alpha, \beta > 0$, the time-averaged Poynting vector is given by

$$\langle \mathbf{S}_\pm \rangle = \frac{1}{2}\,\mathrm{Re}\left[\mathbf{E} \times \mathbf{H}^*\right] = \frac{H_0^2}{2\sqrt{2\alpha}\,\epsilon_0\, c}\left(\frac{\alpha}{\sqrt{\alpha^2+\beta^2}}\,\hat{y} + \hat{z}\right) e^{\mp \frac{2\omega\beta}{\sqrt{2\alpha}\,c}\,z}, \tag{2.35}$$

where the component along z indicates the presence of a vertical energy flow. Indeed, this energy transfer is precisely the factor that enables the propagation of a stable and confined mode: energy is generated in the gain medium and dissipated in the lossy medium. The perfect balance between creation and dissipation rates ensures that the electromagnetic energy is globally conserved, even though it is not locally conserved.

It is important to note that the results in Eqs. (2.33) to (2.35) do not tend to the SPP limit when the dielectric constants are real. In fact, the limit $\beta \to 0$ corresponds to a homogeneous space, which inherently does not support surface wave propagation.

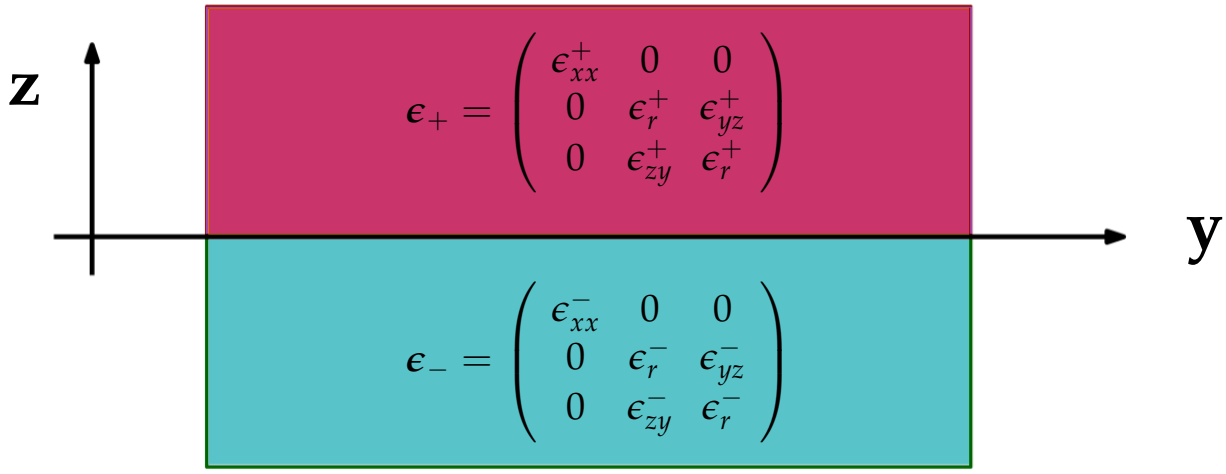

FIGURE 2.7: Interface between the two anisotropic half-spaces.

2.5.2 Non-reciprocal system, unidirectional propagation

Following the approach used in Section 2.5.1, we now look for modes localized at the interface between two anisotropic media described by asymmetric dielectric tensors, as illustrated in Fig. 2.7.
By focusing on TM waves, the dispersion relations of bulk waves read

$$\epsilon_r^\pm \left[k_y^2 + (k_z^\pm)^2\right] + k_y k_z^\pm \left(\epsilon_{yz}^\pm + \epsilon_{zy}^\pm\right) + \epsilon_{yz}^\pm \epsilon_{zy}^\pm - (\epsilon_r^\pm)^2 = 0, \tag{2.36}$$

whereas, the continuity of E_y implies the continuity of

$$\frac{\epsilon_r^\pm k_z^\pm + \epsilon_{yz}^\pm k_y}{\epsilon_{yz}^\pm \epsilon_{zy}^\pm - (\epsilon_r^\pm)^2}.$$

To simplify the calculations, it is possible to use the sufficient conditions $\epsilon_r^+ = \epsilon_r^-$ and $\epsilon_{yz}^+ \epsilon_{zy}^+ = \epsilon_{yz}^- \epsilon_{zy}^-$. Hence, by defining $\epsilon_{yz}^+ = \epsilon_{zy}^- \equiv A$ and $\epsilon_{yz}^- = \epsilon_{zy}^+ \equiv B$, the continuity condition reduces to

$$\epsilon_r k_z^+ + A k_y = \epsilon_r k_z^- + B k_y. \tag{2.37}$$

Equations (2.36) and (2.37) admit four distinct solutions

$$k_y = 0, \qquad k_z^+ = \frac{\omega}{c}\sqrt{\epsilon_r - \frac{AB}{\epsilon_r}}, \qquad k_z^- = \frac{\omega}{c}\sqrt{\epsilon_r - \frac{AB}{\epsilon_r}}, \tag{2.38a}$$

$$k_y = 0, \qquad k_z^+ = -\frac{\omega}{c}\sqrt{\epsilon_r - \frac{AB}{\epsilon_r}}, \qquad k_z^- = -\frac{\omega}{c}\sqrt{\epsilon_r - \frac{AB}{\epsilon_r}}, \tag{2.38b}$$

$$k_y = -\frac{\omega}{c}\sqrt{\epsilon_r}, \qquad k_z^+ = \frac{\omega}{c}\frac{A}{\sqrt{\epsilon_r}}, \qquad k_z^- = \frac{\omega}{c}\frac{B}{\sqrt{\epsilon_r}}, \tag{2.38c}$$

$$k_y = \frac{\omega}{c}\sqrt{\epsilon_r}, \qquad k_z^+ = -\frac{\omega}{c}\frac{A}{\sqrt{\epsilon_r}}, \qquad k_z^- = -\frac{\omega}{c}\frac{B}{\sqrt{\epsilon_r}}. \tag{2.38d}$$

Solutions in Eqs. (2.38a) and (2.38b) correspond to radiative modes, which are not confined on the interface. Conversely, solutions Eqs. (2.38c) and (2.38d) are strong candidates for confined and propagating modes. The final conditions to be imposed are $\mathrm{Im}(k_z^+) > 0$ and $\mathrm{Im}(k_z^-) < 0$, which are satisfied by the solution described in Eq. (2.38c) if $A = i\eta$ and $B = -i\nu$, where $\eta, \nu > 0$. Thus, if the dielectric tensors characterizing the system read

$$\boldsymbol{\epsilon}_+ = \begin{pmatrix} \epsilon_{xx}^+ & 0 & 0 \\ 0 & \epsilon_r & i\eta \\ 0 & -i\nu & \epsilon_r \end{pmatrix}, \qquad \boldsymbol{\epsilon}_- = \begin{pmatrix} \epsilon_{xx}^- & 0 & 0 \\ 0 & \epsilon_r & -i\nu \\ 0 & i\eta & \epsilon_r \end{pmatrix}, \tag{2.39}$$

then the system supports the propagation of surface modes with $k_y < 0$. Propagation in the opposite direction is forbidden because Eq. (2.38d) would not imply interface confinement. This is a consequence of the lack of reciprocity:[12] it can be observed that, according to the results discussed in Section 2.4, the tensors in Eq. (2.39) belong to the fifth type of materials, indicating that none of the three symmetries are locally preserved in the system. Despite the lack of local energy conservation, these modes can still propagate indefinitely on the interface, as for those found in Section 2.5.1.

In this case, according to the solution in Eq. (2.38c), the electric field and the corresponding time-averaged Poynting vector are given by

$$\begin{aligned}
\mathbf{E}_+(y,z,t) &= -\frac{H_0}{\epsilon_0\sqrt{\epsilon_r}\,c}\, e^{-i\omega\left(\frac{\sqrt{\epsilon_r}}{c}y+t\right)}\, e^{-\frac{\omega\eta}{c\sqrt{\epsilon_r}}z}\,\hat{z}, \\
\langle \mathbf{S}_+\rangle(z) &= -\frac{H_0^2}{2\epsilon_0\sqrt{\epsilon_r}\,c}\, e^{-\frac{2\omega\nu}{c\sqrt{\epsilon_r}}z}\,\hat{y}, \\
\mathbf{E}_-(y,z,t) &= -\frac{H_0}{\epsilon_0\sqrt{\epsilon_r}\,c}\, e^{-i\omega\left(\frac{\sqrt{\epsilon_r}}{c}y+t\right)}\, e^{+\frac{\omega\eta}{c\sqrt{\epsilon_r}}z}\,\hat{z}, \\
\langle \mathbf{S}_-\rangle(z) &= -\frac{H_0^2}{2\epsilon_0\sqrt{\epsilon_r}\,c}\, e^{+\frac{2\omega\nu}{c\sqrt{\epsilon_r}}z}\,\hat{y}.
\end{aligned}$$

This implies that the electric field lines are straight and vertical, while the energy flow is parallel to the in-plane wave vector $k_y = -\omega\sqrt{\epsilon_r}/c$.

Finally, it should be mentioned that the results just found also hold for hermitian tensors. In fact, the limit $\eta \to \nu$ corresponds to a space composed of two lossless gyrotropic media, which inherently support unidirectional surface wave propagation. The asymmetry between forward and backward propagating modes at the interface with gyrotropic media will emerge again in the next chapter, where specific configurations of low-symmetry systems will be analyzed.

[12] It is important to keep in mind that the lack of reciprocity is a necessary (but not sufficient) condition for the asymmetry between forward and backward propagation. In fact, even if the dielectric tensor is asymmetric, there can still be particular polarizations that are not affected by the asymmetric elements, and therefore do not distinguish between the two directions of propagation.

More broadly, balanced gain-loss structures on the lines of those proposed in Sections 2.5.1 and 2.5.2 have been explored in the context of PT-symmetric photonics [Zyablovsky et al., 2014], where they lead to applications in optical isolation, coherent perfect absorption and novel laser designs. PT-symmetric systems, which remain invariant under the combined action of parity and time-reversal transformations, provide a framework to study non-Hermitian physics while still supporting real eigenvalues under particular conditions [Feng, El-Ganainy, and Ge, 2017].

Chapter 3

Electromagnetic Modes in Gyro-Hyperbolic Structures

This chapter presents a comprehensive study of electromagnetic surface waves in structures combining gyrotropic and hyperbolic media. We investigate how the simultaneous presence of anisotropy and gyrotropy gives rise to new classes of non-reciprocal surface modes with distinctive dispersion and energy flow characteristics. Analytical and numerical methods reveal that these modes exhibit directional propagation, enhanced field penetration and tilted field profiles not found in conventional systems [Provenzano and La Rocca, 2023]. In addition to single-interface configurations, we examine one-dimensional photonic crystals composed of alternating gyroelectric and uniaxial layers, uncovering intermediate surface waves with tunable forward or backward group velocities. The photonic band structure is shown to be dynamically controllable via external magnetic fields, influencing both bulk and surface states [Provenzano and La Rocca, 2024].

3.1 Introduction

In Chapter 1, we introduced the concept of electromagnetic surface waves and discussed their most important and well-known types, the majority of which were considered in the context of isotropic interfaces.

When at least one of the interfacing materials is anisotropic, the physics of surface waves becomes even more intricate. In particular, the introduction of birefringence or gyrotropy enables novel surface wave phenomena. Notably, *Dyakonov Waves* (DWs) can propagate at the boundary between an isotropic dielectric and a uniaxial crystal with the optical axis lying in the plane of the interface [Dyakonov, 1988]. These hybrid-polarized waves exist only within a narrow angular range, dictated by the orientation of the optical axis. If one of the media possesses metal-like permittivities, DWs evolve into *Dyakonov Plasmons* (DPs) [Narimanov, 2014; Takayama, Bogdanov, and Lavrinenko, 2017], inheriting the strong field localization of SPPs and the directional characteristics of DWs. As for gyrotropy, typically induced by external magnetic fields, things are even more peculiar. In gyrotropic media,

the lack of both Lorentz reciprocity and time-reversal symmetry leads to nonreciprocal propagation, that is, the dispersion relation of forward modes is different from backward modes [Camley, 1987; Alexander and Barkovsky, 2006; Alexander and Barkovsky, 2008]. This opens new avenues for designing one-way surface waveguides and isolators. While several studies have investigated ESWs involving gyrotropic or anisotropic materials separately [Polo, Mackay, and Lakhtakia, 2013; Polo, Nelatury, and Lakhtakia, 2007; Lakhtakia, Mackay, and Zhou, 2020; Zhou, Mackay, and Lakhtakia, 2020; Cojocaru, 2015], the combined effects of anisotropy and gyrotropy remain relatively unexplored.

The first part of this chapter, we focus on electromagnetic surface modes localized at the interface between a gyrotropic medium and a uniaxial material. In particular, we examine the case in which the uniaxial material exhibits hyperbolic dispersion, behaving as a Hyperbolic Medium (HM). We demonstrate that the anisotropy of the HM is responsible for a tilted field distribution akin to that observed in ZWs. Additionally, we show that gyrotropy not only introduces non-reciprocity in the dispersion relations but also leads to the emergence of multiple surface modes. A realistic configuration composed of indium antimonide (InSb) and a stack of graphene layers is analyzed, revealing conditions under which such new modes could be observed and potentially exploited.

In the second part, we analyze what happens to the electromagnetic modes as the number of interfaces increases, eventually forming photonic crystals.

As discussed in Chapter 1, considerable interest has been devoted to PhCs due to their ability to control light flow [Joannopoulos et al., 2008; Inoue and Ohtaka, 2004]. While isotropic PhCs offer well-established properties, the incorporation of anisotropic media introduces direction-dependent refractive indices and polarization responses, giving rise to phenomena such as Faraday rotation in gyrotropic materials [Landau and Lifshitz, 1984; Zangwill, 2012]. As a result, PhCs composed of anisotropic constituents provide a powerful platform for tunable and reconfigurable photonic devices [Alagappan et al., 2006b; Alagappan et al., 2006a; Fesenko et al., 2008; Vytovtov and Mospan, 2011]. External electric or magnetic fields can be employed to control band gap features, such as their position or width, especially in systems involving liquid crystals or gyrotropic media [Kim and Kurihara, 2018].

Beyond bulk propagation, PhCs are capable of supporting surface-bound modes, including Tamm waves and Bloch surface waves [Lakhtakia, Mackay, and Zhou, 2020; Polo, Mackay, and Lakhtakia, 2013; Bashiri et al., 2019; Wang et al., 2009; Akjouj et al., 2021; Martorell, Sprung, and Morozov, 2006; Barvestani, Kalafi, and Vala, 2007; Feng et al., 2005; Jacob and Narimanov, 2008; Pérez Huerta et al., 2018]. When such structures incorporate gyroelectric and uniaxial layers, novel ESWs can emerge. In this context, we analyze a one-dimensional PhC made of alternating lossless gyroelectric and uniaxial layers. Previous works have treated these media separately [Narimanov, 2014; Zhao, luo, and Zhou, 2007], but their combination remains largely unexplored.

Our investigation shows that when the uniaxial layers act as Hyperbolic Materials,

new types of ESWs can propagate at the surface of the crystal. These modes exhibit either forward or backward propagation—associated with positive or negative group velocities—depending on the specific hyperbolic dispersion. This behavior is particularly promising for the realization of devices with controllable propagation direction. Moreover, these surface waves possess significantly higher penetration depths than traditional Tamm waves or SPPs, suggesting their potential to control signal transmission through the surface rather than the bulk modes.

Importantly, we demonstrate that gyrotropy significantly modifies the photonic band structure. By varying the external magnetic field, one can dynamically shift or reshape the frequency bands allowed within the structure. We also examine a finite-size version of the system under an Otto configuration, where reflection spectra reveal clear signatures of surface mode excitation. In particular, near-zero reflection correlates with non-trivial values of the *Goos–Hänchen shift* (GHS), which can be either positive or negative depending on the group velocity of the excited mode. Finally, we highlight how breaking symmetry in the layer arrangement leads to reflectivity that is asymmetric with respect to the sign of the incidence angle—another manifestation of gyrotropy-induced non-reciprocity.

The results discussed in this chapter have been published in two papers [Provenzano and La Rocca, 2023; Provenzano and La Rocca, 2024]. Together, they provide a comprehensive picture of how anisotropy and gyrotropy can be harnessed to control surface-bound electromagnetic modes, both at simple interfaces and within periodic photonic structures. For analytical convenience, we will examine in detail those non-trivial cases that can be addressed through exact methods, followed by numerical results for more complex configurations.

3.2 Surface Waves Propagating Between Two Semi-Infinite Media

Let us analyze the propagation of surface waves at the interface between a gyroelectric and a uniaxial medium (possibly a HM), as outlined in Fig. 3.1. We chose to consider a gyroelectric medium in the so-called *Voigt configuration*, such that in our coordinate system its dielectric tensor reads

$$\boldsymbol{\epsilon}_{\text{gyro}} = \epsilon_0 \begin{pmatrix} \epsilon_B & 0 & 0 \\ 0 & \epsilon_g & ig \\ 0 & -ig & \epsilon_g \end{pmatrix}, \tag{3.1}$$

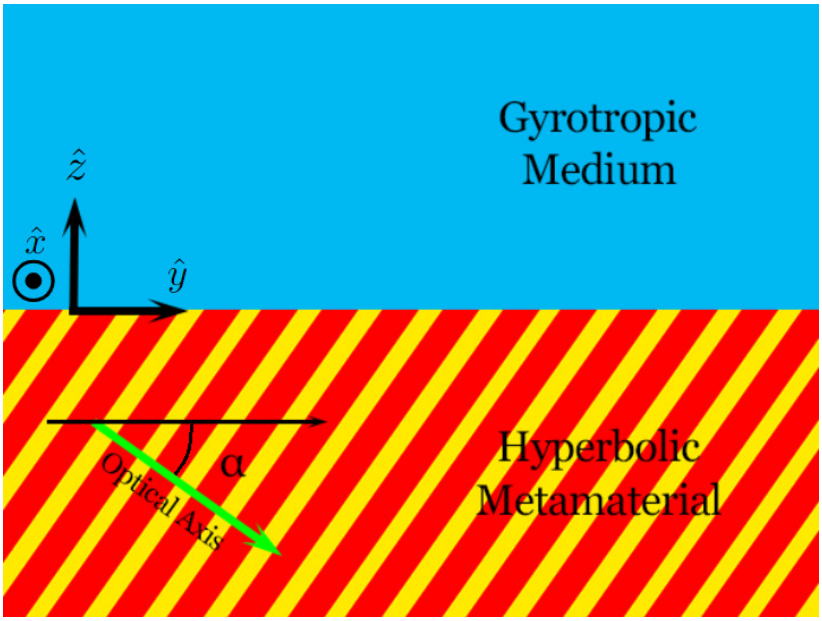

FIGURE 3.1: Outline of the interface between a gyroelectric medium and a hyperbolic medium. The green line represents the direction of the optical axis of the hyperbolic medium.

which is equivalent to considering an external magnetic field pointing towards the x-axis. As for the uniaxial medium, its dielectric tensor was chosen to be

$$\epsilon'_u = \epsilon_0 \begin{pmatrix} \epsilon_\perp & 0 & 0 \\ 0 & \epsilon_\parallel & 0 \\ 0 & 0 & \epsilon_\perp \end{pmatrix}, \tag{3.2}$$

in its principal coordinate system. We consider the configuration wherein the optical axis is neither parallel nor perpendicular to the interface between the two media, as shown in Fig. 3.1. Hence, we have to rotate the dielectric tensor by means of the rotation matrix

$$R_x(\alpha) = \begin{pmatrix} 1 & 0 & 0 \\ 0 & \cos\alpha & \sin\alpha \\ 0 & -\sin\alpha & \cos\alpha \end{pmatrix}. \tag{3.3}$$

In our coordinate system, the uniaxial dielectric tensor reads

$$\boldsymbol{\epsilon}_u = R_x(\alpha)\, \boldsymbol{\epsilon}'_u\, R_x(-\alpha) = \epsilon_0 \begin{pmatrix} \epsilon_{xx} & 0 & 0 \\ 0 & \epsilon_{yy} & \epsilon_{yz} \\ 0 & \epsilon_{zy} & \epsilon_{zz} \end{pmatrix}, \tag{3.4}$$

where the matrix elements are

$$\begin{cases} \epsilon_{xx} = \epsilon_{\perp}, \\ \epsilon_{yy} = \epsilon_{\perp} \sin^2 \alpha + \epsilon_{\parallel} \cos^2 \alpha, \\ \epsilon_{yz} = \epsilon_{zy} = \left(\epsilon_{\perp} - \epsilon_{\parallel}\right) \sin \alpha \cos \alpha, \\ \epsilon_{zz} = \epsilon_{\perp} \cos^2 \alpha + \epsilon_{\parallel} \sin^2 \alpha. \end{cases} \tag{3.5}$$

The condition for a surface wave to exist is that it must be evanescent far from the interface; thus, in both regions, the wave vectors must have an imaginary z-component. Assuming propagation along $\hat{y}$ and following the $\exp\left[+i(\mathbf{k} \cdot \mathbf{r} - \omega t)\right]$ convention, we seek modes with real ω and k_y. Therefore, the wave vectors are given by:

$$\mathbf{k_1} = \left(0, k_y, i\beta_1\right), \tag{3.6}$$

$$\mathbf{k_2} = \left(0, k_y, -i\beta_2\right), \tag{3.7}$$

where the subscript "1" stands for the gyroelectric medium ($z > 0$), whereas "2" for the uniaxial medium ($z < 0$) and $\mathrm{Re}\{\beta_1\},\ \mathrm{Re}\{\beta_2\} > 0$. The main feature of our configuration is that TE and TM modes are not coupled, hence they obey the following dispersion relations

$$\begin{cases} k_y^2 - \beta_1^2 = \frac{\omega^2}{c^2} \epsilon_B, \\ k_y^2 - \beta_2^2 = \frac{\omega^2}{c^2} \epsilon_{\perp}, \end{cases} \tag{3.8}$$

$$\begin{cases} k_y^2 - \beta_1^2 = \frac{\omega^2}{c^2} \frac{\epsilon_g^2 - g^2}{\epsilon_g}, \\ \epsilon_{yy} k_y^2 - \epsilon_{zz} \beta_2^2 - 2ik_y \beta_2 \epsilon_{yz} = \frac{\omega^2}{c^2} \epsilon_{\parallel} \epsilon_{\perp}, \end{cases} \tag{3.9}$$

where Eq. (3.8) hold for TE modes, whereas Eq. (3.9) rule the TM-modes propagation. As for TE modes, a simple calculation shows that the condition for evanescence $\mathrm{Re}\{\beta_1\},\ \mathrm{Re}\{\beta_2\} > 0$ is never satisfied for any value of the parameters, as for standard SPPs. Hence TE surface waves cannot propagate at the interface under consideration. Thus, our discussion will be focused on TM modes, characterized by the triplet (E_y, E_z, H_x). The magnetic field reads

$$\mathbf{H}_1 = (H_0, 0, 0)\, e^{ik_y y - \beta_1 z - i\omega t} \qquad z > 0, \tag{3.10}$$

$$\mathbf{H}_2 = (H_0, 0, 0)\, e^{ik_y y + \beta_2 z - i\omega t} \qquad z < 0. \tag{3.11}$$

We can evaluate the components of the electric field by means of Maxwell's equations:

$$\mathbf{E}_1 = \frac{H_0 e^{ik_y y + \beta_2 z - i\omega t}}{\omega \epsilon_0 (\epsilon_g^2 - g^2)} \left(0,\ -i\epsilon_g \beta_1 - igk_y,\ \epsilon_g k_y + g\beta_1\right), \tag{3.12}$$

$$\mathbf{E}_2 = \frac{H_0 e^{ik_y y+\beta_2 z-i\omega t}}{\omega\epsilon_0\epsilon_{\parallel}\epsilon_{\perp}}\,(0,\; i\epsilon_{zz}\beta_2 - \epsilon_{yz}k_y,\; \epsilon_{yy}k_y - i\epsilon_{yz}\beta_2). \tag{3.13}$$

By applying the continuity of E_y, we find the further condition

$$\epsilon_{\parallel}\epsilon_{\perp}(gk_y + \epsilon_g\beta_1) + (\epsilon_g^2 - g^2)(i\epsilon_{yz}k_y + \epsilon_{zz}\beta_2) = 0, \tag{3.14}$$

which governs the propagation of the surface wave together with Eq. (3.9). These last two equations can be solved for β_1 and β_2, under the assumptions $\epsilon_g > g > 0$[1] and $\epsilon_{\perp}\epsilon_{\parallel} < 0$, as for HMs:

$$\beta_1 = \sqrt{k_y^2 - \epsilon_v\frac{\omega^2}{c^2}}, \tag{3.15}$$

$$\beta_2 = -i\,\frac{\epsilon_{yz}}{\epsilon_{zz}}\,k_y + \frac{1}{|\epsilon_{zz}|}\sqrt{\epsilon_{\parallel}\epsilon_{\perp}\left(k_y^2 - \epsilon_{zz}\frac{\omega^2}{c^2}\right)}, \tag{3.16}$$

where we defined $\epsilon_v \equiv (\epsilon_g^2 - g^2)/\epsilon_g$. Generally β_2 is a complex number, but evanescence is guaranteed in the anisotropic bulk, provided that $\mathrm{Re}\{\beta_2\} > 0$. Keeping in mind that we are looking for solutions with both ω and k_y real, the only way for the ESW to exist is considering β_2 as already divided in its real and imaginary parts, as written in Eq. (3.16). Thus, the quantity inside the square root must be positive. Hence

$$\epsilon_{\parallel}\epsilon_{\perp}\left(k_y^2 - \epsilon_{zz}\frac{\omega^2}{c^2}\right) > 0 \qquad \overset{\epsilon_{\perp}\epsilon_{\parallel}<0}{\Longrightarrow} \qquad k_y^2 < \epsilon_{zz}\frac{\omega^2}{c^2}.$$

In addition, we should also require β_1 to be real and positive

$$\beta_1 > 0 \qquad \Longrightarrow \qquad k_y^2 > \epsilon_v\frac{\omega^2}{c^2}.$$

Combining the last two conditions yields $\epsilon_{zz} > \epsilon_v$, which implies $(\epsilon_{\perp} - \epsilon_{\parallel})\cos^2\alpha > \epsilon_v - \epsilon_{\parallel}$. At this point there are two possible cases:

(a) $\epsilon_{\perp} > 0$, $\epsilon_{\parallel} < 0 \Longrightarrow \cos^2\alpha > \frac{\epsilon_v - \epsilon_{\parallel}}{\epsilon_{\perp} - \epsilon_{\parallel}}$. The condition $0 < \cos^2\alpha < 1$ yields $\epsilon_{\perp} > \epsilon_v$.

(b) $\epsilon_{\perp} < 0$, $\epsilon_{\parallel} > 0 \Longrightarrow \cos^2\alpha < \frac{\epsilon_v - \epsilon_{\parallel}}{\epsilon_{\perp} - \epsilon_{\parallel}}$. The condition $0 < \cos^2\alpha < 1$ yields $\epsilon_{\parallel} > \epsilon_v$.

Solving Eqs. (3.14) to (3.16) for k_y, we find

$$k_y(\omega) = \overset{+}{-}\,\frac{\omega}{c}\sqrt{\frac{\epsilon_{zz}(\epsilon_g^2-g^2)^2+\epsilon_g(\epsilon_{\perp}\epsilon_{\parallel})^2-\epsilon_{\perp}\epsilon_{\parallel}\left[\epsilon_g(\epsilon_g^2-g^2)+\epsilon_{zz}(\epsilon_g^2+g^2)\right]\overset{+}{-}\Delta}{(\epsilon_g^2-g^2)^2+(\epsilon_{\perp}\epsilon_{\parallel})^2-2\epsilon_{\perp}\epsilon_{\parallel}(\epsilon_g^2+g^2)}} \tag{3.17}$$

[1] The condition $g < \epsilon_g$ guarantees modes propagation in the gyroelectric medium.

where

$$\Delta = 2g\epsilon_g \left|\epsilon_\perp \epsilon_\parallel\right| \sqrt{\epsilon_{zz}^2 + \epsilon_\perp \epsilon_\parallel - \epsilon_{zz}\epsilon_g + \frac{\epsilon_{zz}}{\epsilon_g}\left(g^2 - \epsilon_\perp \epsilon_\parallel\right)}.$$

Equation (3.17) represents the dispersion relation of the surface wave.[2] It is to be remarked that the choice of the sign of $\pm\Delta$ in Eq. (3.17) corresponds to the choice of the sign of k_y, resulting in non-degenerate forward and backward propagating waves. In particular, $+\Delta$ corresponds to forward modes ($k_y > 0$), whereas $-\Delta$ corresponds to backward modes ($k_y < 0$). This is a typical non-reciprocal feature resulting from the presence of an external magnetic field: lossless gyrotropic media, such as the one considered in this section, belong to the red subset of Fig. 2.4. By contrast, lossless uniaxial media respect all three fundamental symmetries described in Chapter 2 and, thus, belong to the black subset. Overall, the system under consideration, which is the combination of both media, is non-reciprocal, and it is therefore expected that the behavior of surface waves depends on the direction in which they travel, as anticipated in Section 2.5.2.

If both media do not exhibit dispersion, Eq. (3.17) reduces to a straight line on the $\omega - k_y$ plane. Instead, we assume that the HM has metal-like permittivities, i.e. we consider

$$\epsilon_\parallel = \epsilon_\perp \left(1 - \frac{\omega_p^2}{\omega^2}\right),$$

as for case (a).[3] Three typical dispersion diagrams are shown in Fig. 3.2, wherein the red plot represents the case of non-gyrotropy. As we switch gyrotropy on, depending on the sign of the off-diagonal element g, the solution may assume a kink-behavior, hence there are two distinct regimes characterized by different values of the group velocity. The region of the plot we are interested in is for $\omega < \omega_p$ because the remaining part does not respect the assumption $\epsilon_\parallel \epsilon_\perp < 0$. In this regime, we notice that all plots end up in the same point on the $\omega = \omega_p$ line, regardless of the amount of gyrotropy affecting the system. This is due to the fact that $\epsilon_\parallel(\omega = \omega_p) = 0$. Such value of $\epsilon_\parallel$ lets Eq. (3.17) reduce to

$$|k_y(\omega = \omega_p)| = \frac{\omega_p}{c}\sqrt{\epsilon_{zz}(\omega = \omega_p)}, \tag{3.18}$$

which no longer depends on g. For $\omega > \omega_p$, the existence conditions that let the surface wave have both ω and k_y real can no longer be satisfied.

3.2.1 Energy flow

Building on the expressions for the electric and magnetic fields derived in the previous section, we now evaluate the time-averaged Poynting vector, defined as

[2] In the particular case where $g = 0$ and $\epsilon_\perp = \epsilon_\parallel < 0$, Eq. (3.17) reduces to the dispersion relation of the SPP propagating through a metal-dielectric interface.

[3] Case (b) shows similar features, hence it will not be investigated in detail here.

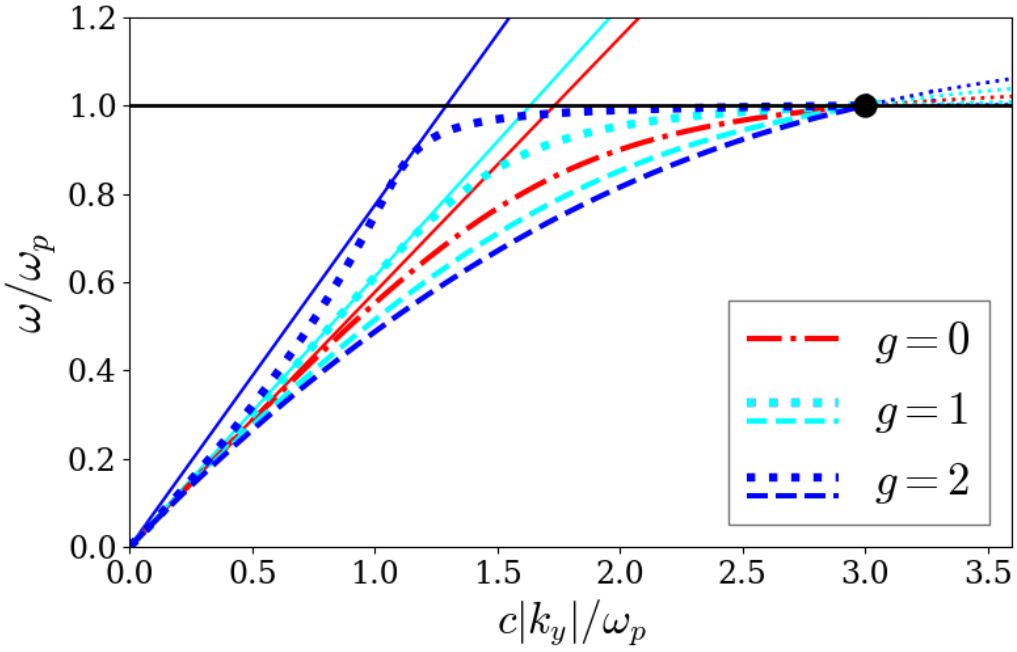

FIGURE 3.2: Typical dispersion diagrams of a surface wave traveling through the interface between a gyroelectric medium and an HM (the parameters used for illustrative purposes are $\epsilon_g = 3$ and $\epsilon_\perp = 9$). The solid straight lines represent the light dispersion in the gyroelectric medium. Dotted and dashed lines of the same color refer to the same value of g, but are distinguished by the $\pm$ sign in Eq. (3.17), and thus describe forward- or backward-propagating modes. In particular, each upper branch represents a forward mode, whereas each lower branch represents a backward mode. The red curve describes the case with no gyrotropy, hence its corresponding wave can propagate in both directions. It is to be noted that for $\omega > \omega_p$ all curves shown no longer correspond to physically acceptable solutions, but rather represent the real part of an in-plane wave-vector k_y which is no longer real.

$\langle \mathbf{S} \rangle \equiv \frac{1}{2} \operatorname{Re}\{\mathbf{E} \times \mathbf{H}^*\}$. It follows that

$$\langle \mathbf{S}_1 \rangle = \frac{H_0^2 e^{-2\operatorname{Re}\{\beta_1\}z}}{2\omega\epsilon_0(\epsilon_g^2 - g^2)} \operatorname{Re}\{(0,\ \epsilon_g k_y + g\beta_1,\ i\epsilon_g\beta_1 - igk_y)\}, \tag{3.19}$$

$$\langle \mathbf{S}_2 \rangle = \frac{H_0^2 e^{2\operatorname{Re}\{\beta_2\}z}}{2\omega\epsilon_0\epsilon_\parallel\epsilon_\perp} \operatorname{Re}\{(0,\ \epsilon_{yy}k_y - i\epsilon_{yz}\beta_2,\ \epsilon_{yz}k_y - i\epsilon_{zz}\beta_2)\}. \tag{3.20}$$

The existence conditions in Eqs. (3.14) to (3.16) let the time-averaged Poynting vector point towards $\hat{y}$, in particular

$$\langle \mathbf{S} \rangle = \begin{cases} \frac{H_0^2(\epsilon_g k_y + g\beta_1)}{2\omega\epsilon_0(\epsilon_g^2 - g^2)} e^{-2\beta_1 z}\, \hat{y} & z > 0, \\ \\ \frac{H_0^2 k_y}{2\epsilon_0\epsilon_{zz}\omega} e^{2\operatorname{Re}\{\beta_2\}z}\, \hat{y} & z < 0. \end{cases} \tag{3.21}$$

Thus, the flow of energy is correctly directed along the boundary, which guarantees an in-plane flow of energy. We notice that for $z > 0$ the energy flows towards $+\hat{y}$ for any value of the parameters, whereas in the lower half-space it can point towards $-\hat{y}$ if $\epsilon_{zz} < 0$. Overall, the total flux of energy is

$$\langle \mathcal{F} \rangle = \int_{-\infty}^{\infty} \langle \mathbf{S} \rangle \, \mathrm{d}z = \frac{H_0^2}{4\epsilon_0 \omega} \left[\frac{g}{\epsilon_g \epsilon_v} + k_y \left(\frac{1}{\epsilon_v \beta_1} + \frac{1}{\epsilon_{zz} \operatorname{Re}\{\beta_2\}} \right) \right] \hat{y}.$$

Depending on the parameters we choose to consider, $\langle \mathcal{F} \rangle$ may be opposite to the direction of propagation.[4] In particular, this happens if

$$0 > \frac{1}{\epsilon_{zz}} > -\frac{\operatorname{Re}\{\beta_2\}}{\epsilon_v} \left\{ \frac{1}{\beta_1} + \frac{g}{\epsilon_g k_y} \right\}, \tag{3.22}$$

leading to negative values of the group velocity.

We can prove an important result related to the field distribution in such systems. Let us focus our attention on the electric field lines in both upper and lower media. To do so, we have to consider the physical fields, represented by the real parts of Eqs. (3.12) and (3.13), and then derive the equation describing the field lines in the yz plane by means of

$$\frac{\mathrm{d}z}{\mathrm{d}y}(y,t) = \frac{\operatorname{Re}\{E_z(z,y,t)\}}{\operatorname{Re}\{E_y(z,y,t)\}}. \tag{3.23}$$

It turns out that the field lines in the gyroelectric medium are the same as the standard SPPs propagating between dielectric and metal. As for the HM, the field lines cannot be analytically evaluated if $\epsilon_{yz} \neq 0$, but the numerical results, obtained by solving Eq. (3.23) using Wolfram Mathematica, are shown in Fig. 3.3. We notice a tilted behavior of the lines in the lower medium, which recalls the characteristic profile of the ZW [Oruganti et al., 2020; Jangal et al., 2016], even though we did not consider any lossy dielectric function. In addition, the tilted behavior of the lines disappears when the off-diagonal element ϵ_{yz} is null, thus we can conclude that only anisotropy is responsible for this peculiar phenomenon. Adding some absorption would make the lines sink towards the interface, as for ZWs [Oruganti et al., 2020; Jangal et al., 2016].

The analytical results we derived in this section could be used to study less general situations by assigning proper values to the parameters, for instance if the upper medium is isotropic, in which case the solution is very similar to standard SPPs. In general, the surface waves we consider can be excited using the usual techniques, such as exploiting a coupling prism in a Otto configuration [Maier, 2007; Zayats, Smolyaninov, and Maradudin, 2005], as shown below.

[4] This result has already been shown for particular interfaces, including left-handed media [Huang et al., 2007].

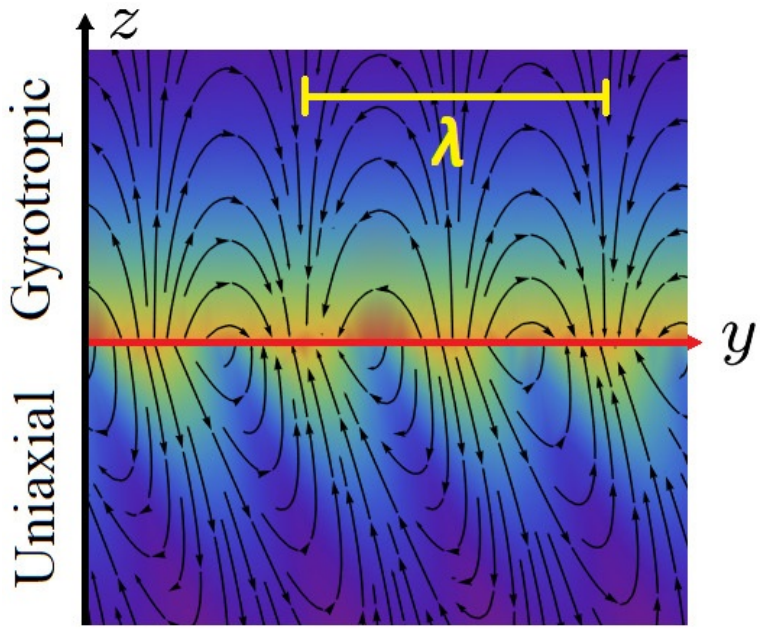

FIGURE 3.3: Electric field lines of the TM mode that propagates at the interface between a gyroelectric and a hyperbolic medium. The parameters used are $\epsilon_g = 3$, $g = 1$, $\epsilon_\perp = 9$, $\omega = 4 \times 10^{14}$ Hz and $\omega_p = 5 \times 10^{14}$ Hz (corresponding to $\epsilon_\parallel \approx -5.06$). The obtained in-plane wavelength is $\lambda = \frac{2\pi}{k_y} = 2.79\,\mu$m, which is shown in the figure as a comparison length. The penetration depths are $l_p^{\text{gyro}} = \frac{1}{\beta_1} \approx 1.8\,\mu$m and $l_p^{\text{uni}} = \frac{1}{\text{Re}\{\beta_2\}} \approx 0.4\,\mu$m, respectively.

3.2.2 InSb-Graphene AHMM interface at mid-infrared frequencies

It is not so easy to find a proper material which shows a gyroelectric behavior at reasonable temperatures and frequencies. The most famous examples of gyroelectric media are cold plasmas subjected to an external homogeneous magnetic field. However, when it comes to practical uses, plasmas are difficult to confine and it is not trivial to deal with their temperatures. On the other hand, some semiconductors have been proven to have a gyroelectric response at some particular frequencies when a magnetic bias is switched on. For example, Indium Antimonide (InSb) dielectric response can be modeled as [Moncada-Villa, Fernández-Domínguez, and Cuevas, 2019; Chochol et al., 2016]

$$\epsilon_g = \epsilon_0\,\epsilon_\infty \left(1 - \frac{\omega_p^2 \left(\omega^2 + i\gamma\omega\right)}{\left(\omega^2 + i\gamma\omega\right)^2 - \omega_{\text{cyc}}^2\omega^2} \right), \tag{3.24a}$$

$$g = \epsilon_0\,\epsilon_\infty \frac{i\omega_p^2\omega_{\text{cyc}}\omega}{\left(\omega^2 + i\gamma\omega\right)^2 - \omega_{\text{cyc}}^2\omega^2}, \tag{3.24b}$$

$$\omega_p = \sqrt{\frac{Ne^2}{\epsilon_0\epsilon_\infty m^*}}, \quad \omega_{\text{cyc}} = \frac{eB}{m^*}, \tag{3.24c}$$

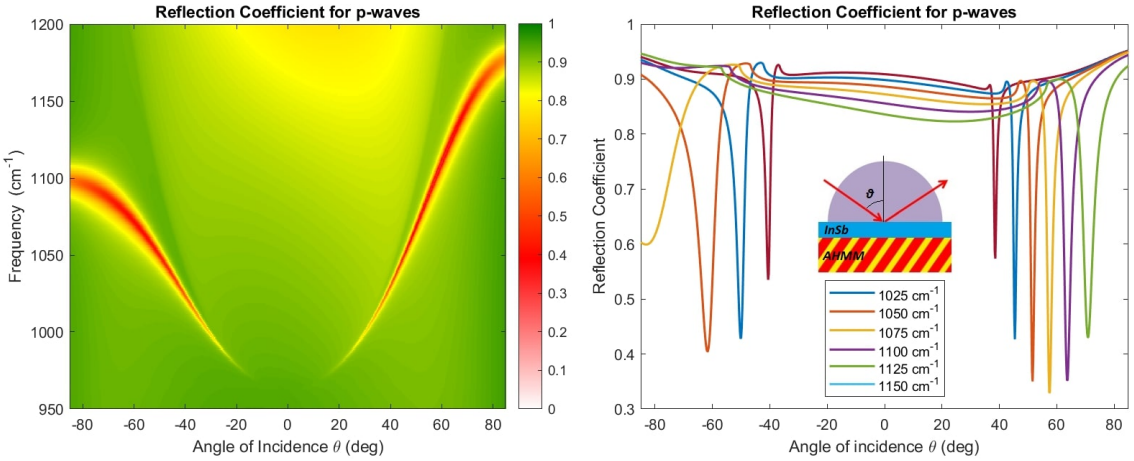

FIGURE 3.4: (a) Numerical results for the reflectivity of the Otto configuration with $d_{InSb} = 1.1\,\mu m$ and $\alpha = \frac{\pi}{4}$. (b) Reflectivity as a function of the incidence angle, for different values of the frequency.

where ω_p is the plasma frequency, ω_{cyc} is the cyclotron frequency, γ is the damping coefficient, N is the electron density, m^* is the effective mass and B is the external magnetic bias. In our case, one can properly choose both the electron density and the external magnetic field such that the existence conditions are satisfied.

As for the hyperbolic medium, many artificial structures have been shown to generate hyperbolic anisotropy. The most remarkable ones are a stack of alternating metallic and dielectric layers (Multilayer) and a lattice of metallic nanowires embedded in a dielectric background (Nanowire Array). Such engineered media are known as Hyperbolic Metamaterials (HMMs) [Ferrari et al., 2014; Shekhar, Atkinson, and Jacob, 2014]. Aiming for a multilayer structure, let us consider a material composed of a succession of metallic and dielectric layers, whose thicknesses and dielectric constants are, respectively, l_d, ϵ_d and l_m, ϵ_m. If the growth direction is $\hat{y}$, by means of an effective medium approximation it can be shown that the overall dielectric tensor of such composite material has the form Eq. (3.2), with

$$\epsilon_\perp = \frac{l_d\epsilon_d + l_m\epsilon_m}{l_d + l_m} = (1-f)\epsilon_d + f\epsilon_m, \tag{3.25}$$

$$\epsilon_\parallel = \frac{l_d + l_m}{l_d\epsilon_d^{-1} + l_m\epsilon_m^{-1}} = \frac{1}{(1-f)\epsilon_d^{-1} + f\epsilon_m^{-1}}, \tag{3.26}$$

where f is the *fill fraction* and it is defined as $f \equiv \frac{l_m}{l_m + l_d}$ [Ferrari et al., 2014; Shekhar, Atkinson, and Jacob, 2014]. If the growth direction does not lie on the interface plane, the HMM is referred to as *Asymmetric Hyperbolic Metamaterials* (AHMMs) and its physical configuration is depicted in Fig. 3.1.

Graphene layers stuck in a host matrix can exhibit a hyperbolic behavior [Iorsh et al., 2012]; their dielectric response can be modeled as

$$\epsilon_{\parallel} = \epsilon_h, \tag{3.27a}$$

$$\epsilon_{\perp} = \epsilon_h + i\,\frac{\sigma(\omega)}{d\omega\epsilon_0}, \tag{3.27b}$$

where ϵ_h is the dielectric constant of a host matrix, d is the distance between the two-dimensional graphene layers and $\sigma(\omega)$ is the surface conductivity [Nefedov et al., 2013; Dubinov et al., 2011]. If the optical axis is tilted with respect to the interface, we have a graphene-based AHMM [Nefedov et al., 2013; Nefedov and Melnikov, 2015]. One can properly choose the host matrix and the periodicity d to minimize the losses due to the imaginary part of $\epsilon_{\perp}$, as Nefedov and Melnikov showed in [Nefedov and Melnikov, 2015], and satisfy the existence conditions of the surface wave.

At this point, a brief clarification is necessary: the dielectric functions described by equations Eqs. (3.24a) to (3.24c) and Eqs. (3.27a) and (3.27b) do not satisfy the working assumptions used earlier. In fact, they are affected by losses, which means that the system belongs to the white subset in Fig. 2.4, i.e., it does not respect any of the three fundamental symmetries described in Chapter 2. When studying a configuration that is experimentally realizable, it is almost impossible to eliminate losses in a heterogeneous system. However, this does not undermine our analysis, as our goal is to highlight the non-reciprocal effects in such a system, which are present regardless of whether losses are included or not.

In order to show how the ESW here predicted could be observed in such a system, we have studied the reflection properties of an InSb-Graphene AHMM interface in the Otto configuration, where Thallium Bromo-Iodide (KRS5) was used as the coupling medium. Figure 3.4(a) shows the reflectivity of the system as a function of the light frequency and the incidence angle θ, calculated using the 4×4 Transfer Matrix Formalism for anisotropic media, proposed by Berreman [Berreman, 1972]. For each value of the frequency, we notice that the reflectivity significantly drops near a certain value of the incidence angle θ. For that particular value of θ, the in-plane component of the wave vector gives rise to the coupling between bulk and surface modes. In addition, here we can easily observe the non-reciprocal behavior of these ESWs, as the spectra shown in Fig. 3.4 are not symmetric with respect to $\theta = 0$. Six different sections of the reflectivity plot are shown in Fig. 3.4(b), where the effects of the excitation of the ESW can be observed more clearly. As an example to quantify the effect of losses (here essentially due to those in the gyroelectric medium), the propagation length of the forward propagating mode at $\omega = 1100\,\mathrm{cm}^{-1}$, defined as $l_p \equiv 1/\,\mathrm{Im}\{k_y\}$, amounts to $l_p \approx 40\lambda$. We can conclude that InSb and a graphene-based AHMM could be exploited to excite and detect the novel modes here predicted.

In the upcoming part of this chapter, we will explore what happens when the

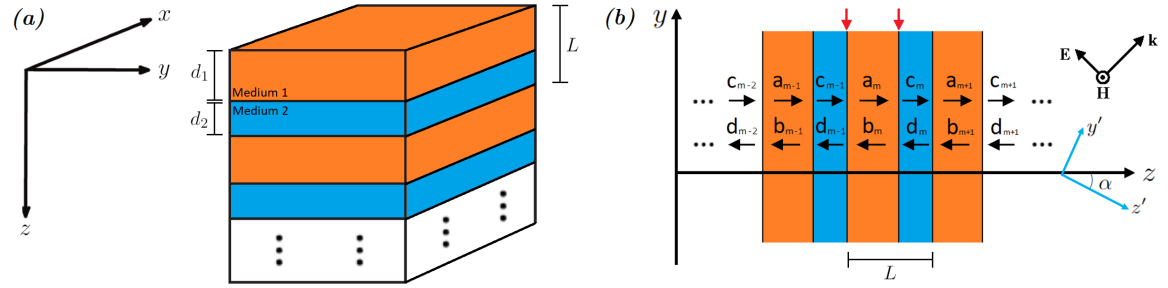

FIGURE 3.5: (a) Outline of the 1D-periodic multilayer structure. (b) Outline of the yz plane section of the periodic structure under consideration. Here, y' and z' represent the principal axes of the hyperbolic slabs.

structure analyzed so far becomes patterned with multiple layers, thus forming a photonic crystal.

3.3 Gyro-Hyperbolic Photonic Crystals

3.3.1 Anisotropic multilayered structures

Consider a multilayered system consisting of an ordered succession of two slabs of lossless material, whose thicknesses and dielectric tensors are, respectively, $d_1, \boldsymbol{\epsilon}_1$ and $d_2, \boldsymbol{\epsilon}_2$, as depicted in Fig. 3.5(a). Let the spatial periodicity of the stratified medium be $L = d_1 + d_2$ and $\hat{z}$ be the growth direction, such that the overall dielectric function on the structure can be written as follows

$$\boldsymbol{\epsilon} = \begin{cases} \boldsymbol{\epsilon}_1 & mL < z < mL + d_1, \\ \boldsymbol{\epsilon}_2 & mL + d_1 < z < (m+1)L, \end{cases}$$

where m is an integer number. We consider a multilayered structure composed of gyroelectric and uniaxial layers, such that their dielectric tensors read

$$\boldsymbol{\epsilon}_1 = \epsilon_0 \begin{pmatrix} \epsilon_g & 0 & 0 \\ 0 & \epsilon_g & ig \\ 0 & -ig & \epsilon_g \end{pmatrix}, \quad \boldsymbol{\epsilon}_2' = \epsilon_0 \begin{pmatrix} \epsilon_\perp & 0 & 0 \\ 0 & \epsilon_\parallel & 0 \\ 0 & 0 & \epsilon_\perp \end{pmatrix}, \tag{3.28}$$

in their respective principal coordinate systems. As for the uniaxial medium, let us initially consider the general configuration wherein its optical axis is neither parallel nor perpendicular to the interface between the two media. Hence, we have to rotate its dielectric tensor by means of a rotation matrix such that, in our coordinate system,

the uniaxial dielectric tensor reads

$$\boldsymbol{\epsilon}_2 = \boldsymbol{R}_x(\alpha)\,\boldsymbol{\epsilon}'_u\,\boldsymbol{R}_x(-\alpha) = \epsilon_0 \begin{pmatrix} \epsilon_{xx} & 0 & 0 \\ 0 & \epsilon_{yy} & \epsilon_{yz} \\ 0 & \epsilon_{zy} & \epsilon_{zz} \end{pmatrix},$$

where the matrix elements are

$$\begin{aligned} \epsilon_{xx} &= \epsilon_\perp, \\ \epsilon_{yy} &= \epsilon_\perp \sin^2\alpha + \epsilon_\parallel \cos^2\alpha, \\ \epsilon_{yz} &= \epsilon_{zy} = \left(\epsilon_\perp - \epsilon_\parallel\right) \sin\alpha \cos\alpha, \\ \epsilon_{zz} &= \epsilon_\perp \cos^2\alpha + \epsilon_\parallel \sin^2\alpha. \end{aligned}$$

For analytical convenience, we focus on anisotropic configurations where TE and TM modes can be decoupled, while low-symmetry configurations will be numerically investigated in Section 3.3.4. Non-trivial results will concern only the TM polarization; thus, it is appropriate to consider the following form for the magnetic field, which accounts for bulk mode propagation both in the $\hat{z}$ and $-\hat{z}$ directions:

$$H_x^m(y,z) = \begin{cases} \left[a_m\, e^{ik_u(z-mL)} + b_m\, e^{-ik_u(z-mL)}\right] e^{i(k_y y - \omega t)} & mL < z < mL + d_u, \\ \left[c_m\, e^{ik_g(z-mL)} + d_m\, e^{-ik_g(z-mL)}\right] e^{i(k_y y - \omega t)} & mL + d_u < z < (m+1)L, \end{cases} \tag{3.29}$$

where u stands for *uniaxial* and g for *gyrotropic*, k_u and k_g represent the z-components of the wave vectors, whereas $L \equiv d_u + d_g$, d_u and d_g are, respectively, the period of the structure and the thicknesses of the two slabs. The coefficients a_m, b_m, c_m, d_m are the amplitudes of forward and backward modes relative to each medium, as outlined in Fig. 3.5(b).

Applying the continuity conditions for H_x and E_y on the two boundaries marked by red arrows in Fig. 3.5(b), leads to a four-equations system relating the six variables a_m, b_m, c_m, d_m, c_{m-1} and d_{m-1}. As shown in Appendix B, the whole algebraic system can be recast in order to express c_{m-1} and d_{m-1} as functions of c_m and d_m:

$$\begin{pmatrix} c_{m-1} \\ d_{m-1} \end{pmatrix} = \begin{pmatrix} A & B \\ C & D \end{pmatrix} \begin{pmatrix} c_m \\ d_m \end{pmatrix}. \tag{3.30}$$

where A, B, C and D are complex coefficients which will be derived in the next section. We will use this formalism in order to find the eigenmodes in a one-dimensional periodic structure.

3.3.2 Periodic anisotropic structures

If we let the number of layers become infinite, what we obtain is a Photonic Crystal. In such a periodic system, the Bloch theorem assures that the solution to the

Helmholtz equation is a Bloch wave, namely a wave function which can be written as the product of a plane wave and a periodic term

$$\mathbf{H}(z) = \mathbf{H}_B(z)\, e^{iK_B z}, \tag{3.31}$$

where $\mathbf{H}_B(z) = \mathbf{H}_B(z+L)$ denotes a periodic function, and K_B represents the Bloch wave number, lying within the first Brillouin zone $[-\pi/L, \pi/L]$ [Yariv and Yeh, 2002]. Following the procedure shown in [Yeh, 2005], we must solve the following eigenvalue problem

$$\begin{pmatrix} A & B \\ C & D \end{pmatrix} \begin{pmatrix} c_m \\ d_m \end{pmatrix} = e^{-iK_B L} \begin{pmatrix} c_m \\ d_m \end{pmatrix}, \tag{3.32}$$

whose solutions are

$$\begin{pmatrix} c_m \\ d_m \end{pmatrix} = \begin{pmatrix} B \\ e^{-iK_B L} - A \end{pmatrix}, \tag{3.33}$$

where

$$K_B = \pm \frac{1}{L} \cos^{-1}\left(\frac{A+D}{2}\right). \tag{3.34}$$

As pointed out in Appendix B, the eigenvalues are one the reciprocal of the other because the matrix in Eq. (3.32) is unitary. If K_B is a real number, the eigenvalues represent propagating waves, whereas complex values of K_B correspond to damped waves in the bulk. Due to the properties of the cosine function, we can distinguish two scenarios: if $A + D \in \mathbb{R}$ and $A + D < 2$, the Bloch wave can propagate through the PhC, otherwise it will decay inside the bulk [Yeh, 2005; Yariv and Yeh, 2002]. The latter situation corresponds to the band gap.

We can derive the coefficients A, B, C, D in the TM case by means of Eqs. (B.1) to (B.4). By defining

$$\epsilon_v \equiv \frac{\epsilon_g^2 - g^2}{\epsilon_g}$$

and

$$Z \equiv \frac{\epsilon_{yz}\epsilon_v}{\epsilon_\parallel \epsilon_\perp} - i\frac{g}{\epsilon_g}, \tag{3.35}$$

they turn out to be

$$A_{TM} = e^{ik_u d_u}\left\{\cos k_g d_g + \frac{i}{2}\sin k_g d_g \left[\frac{\epsilon_\parallel \epsilon_\perp k_g}{\epsilon_v \epsilon_{zz} k_u} + \frac{\epsilon_v \epsilon_{zz} k_u}{\epsilon_\parallel \epsilon_\perp k_g} - \frac{\epsilon_\parallel \epsilon_\perp}{\epsilon_v \epsilon_{zz}} \frac{k_y^2}{k_u k_g} Z^2\right]\right\}, \tag{3.36a}$$

$$B_{TM} = \frac{i}{2} e^{-ik_u d_u} \sin k_g d_g \left\{\frac{\epsilon_\parallel \epsilon_\perp k_g}{\epsilon_v \epsilon_{zz} k_u} - \frac{\epsilon_v \epsilon_{zz} k_u}{\epsilon_\parallel \epsilon_\perp k_g} - \frac{\epsilon_\parallel \epsilon_\perp}{\epsilon_v \epsilon_{zz}} \frac{k_y^2}{k_u k_g} Z^2 + 2Z\frac{k_y}{k_g}\right\}, \tag{3.36b}$$

$$C_{TM} = -\frac{i}{2} e^{ik_u d_u} \sin k_g d_g \left\{ \frac{\epsilon_\parallel \epsilon_\perp k_g}{\epsilon_v \epsilon_{zz} k_u} - \frac{\epsilon_v \epsilon_{zz} k_u}{\epsilon_\parallel \epsilon_\perp k_g} - \frac{\epsilon_\parallel \epsilon_\perp}{\epsilon_v \epsilon_{zz}} \frac{k_y^2}{k_u k_g} Z^2 - 2Z \frac{k_y}{k_g} \right\}, \tag{3.36c}$$

$$D_{TM} = e^{-ik_u d_u} \left\{ \cos k_g d_g - \frac{i}{2} \sin k_g d_g \left[\frac{\epsilon_\parallel \epsilon_\perp k_g}{\epsilon_v \epsilon_{zz} k_u} + \frac{\epsilon_v \epsilon_{zz} k_u}{\epsilon_\parallel \epsilon_\perp k_g} - \frac{\epsilon_\parallel \epsilon_\perp}{\epsilon_v \epsilon_{zz}} \frac{k_y^2}{k_u k_g} Z^2 \right] \right\}. \tag{3.36d}$$

Notice that Z reduces to zero if both media are isotropic and, consequently, the matrix elements in Eqs. (3.36a) to (3.36d) reduce to the expressions commonly documented in the literature [Joannopoulos et al., 2008; Yeh, 2005; Yariv and Yeh, 2002]. Furthermore, Eq. (3.34) becomes

$$K_{TM}^B = \frac{1}{L} \cos^{-1} \left(\cos k_g d_g \cos k_u d_u - \mathcal{W} \sin k_g d_g \sin k_u d_u \right), \tag{3.37}$$

where we defined

$$2\mathcal{W} \equiv \frac{\epsilon_\parallel \epsilon_\perp k_g}{\epsilon_v \epsilon_{zz} k_u} + \frac{\epsilon_v \epsilon_{zz} k_u}{\epsilon_\parallel \epsilon_\perp k_g} - \frac{\epsilon_\parallel \epsilon_\perp}{\epsilon_v \epsilon_{zz}} \frac{k_y^2}{k_u k_g} Z^2. \tag{3.38}$$

As mentioned in the previous section, we only focus on the TM polarization because TE modes obey the very same equations of the isotropic case.

Before we move on, it is essential to make a significant observation. As evident in Eqs. (3.37) and (3.38), the presence of Z ensures that K_B has an imaginary part if $g \neq 0$ and $\epsilon_{yz} \neq 0$ simultaneously, for any real values of ω and k_y. This is surprising, especially considering that it holds even for lossless structures such as the ones we aim to analyze. In any case, the band diagram is almost empty because, apart from normal incidence and a few other cases, no mode can propagate into the bulk. This last statement will be examined in more detail during the discussion of the numerical results. We aim to investigate non-trivial scenarios involving gyrotropy, hence we are compelled to restrict our analysis to the case $\alpha = k\pi/2$, where $k \in \mathbb{Z}$.

In the upcoming section, we will employ Eq. (3.37) to derive band diagrams for TM modes within our anisotropic PhC. Our objective is to identify surface states within the band gaps, where bulk modes are not allowed to propagate.

3.3.3 Modes in a semi-infinite photonic crystal

Valuable insights can be gathered by exploring the surface modes permitted to propagate in PhCs [Bashiri et al., 2019; Vinogradov et al., 2010], as we will demonstrate below.

When a PhC is cut along one interface between two consecutive slabs, two semi-infinite PhCs are created. The dispersion relation for surface waves propagating on a semi-infinite PhC bordering a dielectric half-space is [Wang et al., 2009; Feng et al., 2005]

$$e^{iK_B L} - A - \frac{Bc}{\omega\epsilon_I}\sqrt{\epsilon_I\left(\frac{\omega}{c}\right)^2 - k_y^2} = 0, \tag{3.39}$$

where ϵ_I is the dielectric constant of the isotropic dielectric half-space. Equation (3.39) enables us to identify and graphically represent the surface modes directly on the reduced band diagrams that characterize the system.

Before we present our numerical findings, it is important to introduce the frequency dependence of the dielectric functions. We choose to consider the following dispersion for the uniaxial medium permittivities[5]

$$\epsilon_{\perp,\parallel} = \epsilon_\infty\left(1 - \frac{\omega_{p_{\perp,\parallel}}^2}{\omega^2}\right). \tag{3.40}$$

Such response functions with anisotropic plasma frequencies characterize the behavior of media that exist in nature [Brar et al., 2014; Grecu, 1973] or can be artificially engineered using multilayer or nanowire array geometries [Yermakov et al., 2015; Koshelev and Bogdanov, 2015; Belov et al., 2003]. In such engineered media, non-local effects may play a significant role in shaping the dispersion of EWs, as discussed in [Chebykin et al., 2011; Gorlach and Belov, 2014]. We neglect such effects in the current analysis.

As ω varies, Eq. (3.40) may describe an anisotropic metal ($\omega < \min[\omega_{p_\perp}, \omega_{p_\parallel}]$), an anisotropic dielectric ($\omega > \max[\omega_{p_\perp}, \omega_{p_\parallel}]$) or a hyperbolic medium ($\min[\omega_{p_\perp}, \omega_{p_\parallel}] < \omega < \max[\omega_{p_\perp}, \omega_{p_\parallel}]$). The last regime is of particular interest when it comes to surface modes, as shown in Fig. 3.6. Its rows correspond to the three different scenarios $\omega_{p,\parallel} = \omega_{p,\perp}$, $\omega_{p,\parallel} < \omega_{p,\perp}$ and $\omega_{p,\parallel} > \omega_{p,\perp}$, respectively. Instead, columns correspond to non-gyrotropy (left) and gyroelectric (right) cases. It should be specified that the surface modes in Fig. 3.6 only concern the configuration where the semi-infinite crystal terminates with a gyrotropic slab. If this were not the case, the dispersion of the surface waves would be slightly different, but all their characteristic features would remain the same.

- Figure 3.6(a)-(b), $\omega_{p,\parallel} = \omega_{p,\perp} \equiv \omega_p$. Two distinct types of surface waves are observed: a truncated SPP below the threshold $\omega = \omega_p$, and Tamm waves in the domain $\omega > \omega_p$, where the metallic constituents demonstrate dielectric behavior ($\epsilon_\parallel, \epsilon_\perp > 0$). When gyrotropy is switched on within the dielectric layers, the lower bands get modified such that the SPP no longer exists. Conversely,

[5]The quantities $\epsilon_\parallel$ and $\epsilon_\perp$ were initially defined in Section 3.2.2, in a form that differs from the one given in Eq. (3.40). From this point onward and throughout the remainder of the chapter, we adopt the functional form defined in Eq. (3.40).

Tamm waves experience subtle modifications but do not undergo significant alterations.

- Figure 3.6(c)-(d), $\omega_{p,\parallel} < \omega_{p,\perp}$. The horizontal bulk plasmon line undergoes a significant division into numerous bulk bands, situated within the range delineated by the plasma frequencies $\omega_{p,\parallel}$ and $\omega_{p,\perp}$, where the anisotropic metallic components behave as Type 2 HMMs [Ferrari et al., 2014; Shekhar, Atkinson, and Jacob, 2014]. Notably, an intermediate surface mode emerges within each band gap separating the bulk bands. These waves have a positive group velocity, thus they propagate in the forward direction. Interestingly, the introduction of gyrotropy has minimal impact on surface modes, despite the fact that some degenerate bands undergo division. For enhanced clarity, Fig. 3.7(a) illustrates two transversal sections of the reduced band diagram.

- Figure 3.6(e)-(f), $\omega_{p,\parallel} > \omega_{p,\perp}$. Similar to the previous scenario, an infinite array of bulk bands occupies the domain delineated by the plasma frequencies $\omega_{p,\perp}$ and $\omega_{p,\parallel}$. Within this domain, the anisotropic metallic components behave as Type 1 HMMs [Ferrari et al., 2014; Shekhar, Atkinson, and Jacob, 2014]. Notably, all intermediate surface waves demonstrate a negative group velocity, implying their propagation in the backward direction. Furthermore, the SPP undergoes a bifurcation into two branches due to the convergence of lower bands. When gyrotropy is switched on, the lower bands get modified such that the SPP no longer exists. For enhanced clarity, Fig. 3.7(b) illustrates two transversal sections of the reduced band diagrams, whereas Fig. 3.7(c)-(f) show four isofrequency contours in the gyrotropic case.

In summary, these intermediate waves[6] can propagate either forward or backward, depending on the hyperbolic behavior of the uniaxial material constituting the structure. Similar results were found in [Golenitskii, Koshelev, and Bogdanov, 2016] for the non-gyrotropic case. In such work, intermediate surface modes are referred to as *Tamm-Langmuir surface waves*.

As stated above, the presence of gyrotropy in the system modifies some bulk bands, as can be clearly seen in Fig. 3.7. This implies that by adjusting the external magnetic field, the electromagnetic response of the system can be fine-tuned, allowing for the modification of the permissible frequency ranges within the structure.

Figure 3.8 presents a comparison of the field distributions between the Tamm wave and the intermediate mode. In particular, the latter exhibits a significantly greater penetration depth than the former. Hence, in finite multilayer structures, this property may allow the control of signal transmission through surface modes rather than bulk modes. It is observed that the electric field of the novel modes concentrates and oscillates within the uniaxial metallic layers. This unique feature facilitates a deeper penetration of the mode into the bulk. This behavior is common in periodic

[6]The word *intermediate* refers to the position of the new surface modes, which live in the frequency domain delimited by the two plasma frequencies.

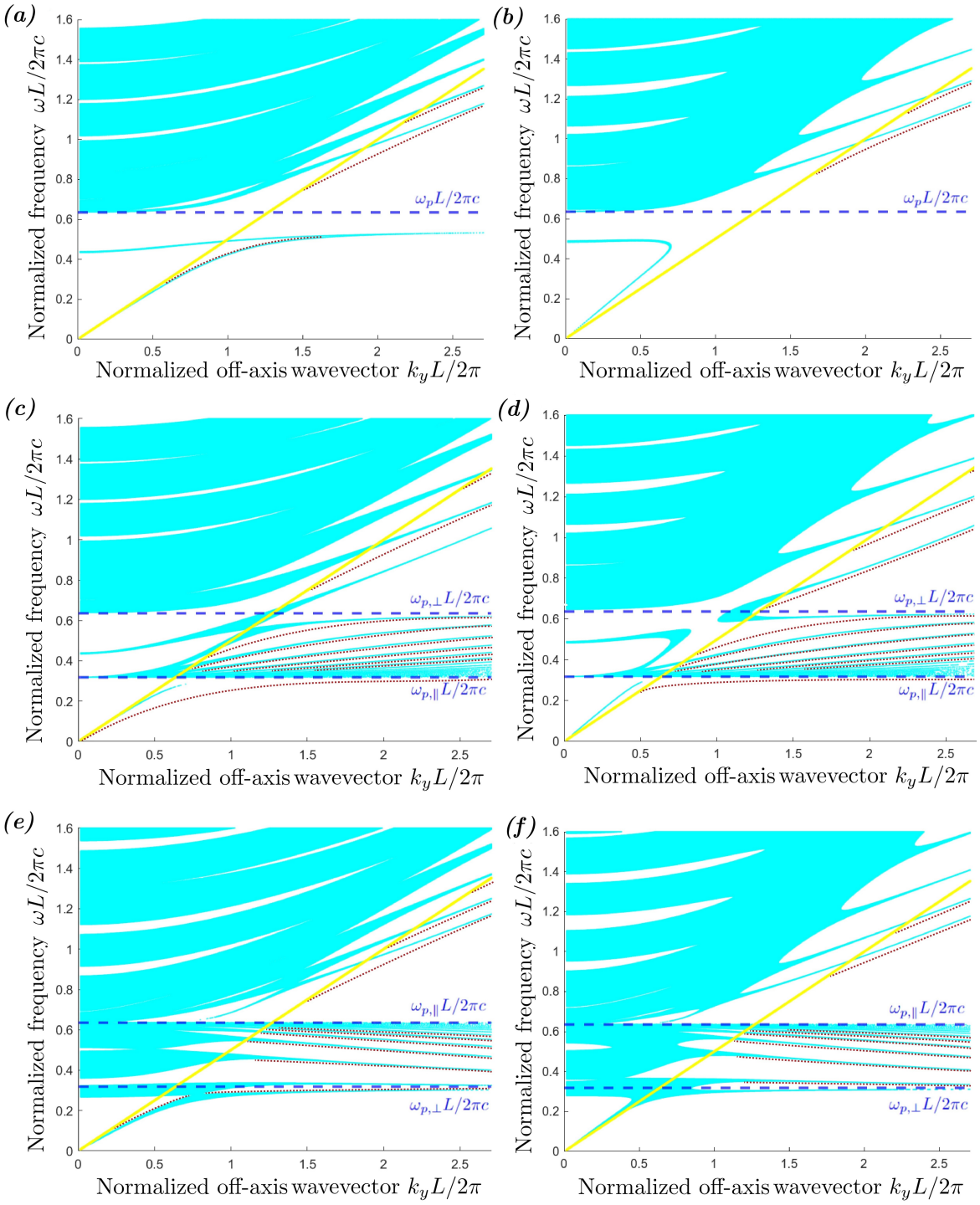

FIGURE 3.6: Reduced band diagrams for TM waves in a metal-dielectric PhC, for different values of the structural parameters. The red dotted lines correspond to surface modes, whereas the yellow straight line represents the light line of the dielectric half-space. The considered structural parameters are $\epsilon_I = 4$, $\epsilon_g = 3$, $\epsilon_\infty = 8$, $d_g = 0.56\,\mu$m, $d_u = 0.44\,\mu$m and $\alpha = \pi/2$. (a) $\omega_{p,\parallel} = \omega_{p,\perp}$, $g = 0$, (b) $\omega_{p,\parallel} = \omega_{p,\perp}$, $g = 1.5$, (c) $\omega_{p,\parallel} < \omega_{p,\perp}$, $g = 0$, (d) $\omega_{p,\parallel} < \omega_{p,\perp}$, $g = 1.5$, (e) $\omega_{p,\parallel} > \omega_{p,\perp}$, $g = 0$, (f) $\omega_{p,\parallel} > \omega_{p,\perp}$, $g = 1.5$.

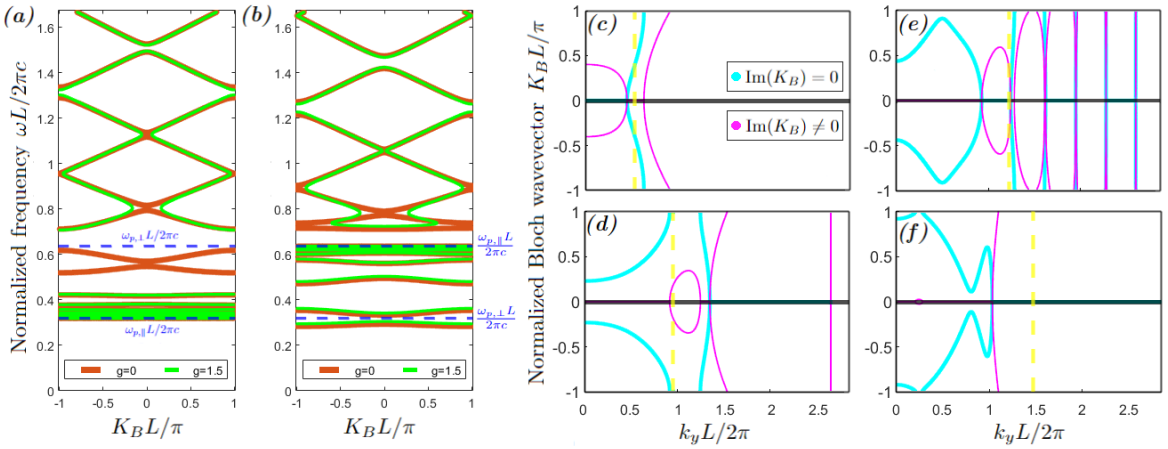

FIGURE 3.7: (a)-(b) are transversal sections of the reduced band diagram shown in Fig. 3.6, for $k_y L/2\pi = 1$. Panel (a) corresponds to Fig. 3.6(c)-(d), whereas panel (b) corresponds to Fig. 3.6(e)-(f). As gyrotropy is switched on, a large number of bulk bands appear slightly above or below the $\omega_{p,\parallel} L/2\pi c$ line. (c)-(f) are isofrequency contours corresponding to four slices of Fig. 3.6(f) at $\omega L/2\pi c = 0.27,\ 0.48,\ 0.61,\ 0.74$. Thick cyan curves represent bulk bands, whereas thin magenta ones correspond to complex values of the Bloch wave vector. Yellow dashed lines represents light lines.

metal-dielectric layered structures with anisotropic metal layers [Bogdanov and Suris, 2012], and does not depend on the presence of a gyrotropic medium.

We conclude this section by numerically investigating the observation made at the end of Section 3.3.2, concerning the restriction to $\alpha = k\pi/2$, where $k \in \mathbb{Z}$. As pointed out before, if $\alpha \neq k\pi/2$ then the Bloch wave number is complex for almost every non-zero value of k_y. As a further confirmation, Fig. 3.9 shows the behavior of the imaginary part of K_B as k_y varies, for four different values of the working frequency. It is evident that $K_B \in \mathbb{C}$ almost everywhere. Notice that, depending on the working frequency, the imaginary part of K_B may be huge or approach zero at normal incidence. The first case corresponds to the band gap, where $A + D$ is now real but larger than 2. The second case corresponds to bulk propagating modes, hence this demonstrates that the band diagram is not empty at normal incidence. Moreover, apart from the case $k_y \to 0$, there may exist additional values of k_y for which $\mathrm{Im}\{K_B\}$ becomes very small. This is due to the form of Eq. (3.38): k_u and k_g are imaginary for high values of the off-axis wave vector, hence the imaginary part of the coefficient $\mathcal{W}$ can actually become zero for a limited set of values of k_y.

3.3.4 Finite multilayer structures

This final section contains a few numerical results concerning finite structures, whose properties were analyzed using the so-called *Otto configuration* with a coupling prism whose refractive index is 3. As for the numerical method, we used the 4×4

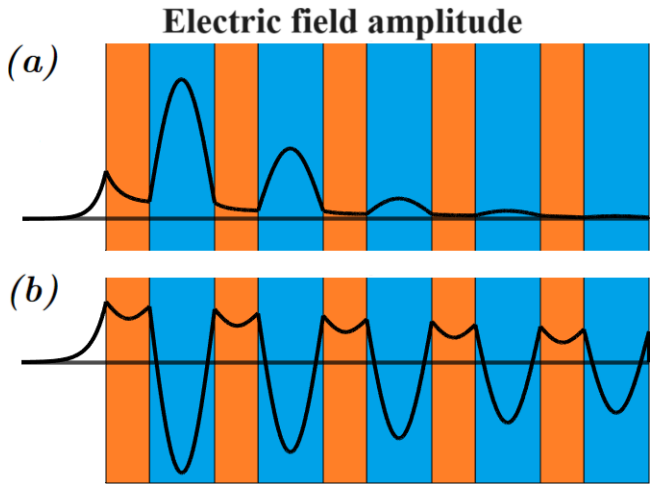

FIGURE 3.8: Typical space distributions of the y-component of the electric field amplitude in a semi-infinite gyro-uniaxial PhC. The blue regions represent the uniaxial components, whereas the orange ones represent the gyrotropic components. (a) Tamm wave. (b) Intermediate surface mode.

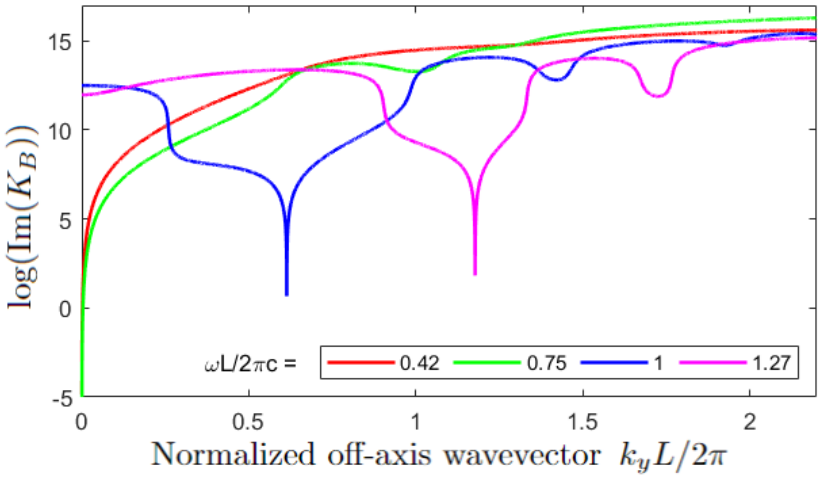

FIGURE 3.9: Natural logarithm of the imaginary part of the Bloch wave number as a function of the off-axis wave vector, for four different values of the working frequency. The structural parameters are the same as in Fig. 3.6(d), except for $\alpha = 1$ rad.

Transfer Matrix Formalism for anisotropic media, proposed by Berreman [Berreman, 1972].

First, we conducted a brief analysis on the Goos-Hänchen Shift (GHS) [Manzoor et al., 2022] for finite multilayer structures. As mentioned in Chapter 1, it is a well-known fact that the GHS increases dramatically when it gets close to the Brewster angle [Lai and Chan, 2002], at which light is totally transmitted through the system. We calculated both the reflectivity and GHS for two structures consisting of ten periods each, in the frequency domain delimited by the two plasma frequencies $\omega_{p,\perp}$ and $\omega_{p,\parallel}$. The results are shown in Fig. 3.10. Consistent with expectations, at angles where the reflectivity approaches zero, the GHS is positive in the case of forward

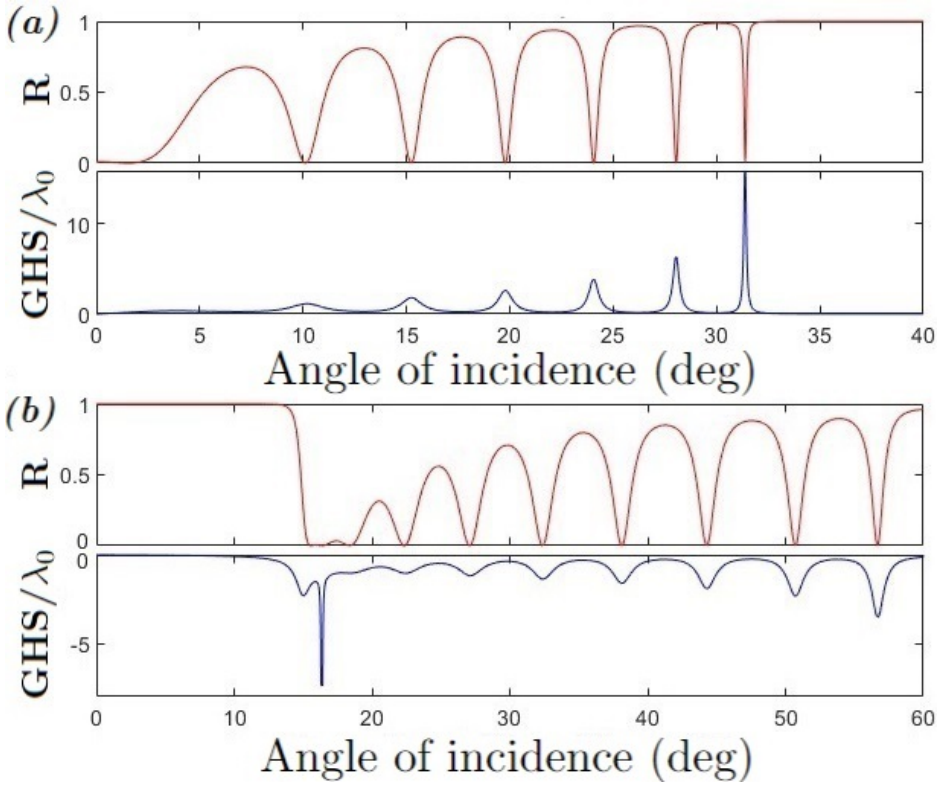

FIGURE 3.10: Reflectivity and Goos–Hänchen Shift (in units of the incident wavelength) for two multilayer structures composed of 10 periods, calculated using the Transfer Matrix method. The structural parameters are the same as in Fig. 3.6. (a) $\omega_{p,\parallel} < \omega_{p,\perp}$, corresponding to forward surface modes of Fig. 3.6(d). (b) $\omega_{p,\parallel} > \omega_{p,\perp}$, corresponding to backward propagating surface modes of Fig. 3.6(f).

modes, whereas it is negative for backward modes.

A final consideration worth making concerns the bulk bands. As can be seen from Eqs. (3.37) and (3.38), the dispersion of the bulk bands depends only on k_y^2, and thus there is no distinction between positive and negative angles of incidence. Indeed, the bulk modes are unaffected by non-reciprocity effects, despite the presence of a gyrotropic medium.[7] To break this high degree of symmetry and observe differences between positive and negative angles of incidence, one possible approach is to rotate the gyroelectric components so that, in our coordinate system, their dielectric tensor takes the form:

$$\boldsymbol{\epsilon}_1 = \epsilon_0 \begin{pmatrix} \epsilon_g & 0 & ig \\ 0 & \epsilon_g & 0 \\ -ig & 0 & \epsilon_g \end{pmatrix}. \tag{3.41}$$

[7] It should be noted that this does not necessarily apply to surface modes. In fact, in this case it does not: we have already shown in Section 3.2 that a tensor like the one in Eq. (3.28) can introduce asymmetry in the propagation of surface modes. However, the same tensor is not capable of producing the same effect for bulk modes when the system becomes periodic.

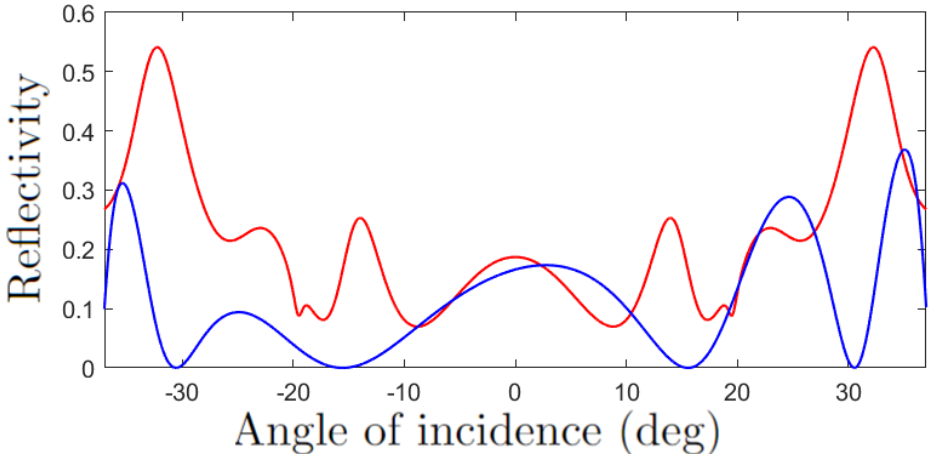

FIGURE 3.11: Comparison between the reflectivity of gyro-uniaxial multilayer structures whose gyrotropic components are described by Eq. (3.28) (red symmetric curve) and Eq. (3.41) (blue asymmetric curve).

Figure 3.11 shows a comparison between the reflectivity of two multilayer structures whose gyrotropic tensors are described by Eq. (3.28) and Eq. (3.41). It appears evident that the latter configuration introduces an asymmetry between the positive and negative angles of incidence. Such configuration cannot be analyzed using the method of Section 3.3.2 because TE and TM modes cannot be decoupled. They should be studied at the same time.

3.4 Conclusions

In this combined study, we investigated novel electromagnetic surface waves (ESWs) arising at the interface between hyperbolic media and gyroelectric materials, as well as within one-dimensional photonic crystals (PhCs) composed of gyroelectric and uniaxial layers. Through a combination of theoretical analysis and electromagnetic simulations, we demonstrated that the interplay between anisotropy and gyrotropy enables the existence of unique surface modes with distinctive properties.

At the simple interface level, we showed that gyrotropy induces non-reciprocal multiplicity in TM-polarized surface modes, while the hyperbolic dispersion of the anisotropic medium leads to tilted field lines reminiscent of Zenneck waves. Frequency dispersion was accounted for, and a practical system—featuring doped InSb under an external magnetic field and a graphene-based AHMM—was proposed to support and potentially detect these surface waves, particularly in an Otto configuration.

Extending the analysis to periodic structures, we characterized the dispersion of bulk bands and surface states in PhCs, uncovering not only traditional SPPs and Tamm waves but also a new class of ESWs with either positive or negative group velocity. These surface waves exhibit significantly larger penetration depths into the bulk compared to conventional modes, offering enhanced control over

signal transmission through surface-guided phenomena. Gyrotropy was found to deform photonic bands and enable tunable electromagnetic responses through external magnetic fields, enhancing the functionality of these structures as frequency-selective devices.

Reflectivity spectra analysis in finite PhC structures revealed near-zero reflectivity correlated with large, tunable Goos-Hänchen shifts, further emphasizing the directional control enabled by gyrotropy. Additionally, asymmetrical reflectivity with respect to incidence angle inversion confirmed the non-reciprocal nature of these surface modes.

Overall, the findings of this chapter give a deeper understanding of surface modes arising from the interplay between gyrotropic and hyperbolic materials. These insights may support the future development of photonic devices with potential applications in non-reciprocal optics, directional light manipulation, and tunable photonic systems.

Chapter 4

Electromagnetic Description of Graviton-Polaritons

This chapter develops an electromagnetic description of graviton–polaritons emerging in a two-dimensional electron gas (2DEG) in the fractional quantum Hall (FQH) regime. Starting from a microscopic picture of chiral spin-2 collective modes ("gravitons") in Laughlin-like states, we construct a quadrupolar light–matter coupling and derive an effective, nonlocal susceptibility tensor for the 2DEG that displays a gyrotropy-like in-plane structure and explicit spatial dispersion. This tensor is then used to obtain the dispersion and field profiles of the electromagnetic surface modes supported by a single FQH layer and by a coupled 2DEG–metal bilayer, revealing hybrid magnetoplasmon–polaritons with strongly confined, plasmonic-like character. Building on these results, the chapter proposes several cavity-electrodynamics configurations—based on planar electrodes and plasmonic nanoparticles—that interface the chiral quadrupole response of the FQH graviton with localized electromagnetic modes. Perturbative estimates of the resulting cavity frequency shifts identify realistic parameter regimes where graviton–polaritons could be detected experimentally, and illustrate in an explicit way how a fully quantum mechanical model can be translated into macroscopic response functions suitable for the surface-wave framework developed in Chapter 3.

4.1 Introduction

In this chapter we extend the surface–wave and response–function framework developed in the previous chapters to a strongly correlated quantum system, namely a two-dimensional electron gas (2DEG) in the fractional quantum Hall (FQH) regime. The chapter is organized as follows. First, we introduce the basic physical ingredients of the FQH effect and the emergence of chiral spin-2 collective excitations, known as graviton modes, which provide the microscopic origin of the light–matter coupling considered here. We then develop a quadrupolar–optical description and derive an effective, nonlocal electromagnetic susceptibility for the 2DEG. This response function is subsequently employed to determine the electromagnetic surface eigenmodes of the system and to analyze their hybridization with cavity fields in

several resonator configurations, with the aim of identifying those that are most suitable for the experimental observation of these effects.

The remaining part of this introductory section is therefore devoted to a concise overview of the fractional quantum Hall effect and of the microscopic theory underlying graviton–polaritons, which will serve as the foundation for the macroscopic electromagnetic description developed in the rest of the chapter.

4.1.1 Fractional quantum Hall effect in 2DEGs

The fractional quantum Hall (FQH) effect is a paradigmatic example of an emergent, strongly correlated quantum fluid realized in a two-dimensional electron gas (2DEG) subjected to a strong perpendicular magnetic field and cooled to ultralow temperatures. Experimentally, it was first observed by Tsui, Stormer and Gossard in ultra–high-mobility GaAs/AlGaAs heterostructures as quantized plateaus in the Hall resistance at fractional values of the filling factor, accompanied by vanishing longitudinal resistance [Tsui, Stormer, and Gossard, 1982]. A detailed account of the discovery and its implications is given in Stormer's Nobel lecture [Stormer, 1999].

In the presence of a uniform perpendicular magnetic field $\mathbf{B}$, the single-particle spectrum of a 2DEG consists of highly degenerate Landau levels,

$$E_N = \hbar\omega_{\mathrm{cyc}}\left(N + \frac{1}{2}\right), \qquad \omega_{\mathrm{cyc}} = \frac{eB}{m^*}, \qquad n = 0, 1, 2, \ldots, \tag{4.1}$$

where m^* is the effective electron mass and $e > 0$ is the elementary charge. The associated magnetic length,

$$\ell_B = \sqrt{\frac{\hbar}{eB}}, \tag{4.2}$$

sets the fundamental length scale for the cyclotron orbits and the spatial structure of electronic wave functions. For a 2D carrier density n, the Landau level filling factor is

$$\nu = 2\pi\ell_B^2 n = \frac{nh}{eB}, \tag{4.3}$$

which counts the number of filled Landau levels in the noninteracting picture. In the integer quantum Hall effect (IQH), plateaus in the Hall conductance σ_{xy} occur at integer ν, $\sigma_{xy} = \nu\, e^2/h$, and can be understood largely in terms of single-particle physics in a disordered potential.

By contrast, the FQH effect occurs at fractional filling factors $\nu = p/q$ (with q typically odd), where the kinetic energy is quenched within a partially filled Landau level and the physics is dominated by Coulomb interactions. The hallmark of the FQH regime is the emergence of new incompressible quantum fluids with fractionally quantized Hall conductance,

$$\sigma_{xy} = \nu\frac{e^2}{h}, \qquad \nu = \frac{1}{3}, \frac{2}{5}, \ldots, \tag{4.4}$$

and small longitudinal conductivity at low temperature [Stormer, 1999].

A major conceptual breakthrough in the theory of the FQH effect was Laughlin's variational wave function for the principal series of fractions $\nu = 1/m$, with m odd [Laughlin, 1983],

$$\Psi_m(z_1, \ldots, z_M) = \prod_{i<j} (z_i - z_j)^m \exp\left(- \sum_k \frac{|z_k|^2}{4\ell_B^2} \right), \tag{4.5}$$

written here for M electrons in the lowest Landau level (LLL) using complex coordinates $z_j = x_j + iy_j$. This state represents an incompressible quantum liquid that avoids short-range repulsion by enforcing a zero of order m whenever two particles coincide. Its excitations are quasiparticles and quasiholes carrying fractional charge $e^* = e/m$, and, more subtly, fractional statistics [Laughlin, 1983]. Exact diagonalization and other numerical studies have shown that Laughlin's ansatz has extremely high overlap with the exact ground state for realistic interactions [Haldane, 1983].

The Laughlin series accounts for only a subset of the experimentally observed filling factors. A hierarchy construction due to Haldane (and independently Halperin) builds further incompressible states by condensing quasiparticles of a parent state into daughter Laughlin states, generating an infinite hierarchy of fractions [Haldane, 1983]. This picture was later complemented by the composite-fermion approach, which provides a unifying description of a large set of observed fractions in terms of integer quantum Hall states of emergent composite fermions [Jain, 1989].

Beyond the ground-state structure, FQH liquids host a rich spectrum of neutral collective modes. Girvin, MacDonald and Platzman (GMP) developed a single-mode approximation that predicts a gapped collective excitation with a dispersion featuring the so-called magnetoroton minimum at finite wave vector [Girvin, MacDonald, and Platzman, 1986]. This excitation may be viewed as a neutral density fluctuation with quadrupolar character, in the sense that it corresponds to a distortion of the electronic density that preserves the center of mass of the incompressible fluid while redistributing charge over a finite length scale. Within the single-mode approximation, this collective excitation evolves continuously from finite wave vector down to the long-wavelength limit, providing the natural continuation of the collective dynamics within a partially filled Landau level. In this limit, the excitation no longer represents a conventional density wave, but instead captures the lowest-energy internal deformation of the incompressible quantum liquid [Girvin, MacDonald, and Platzman, 1986].

Subsequent theoretical work has shown that, at sufficiently long wavelengths, this neutral excitation acquires a well-defined angular momentum (or "spin") character, effectively behaving as a spin–2 collective mode of the FQH liquid [Haldane, 2011; Liou et al., 2019]. For Laughlin states, these long-wavelength neutral modes become chiral: they propagate with a definite sense of rotation and couple selectively to probes carrying the corresponding angular momentum.

These chiral spin–2 modes have been termed "gravitons" of the FQH fluid, in

analogy with spin–2 excitations in gravitational theories. Liou *et al.* demonstrated that, in the limit of small wave vector, such modes appear as sharp resonances in appropriate response functions, confirming their spin–2 nature and their chiral structure [Liou et al., 2019].

Recent polarized Raman scattering experiments have provided compelling evidence for these chiral graviton modes in ultra–high-mobility GaAs samples [Liang et al., 2024]. Neutral excitations with well-defined chirality have been observed at filling factors such as $\nu = 1/3$ and $2/5$, with frequencies and selection rules consistent with theoretical predictions based on the long-wavelength magnetoroton dynamics [Liang et al., 2024; Yang, 2024].

From the perspective of this chapter, an important consequence of this description is that the low-energy collective dynamics of a FQH liquid are governed by internal deformations of the correlated electronic state rather than by rigid charge displacements. As a result, the linear electromagnetic response of a FQH liquid is inherently anisotropic and generally nonlocal, reflecting the fact that the relevant neutral excitations carry finite wave vector and angular momentum. In the following sections, we will exploit these properties to construct an effective electromagnetic susceptibility tensor for a 2DEG in the FQH regime and to analyze its consequences for the spectrum of an electromagnetic cavity.

4.1.2 Fractional quantum Hall liquids coupled to quantum light and graviton-polaritons

The study of light–matter interaction in cavities has revealed that the electromagnetic vacuum can profoundly modify material properties when the coupling between matter excitations and quantized cavity modes reaches the strong or ultrastrong coupling regime. In such regimes, the eigenmodes of the coupled system are hybrid light–matter quasiparticles known as polaritons, and even the ground state can acquire a polaritonic character [Garcia-Vidal, Ciuti, and Ebbesen, 2021].

A comprehensive theoretical treatment of FQH liquids coupled to quantum light has been developed by Bacciconi *et al.* [Bacciconi et al., 2025]. They consider a $\nu = 1/3$ Laughlin state embedded in a single-mode cavity whose electric field has a finite in-plane gradient, so that the cavity mode couples not only to the center-of-mass cyclotron motion but also to higher multipole moments of the electron density. By combining analytical arguments with tensor-network simulations of a fractional quantum Hall system on a cylinder, they arrive at several key conclusions.

First, the topological character of the Laughlin state remains remarkably robust under coupling to the nonlocal cavity vacuum field. In particular, the Hall conductance retains its quantized value $\sigma_{xy} = (1/3)\, e^2/h$, indicating that the bulk topological order is not destroyed by the cavity field [Bacciconi et al., 2025]. This is consistent with the general expectation that topological invariants are insensitive to weak to moderate perturbations that do not close the bulk gap.

Second, and most relevant for the present chapter, they demonstrate the existence of a new neutral quasiparticle in the low-energy spectrum: the *graviton-polariton*. At the field-theoretical level, the coupling between the cavity mode and the FQH fluid can be expressed in terms of a multipolar interaction between the electric field gradient and the quadrupolar (spin-2) collective mode of the internal metric. In other words, the cavity couples directly to the graviton mode of the FQH liquid. When the cavity frequency ω_{cav} is tuned near the graviton frequency ω_G, the two modes hybridize to form a pair of mixed light–matter eigenmodes with an avoided crossing in the spectrum,

$$\omega_{\pm} \approx \frac{\omega_{\text{cav}} + \omega_G}{2} \pm \sqrt{\left(\frac{\omega_{\text{cav}} - \omega_G}{2}\right)^2 + g^2}, \tag{4.6}$$

where g is an effective graviton–photon coupling strength controlled by the cavity field gradient and the geometric susceptibility of the FQH fluid [Bacciconi et al., 2025]. These hybrid modes are precisely the graviton-polaritons: their photonic component enables coupling to the external electromagnetic field, while their matter component inherits the spin-2 character and geometric structure of the underlying FQH graviton.

A crucial aspect of cavity–FQH coupling is that a homogeneous electric field cannot excite any low–energy neutral mode of a gapped fractional quantum Hall liquid. Due to translational invariance and LLL projection, long–wavelength dipole fluctuations are forbidden: the dipole operator only generates a rigid center–of–mass shift, which decouples from internal dynamics in the LLL (Kohn's theorem) and therefore carries no spectral weight in the neutral sector [Girvin, MacDonald, and Platzman, 1986; Haldane, 2011]. The leading internal deformation of the incompressible liquid is instead quadrupolar: the amplitude of long–wavelength density fluctuations satisfies $S(\boldsymbol{k}) \propto k^4$ [Girvin, MacDonald, and Platzman, 1986], reflecting the fact that the first nontrivial neutral excitation is the spin–2 "graviton" mode associated with fluctuations of the emergent quantum metric [Haldane, 2011; Liou et al., 2019]. Consequently, any coupling of light to neutral FQH excitations must arise from spatial gradients of the electromagnetic field. In the cavity setup of Ref. [Bacciconi et al., 2025], the in–plane field gradient selects precisely this quadrupolar channel, yielding a light–matter Hamiltonian whose leading term couples the cavity photon to the spin–2 quadrupole operator of the FQH fluid and enabling the formation of graviton–polaritons.

The graviton-polariton picture provides a natural bridge between the geometric description of FQH liquids and an effective electromagnetic response. From the geometric point of view, the relevant degrees of freedom are encoded in a dynamical internal metric and its spin-2 collective mode [Haldane, 2011; Liou et al., 2019]. From the electromagnetic point of view, the cavity couples to charge and current densities, which can be described by an effective susceptibility tensor. When the

light–matter coupling is dominated by quadrupolar matrix elements, the susceptibility acquires anisotropic and spatially dispersive contributions that effectively encode the response of the internal metric to the applied field.

In the next section we derive the electric susceptibility associated with the quadrupolar coupling between an electromagnetic field and a quantum system confined to two dimensions, which will turn out to be intrinsically anisotropic and to exhibit spatial dispersion. This susceptibility provides a compact description of the graviton-polariton coupling at the level of Maxwell's equations and allows us to compute the resulting frequency shifts and mode hybridization in a cavity geometry. In particular, we will show how the graviton-polariton physics manifests itself as a characteristic modification of the cavity spectrum and field distribution, providing a complementary viewpoint to the microscopic treatments of Ref. [Bacciconi et al., 2025] and directly connecting the internal quantum geometry of the FQH fluid to measurable electromagnetic observables.

4.2 Quadrupolar Optics

One way to describe the interaction energy of an electromagnetic wave with a quantum system, such as an atom or a molecule, is to use the form

$$- e^{i\boldsymbol{k}\cdot\boldsymbol{r}}\, \boldsymbol{E}_0 \cdot \boldsymbol{p}, \tag{4.7}$$

where $\boldsymbol{p} \equiv q\boldsymbol{r}$ denotes the dipole moment of the system and $\boldsymbol{E}_0$ is the amplitude of the electric field of the wave. At zeroth order, Eq. (4.7) reduces to the familiar expression of the energy of a dipole placed in an external electric field. At first order, however, in addition to the dipole term, one obtains

$$-iq\,(\boldsymbol{E}_0 \cdot \boldsymbol{r})(\boldsymbol{k} \cdot \boldsymbol{r}), \tag{4.8}$$

which represents the contribution of the electric quadrupole and the magnetic dipole. Since we want to study the phenomena related to the graviton, which, as mentioned in Section 4.1, is connected to quadrupolar fluctuations, we will use only Eq. (4.8) as the sole contribution to the interaction energy, disregarding lower- and higher-order contributions. In view of the discussion in the following sections and of the purpose of this chapter, we shall explicitly assume that the relevant quadrupolar excitation carries angular momentum $L_z = -2$.

In matter, the electric displacement field is given by [Jackson, 1999]

$$\boldsymbol{D} = \epsilon_0 \boldsymbol{E} + \boldsymbol{P} - \nabla \cdot \overleftrightarrow{Q}' + \ldots \tag{4.9}$$

where $\boldsymbol{P}$ is the polarization density vector and $\overleftrightarrow{Q}'$ denotes the electric quadrupole density. Since we are interested precisely in the last term of Eq. (4.9), it is necessary

to evaluate its expectation value, i.e. its macroscopic average, in order to define

$$-\nabla \cdot \langle \overleftrightarrow{Q}' \rangle \equiv \epsilon_0 \overleftrightarrow{\chi} \cdot \boldsymbol{E} \implies -\sum_b \frac{\partial \langle Q'^{ab} \rangle}{\partial x_b} = \epsilon_0 \sum_\gamma \chi_{a\gamma} E_\gamma, \tag{4.10}$$

and thereby extract the effective susceptibility tensor $\overleftrightarrow{\chi}$, which is the ultimate goal of the current section.

The electric quadrupole density $\langle Q'^{ab} \rangle$ is related to the quadrupole moment $\langle Q^{ab} \rangle \equiv \frac{1}{2} q \langle x_a x_b \rangle$ [Jackson, 1999] through

$$\langle Q'^{ab} \rangle = n \langle Q^{ab} \rangle e^{i\boldsymbol{k}\cdot\boldsymbol{r}}, \tag{4.11}$$

where n is the atomic number density. Assuming a uniform distribution of atoms, one can write

$$\langle Q'^{ab} \rangle = \sum_\nu \langle Q^{ab} \rangle_\nu \, \delta(\boldsymbol{r} - \boldsymbol{r}_\nu) = \langle Q^{ab} \rangle \sum_\nu e^{i\boldsymbol{k}\cdot\boldsymbol{r}_\nu} \, \delta(\boldsymbol{r} - \boldsymbol{r}_\nu) = n \langle Q^{ab} \rangle e^{i\boldsymbol{k}\cdot\boldsymbol{r}}.$$

To evaluate $\langle Q^{ab} \rangle$, we employ time-dependent perturbation theory, where Eq. (4.8) provides the time-dependent interaction term in the Hamiltonian. Given the wavefunction $|\psi(t)\rangle = \sum_j C_j(t)|\phi_j\rangle$ and the generic interaction Hamiltonian

$$H_{\text{int}} = \left(V e^{-i\omega t} + V^* e^{i\omega t} \right) e^{\gamma t}, \tag{4.12}$$

the time-dependent perturbation theory predicts that the coefficients take the form [Scully and Zubairy, 1997; Sakurai and Napolitano, 2011]

$$C_j(t) = \frac{e^{\gamma t}}{i\hbar} \left\{ \frac{V_{j0} \, e^{i(\omega_j - \omega_0 - \omega)t}}{i(\omega_j - \omega_0 - \omega) + \gamma} + \frac{V_{0j}^* \, e^{i(\omega_j - \omega_0 + \omega)t}}{i(\omega_j - \omega_0 + \omega) + \gamma} \right\}, \tag{4.13}$$

where $V_{j0} \equiv \langle j|V|0\rangle$ is the matrix element associated with the transition between the ground state and the j-th level and γ is a damping coefficient. In our specific case, where a single transition is allowed,[1] the coefficient reduces to

$$C(t) = \frac{e^{\gamma t}}{i\hbar} \left\{ \frac{V_{20} \, e^{i(\omega_2 - \omega_0 - \omega)t}}{i(\omega_2 - \omega_0 - \omega) + \gamma} + \frac{V_{02}^* \, e^{i(\omega_2 - \omega_0 + \omega)t}}{i(\omega_2 - \omega_0 + \omega) + \gamma} \right\}, \tag{4.14}$$

with

$$V_{20} \equiv -\langle 2| \, iq(\boldsymbol{E}_0 \cdot \boldsymbol{r})(\boldsymbol{k} \cdot \boldsymbol{r}) \, |0\rangle, \tag{4.15}$$

[1] In accordance with the above assumption, we focus on the situation in which the only relevant quadrupolar excitation of the system carries angular momentum $L_z = -2$. Therefore, the only optically active transition from the ground state is to the state whose angular momentum quantum number differs by two units. All other matrix elements vanish identically. We thus truncate the Hilbert space to the $j = 2$ sector, which is the only one that contributes to the quadrupolar response.

given the form of Eq. (4.8). From here on, whenever we write $|2\rangle$, it is implicitly understood as the state $|2,-2\rangle$, i.e. the excited state with angular momentum $L_z = -2$.

At this stage, the expectation value $\langle Q^{ab}\rangle$ is given by

$$\begin{aligned}\langle\psi(t)|Q^{ab}|\psi(t)\rangle = e^{i(\omega_0-\omega_2)t}\,C(t)\,\langle 0|\,Q^{ab}\,|2\rangle \\ + e^{-i(\omega_0-\omega_2)t}\,C^*(t)\,\langle 2|\,Q^{ab}\,|0\rangle.\end{aligned} \tag{4.16}$$

Neglecting negative-frequency terms and antiresonant contributions, Eq. (4.16) reduces to

$$\langle Q^{ab}\rangle = \frac{iq}{\hbar}\,\frac{\langle 0|\,Q^{ab}\,|2\rangle\;\langle 2|\,(\boldsymbol{E}_0\cdot\boldsymbol{r})(\boldsymbol{k}\cdot\boldsymbol{r})\,|0\rangle}{\omega_2-\omega_0-\omega-i\gamma}\,e^{-i\omega t}\,e^{\gamma t}. \tag{4.17}$$

Since the electronic system is strictly two-dimensional and confined to the plane $z=0$, the position operator has no out-of-plane component, i.e. $\mathbf{r}=(x,y,0)$. As a consequence, the quadrupolar matrix elements only involve the in-plane coordinates and fields, and the out-of-plane components k_z and E_z^0 do not contribute. We can therefore restrict all vectors to their in-plane parts and write

$$\begin{aligned}\boldsymbol{r} &= x\hat{x}+y\hat{y},\\ \boldsymbol{k} &= k_x\hat{x}+k_y\hat{y},\\ \boldsymbol{E}_0 &= E_x^0\,\hat{x}+E_y^0\,\hat{y},\end{aligned}$$

To compute the matrix element, it is convenient to move from Cartesian quantities to those expressed in the circular basis $\{\hat{\sigma}_+,\hat{\sigma}_-\}$. With $\hat{\sigma}_\pm \equiv (\hat{x}\pm i\hat{y})/\sqrt{2}$, we obtain:

$$\boldsymbol{r} = r_-\hat{\sigma}_+ + r_+\hat{\sigma}_-, \quad \text{where} \quad r_\pm \equiv \tfrac{1}{\sqrt{2}}\left(x\pm iy\right), \tag{4.18a}$$

$$\boldsymbol{k} = k_-\hat{\sigma}_+ + k_+\hat{\sigma}_-, \quad \text{where} \quad k_\pm \equiv \tfrac{1}{\sqrt{2}}\left(k_x\pm ik_y\right), \tag{4.18b}$$

$$\boldsymbol{E}_0 = E_-^0\,\hat{\sigma}_+ + E_+^0\,\hat{\sigma}_-, \quad \text{where} \quad E_\pm^0 \equiv \tfrac{1}{\sqrt{2}}\left(E_x^0\pm iE_y^0\right). \tag{4.18c}$$

Using the identity $\boldsymbol{v}\cdot\boldsymbol{w} = v_+w_- + v_-w_+$ and the selection rules for transitions between $|0\rangle$ and $|2\rangle$, we find:

$$\begin{aligned}\langle 2|\,(\boldsymbol{E}_0\cdot\boldsymbol{r})(\boldsymbol{k}\cdot\boldsymbol{r})\,|0\rangle &= \langle 2|\,(E_+^0\,r_- + E_-^0\,r_+)\,(k_+r_- + k_-r_+)\,|0\rangle\\ &= \langle 2|\,E_+^0\,r_-\,k_+r_-\,|0\rangle\\ &= E_+^0\,k_+\,\langle 2|\,r_-^2\,|0\rangle.\end{aligned} \tag{4.19}$$

On the other hand, recalling that $Q^{ab} = \frac{1}{2}q\,x_ax_b$, the matrix elements $\langle 0|\,Q^{ab}\,|2\rangle$ read:

$$\begin{aligned} a=b=x \qquad & \tfrac{1}{4}\,e\,\langle 0|\,r_+^2\,|2\rangle,\\ a=x,\,b=y \qquad & -\tfrac{i}{4}\,e\,\langle 0|\,r_+^2\,|2\rangle,\\ a=y,\,b=x \qquad & -\tfrac{i}{4}\,e\,\langle 0|\,r_+^2\,|2\rangle,\end{aligned}$$

$$a = b = y \qquad -\tfrac{1}{4}\, e\, \langle 0|\, r_+^2\, |2\rangle.$$

Thus, the expectation value of Q^{ab} becomes

$$\langle \overleftrightarrow{Q} \rangle = \frac{iq^2}{4\hbar}\, |\langle 0|r_+^2|2\rangle|^2\, \frac{E_+^0\, k_+\, e^{-i\omega t}\, e^{\gamma t}}{\omega_2 - \omega_0 - \omega - i\gamma} \begin{pmatrix} 1 & -i \\ -i & -1 \end{pmatrix}. \tag{4.20}$$

Now consider the divergence:

$$-\sum_b \frac{\partial \langle Q'^{ab} \rangle}{\partial x_b} = -n \sum_b \langle Q^{ab} \rangle\, \frac{\partial}{\partial x_b} \left[e^{i\mathbf{k}\cdot\boldsymbol{r}} \right]. \tag{4.21}$$

This yields:

$$\begin{aligned} -\nabla \cdot \langle \overleftrightarrow{Q'} \rangle &= -\frac{inq^2}{4\hbar}\, \frac{|\langle 0|r_+^2|2\rangle|^2\, e^{-i\omega t}\, e^{\gamma t}}{\omega_2 - \omega_0 - \omega - i\gamma}\, E_+^0\, e^{i\vec{k}\cdot\vec{r}}\, k_+ \begin{pmatrix} ik_x + k_y \\ k_x - ik_y \end{pmatrix} \\ &= \frac{nq^2}{8\hbar}\, \frac{|\langle 0|r_+^2|2\rangle|^2\, e^{-i\omega t}\, e^{\gamma t}}{\omega_2 - \omega_0 - \omega - i\gamma}\, (k_x^2 + k_y^2)(E_x + iE_y) \begin{pmatrix} 1 \\ -i \end{pmatrix} \\ &= \frac{nq^2}{8\hbar}\, |\langle 0|r_+^2|2\rangle|^2\, \frac{e^{-i\omega t}\, e^{\gamma t}\, (k_x^2 + k_y^2)}{\omega_2 - \omega_0 - \omega - i\gamma} \begin{pmatrix} 1 & i \\ -i & 1 \end{pmatrix} \begin{pmatrix} E_x \\ E_y \end{pmatrix}. \end{aligned}$$

Therefore, we can define

$$-\nabla \cdot \langle \overleftrightarrow{Q'} \rangle \equiv \epsilon_0 \overleftrightarrow{\chi} \cdot \boldsymbol{E} \tag{4.22}$$

with

$$\begin{aligned} \overleftrightarrow{\chi}(\omega, \mathbf{k}) &= \frac{\tilde{n}q^2}{8\,\epsilon_0\,\hbar}\, \frac{|\langle 0|r_+^2|2\rangle|^2\, k_{/\!/}^2}{\omega_2 - \omega_0 - \omega - i\gamma} \begin{pmatrix} 1 & i \\ -i & 1 \end{pmatrix} \delta(z) \\ &= \frac{\Lambda\, k_{/\!/}^2}{\omega_2 - \omega_0 - \omega - i\gamma} \begin{pmatrix} 1 & i \\ -i & 1 \end{pmatrix} \delta(z), \end{aligned} \tag{4.23}$$

where $\tilde{n}$ is the surface charge density, defined by $n = \tilde{n}\,\delta(z)$ since the 2DEG lies on the $z = 0$ plane, $k_{/\!/}$ is the modulus of the in-plane wave vector and Λ is defined by[2]

$$\Lambda \equiv \frac{\tilde{n}q^2}{8\,\epsilon_0\,\hbar}\, |\langle 0|r_+^2|2\rangle|^2. \tag{4.24}$$

The structure of Eq. (4.23) is closely related to that of gyrotropic media, such as ferrites or plasmas in an external magnetic field [Landau and Lifshitz, 1984; Agranovich and Ginzburg, 1984]. In the present case, however, the gyrotropy does not arise from a macroscopic magnetization but from the *quadrupolar* matrix element associated with the unique transition excited by the operator r^2, which couples the ground state only to the single excited state whose angular momentum differs by

[2] In a 2DEG exhibiting the FQH effect, the charge q appearing in all the expressions written in this section corresponds to the charge of the elementary excitation involved in the quadrupolar transition. In this context, it is equal to the electronic charge e [Bacciconi et al., 2025].

two units. Accordingly, Eq. (4.23) describes any two-dimensional system whose electric response, in the frequency range of interest, is governed by this isolated quadrupolar transition, with all other multipolar channels and higher excitations negligible. This situation is realized, as mentioned in the previous section, in 2D electron systems under a strong perpendicular magnetic field, where the dominant low-energy optical excitation is a "graviton-like" quadrupolar mode.

The medium described by Eq. (4.23) does not satisfy any of the three fundamental symmetries discussed in Chapter 2 when $\gamma \neq 0$; it therefore lies outside all colored subsets shown in Fig. 2.4. In contrast, in the limit $\gamma \to 0$ the medium recovers energy conservation and thus falls within the red subset.

Further insights can be obtained by diagonalizing the susceptibility tensor. Its eigenvectors are, of course, the two circular polarizations

$$\mathbf{e}_+ \propto \begin{pmatrix} 1 \\ i \end{pmatrix} \quad \leftrightarrow \quad \hat{\sigma}_+, \qquad \mathbf{e}_- \propto \begin{pmatrix} 1 \\ -i \end{pmatrix} \quad \leftrightarrow \quad \hat{\sigma}_-, \tag{4.25}$$

whereas the corresponding eigenvalues are

$$\chi_+(\omega, \boldsymbol{k}_{/\!/}) = 0, \qquad \chi_-(\omega, \boldsymbol{k}_{/\!/}) = \frac{2\Lambda\, k_{/\!/}^2}{\omega_2 - \omega_0 - \omega - i\gamma}\, \delta(z). \tag{4.26}$$

In other words, the medium responds only to the $\hat{\sigma}_-$ polarization, while the $\hat{\sigma}_+$ polarization experiences no quadrupolar response at all and propagates as if in vacuum because $\epsilon_r^+ = 1$. This is the electromagnetic fingerprint of the underlying chiral quadrupolar selection rule: the interaction Hamiltonian is proportional to r_+^2, and therefore couples exclusively to one handedness of the field.

The dependence on $k_{/\!/}$ in Eq. (4.23) is an example of *spatial dispersion*, i.e. nonlocality of the material response in space [Landau and Lifshitz, 1984; Agranovich and Ginzburg, 1984; Forcella, Prada, and Carminati, 2017]. From a physical point of view, spatial dispersion reflects the fact that the microscopic components of the medium do not respond independently. Instead, their motion is correlated over finite distances, so the response at one point depends on the electric field in its neighborhood. In Fourier space this manifests as a k-dependent susceptibility, while in real space it corresponds to constitutive relations involving spatial derivatives of the fields. In our particular case, the factor $k_{/\!/}^2$ corresponds, for slowly varying fields, to the operator substitution

$$k_{/\!/}^2 \;\longrightarrow\; -\nabla_{/\!/}^2, \tag{4.27}$$

so that the quadrupolar contribution to the displacement field can be written as

$$-\nabla \cdot \langle \overleftrightarrow{Q'} \rangle \;\propto\; -\nabla_{/\!/}^2 \boldsymbol{E}_{/\!/}, \tag{4.28}$$

where $\boldsymbol{E}_{/\!/}$ denotes the in-plane electric field. This shows that the response is suppressed for spatially uniform fields and enhanced in regions where the field varies rapidly on the scale set by the microscopic length entering Λ.

To conclude, given the susceptibility of the 2DEG in Eq. (4.23) and the relation

$$\overleftrightarrow{\epsilon}(\omega,\mathbf{k}) = \overleftrightarrow{I} + \frac{i}{\omega\,\epsilon_0}\,\overleftrightarrow{\sigma}(\omega,\mathbf{k}),$$

the conductivity of the 2DEG sheet is written as

$$\overleftrightarrow{\sigma}(\omega,\mathbf{k}) = -\frac{\Lambda\,\epsilon_0\,\omega\,k_{/\!/}^2}{\omega_2-\omega_0-\omega-i\gamma}\begin{pmatrix} i & -1 \\ 1 & i \end{pmatrix}\delta(z). \tag{4.29}$$

Equation (4.29) will be used in Section 4.3 to determine the eigenmodes of the 2DEG layer in an external magnetic field.

4.3 Surface Eigenmodes of the 2DEG

In this section, we derive the dispersion relation of the electromagnetic surface modes supported by the 2DEG sheet under an external magnetic field. The ultimate goal of this analysis is to obtain and describe the eigenmodes of the 2DEG layer, which will later in the chapter be coupled to the electromagnetic field of a cavity.

In addition to the single-layer configuration, we will also examine a system composed of two parallel sheets: one made of 2DEG and one metallic. The reason is that among the various cavity configurations analyzed in Section 4.4, one can indeed be modeled in this way—that is, as a structure with a metallic substrate beneath the layer in the FQH regime. Therefore, to determine the surface-mode dispersion of the different configurations, we will carry out the analytic derivation directly for the two-layer system, and then analyze the single-layer case as a simple limiting situation.

A crucial point is that the derivation presented below is deliberately formulated in its *most general form*. We will not assume any particular microscopic model for the two conducting sheets, until the very end of the section. The calculation below depends only on the fact that each sheet is characterized by a generic in-plane conductivity tensor

$$\overleftrightarrow{\sigma} = \begin{pmatrix} \sigma_{xx} & \sigma_{xy} \\ \sigma_{yx} & \sigma_{yy} \end{pmatrix}, \tag{4.30}$$

whose frequency dependence is left completely arbitrary.

4.3.1 Analytical derivation of the dispersion relation

The system under consideration is sketched in Fig. 4.1. Two conductive sheets with conductivity tensors $\overleftrightarrow{\sigma}_L$ (*left*) and $\overleftrightarrow{\sigma}_R$ (*right*) are located at $z = 0$ and $z = d$, respectively, and exhibit a Hall response—resulting in nonzero off-diagonal elements due to a perpendicular magnetic field $\boldsymbol{B} = B\hat{z}$. The three dielectric regions into which space is divided have permittivities ϵ_1, ϵ_2, and ϵ_3.

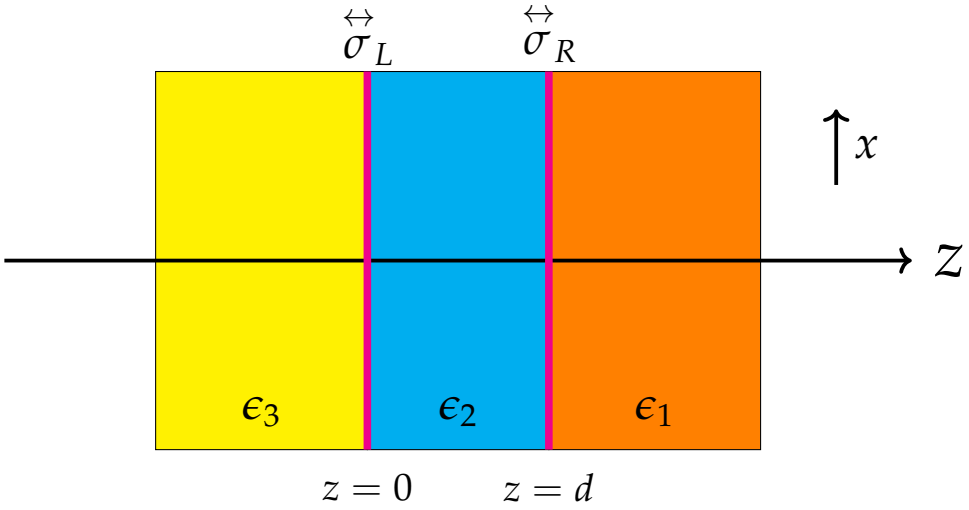

FIGURE 4.1: Schematic illustration of the system under investigation. The ϵ_i denote the dielectric constants of the three media, while the $\overleftrightarrow{\sigma}_i$ are the anisotropic conductivities of the two 2D layers, shown in magenta.

One might initially expect that the appropriate procedure would be to treat TM and TE modes separately, as for standard configurations. However, in the present problem this decomposition fails: the presence of off-diagonal terms in $\overleftrightarrow{\sigma}_i$ introduces a coupling between the tangential components of the electric field at each sheet, and consequently couples TE and TM polarized waves. Physically, the medium response generates a surface current transverse to the applied electric field, so that a TM-polarized wave (with E_x and E_z components) induces a transverse surface current that in turn produces a TE field component (and vice versa). Thus, one must start with a field that is a superposition of both polarizations.

We therefore consider the generic electric field of an electromagnetic plane wave

$$\mathbf{E}_m(x,z,t) = \Big(E_{mx}(z), E_{my}(z), E_{mz}(z)\Big)\, e^{i(k_x x - \omega t)}, \tag{4.31}$$

that propagates with the wave vector

$$\mathbf{k}_m = (k_x, 0, k_{mz})\,, \tag{4.32}$$

where $m = 1,2,3$ is the index that characterizes the medium. The choice of $\mathbf{E}_m$ and $\mathbf{k}_m$ is made to ensure translational invariance in y, homogeneous propagation along x, and confinement along z.

Apart from the common exponential factor, the electric field components can be written as

$$\begin{aligned} E_{1i}(z) &= \mathcal{E}_i^1 e^{ik_{1z}z}, \\ E_{2i}(z) &= \mathcal{E}_i^{2+} e^{ik_{2z}z} + \mathcal{E}_i^{2-} e^{-ik_{2z}z}, \\ E_{3i}(z) &= \mathcal{E}_i^3 e^{ik_{3z}z}, \end{aligned}$$

where $i = x, y, z$.

Proceeding with the analytical calculations, one can show that the physical system under consideration is governed by the equation

$$\left(\begin{array}{c|c} A & B \\ \hline C & D \end{array}\right) \begin{pmatrix} \mathcal{E}_x^3 \\ \mathcal{E}_x^{2+} \\ \mathcal{E}_x^{2-} \\ \mathcal{E}_x^1 \\ \mathcal{E}_y^3 \\ \mathcal{E}_y^{2+} \\ \mathcal{E}_y^{2-} \\ \mathcal{E}_y^1 \end{pmatrix} = \begin{pmatrix} 0 \\ 0 \\ 0 \\ 0 \\ 0 \\ 0 \\ 0 \\ 0 \end{pmatrix}, \tag{4.33}$$

where A, B, C, and D are 4×4 blocks. The analytical derivation of this result and the explicit form of the four matrix blocks are reported in Appendix C.

The cancellation of the determinant of the full 8×8 matrix determines the mode dispersion relation in the general case. It is now convenient to study the simplest configuration compatible with the symmetries of a system permeated by a homogeneous external magnetic field oriented along $\hat{z}$. In that case we can assume

$$\sigma_{xx}^R = \sigma_{yy}^R, \qquad \sigma_{xx}^L = \sigma_{yy}^L, \tag{4.34}$$

and, in the lossless limit,

$$\sigma_{xy}^R = -\sigma_{yx}^R, \qquad \sigma_{xy}^L = -\sigma_{yx}^L. \tag{4.35}$$

Indeed, Eq. (4.29) satisfies Eq. (4.34) in all cases, and Eq. (4.35) in the limit $\gamma \to 0$.

Finally, if the right conductive sheet is in contact only with vacuum (i.e., $\epsilon_1 = \epsilon_2 = 1$), while medium 3 is still a generic material characterized by a permittivity ϵ_3, the condition $\det = 0$ for the full 8×8 matrix yields, after straightforward but lengthy algebra, the following dispersion equation:

$$\mathcal{C}_4\, e^{4\beta_1 d} + \mathcal{C}_2\, e^{2\beta_1 d} + \mathcal{C}_0 = 0, \tag{4.36}$$

where

$$\begin{aligned} \mathcal{C}_0 &= \beta_1 \mu_0 \left(\sigma_{xy}^R \sigma_{yx}^R - \sigma_{xx}^R \sigma_{yy}^R\right) \omega \\ &\times \Bigg[i\,\beta_1(\beta_1 - \beta_3)\beta_3\, \sigma_{xx}^L + \left(\beta_3^2 \epsilon_0 + \beta_1^2 \epsilon_0 \epsilon_3 - \beta_1 \beta_3 \left(\epsilon_0 + \epsilon_0 \epsilon_3 - \mu_0 \sigma_{xy}^L \sigma_{yx}^L + \mu_0 \sigma_{xx}^L \sigma_{yy}^L\right)\right)\omega \\ &\qquad - i\,\epsilon_0(\beta_3 - \beta_1 \epsilon_3)\mu_0 \sigma_{yy}^L\, \omega^2 \Bigg], \end{aligned}$$

$$\mathcal{C}_4 = -\left[2\beta_1^2 \sigma_{xx}^R - i\beta_1 \left(4\epsilon_0 - \mu_0 \sigma_{xy}^R \sigma_{yx}^R + \mu_0 \sigma_{xx}^R \sigma_{yy}^R\right)\omega - 2\epsilon_0 \mu_0 \sigma_{yy}^R \omega^2\right]$$

$$\times\Big[\beta_1\beta_3(\beta_1+\beta_3)\sigma^L_{xx}-i\Big(\beta_3^2\epsilon_0+\beta_1^2\epsilon_0\epsilon_3+\beta_1\beta_3\Big(\epsilon_0+\epsilon_0\epsilon_3-\mu_0\sigma^L_{xy}\sigma^L_{yx}+\mu_0\sigma^L_{xx}\sigma^L_{yy}\Big)\Big)\omega$$
$$-\epsilon_0(\beta_3+\beta_1\epsilon_3)\mu_0\sigma^L_{yy}\,\omega^2\Big],$$

$$\mathcal{C}_2=2\Big[\beta_1^3\beta_3(\beta_1+\beta_3)\sigma^L_{xx}\sigma^R_{xx}$$
$$-i\beta_1^2\Big(\beta_1^2\epsilon_0\epsilon_3\sigma^R_{xx}+\beta_1\beta_3\sigma^R_{xx}\Big(\epsilon_0(\epsilon_3-1)-\mu_0\sigma^L_{xy}\sigma^L_{yx}+\mu_0\sigma^L_{xx}\sigma^L_{yy}\Big)$$
$$-\beta_3^2\Big(\epsilon_0\sigma^R_{xx}+\mu_0\sigma^L_{xx}(\sigma^R_{xy}\sigma^R_{yx}-\sigma^R_{xx}\sigma^R_{yy})\Big)\Big)\omega$$
$$-\beta_1\mu_0\Big(\beta_1^2\epsilon_0\epsilon_3\sigma^R_{xx}\sigma^L_{yy}+\beta_3^2\epsilon_0\sigma^L_{xx}\sigma^R_{yy}+\beta_1\beta_3\Big[\mu_0(\sigma^L_{xy}\sigma^L_{yx}-\sigma^L_{xx}\sigma^L_{yy})(\sigma^R_{xy}\sigma^R_{yx}-\sigma^R_{xx}\sigma^R_{yy})$$
$$+\epsilon_0\Big(2\sigma^L_{xy}\sigma^R_{yx}+\sigma^R_{xy}(2\sigma^L_{yx}+\sigma^R_{yx}-\epsilon_3\sigma^R_{yx})-\sigma^R_{xx}\sigma^L_{yy}+\epsilon_3\sigma^R_{xx}\sigma^R_{yy}-(\sigma^L_{xx}+\sigma^R_{xx})\sigma^R_{yy}\Big)\Big]\Big)\omega^2$$
$$-i\epsilon_0\mu_0\Big(-\beta_3^2\epsilon_0\sigma^R_{yy}+\beta_1\beta_3(\epsilon_0-\epsilon_0\epsilon_3+\mu_0\sigma^L_{xy}\sigma^L_{yx}-\mu_0\sigma^L_{xx}\sigma^L_{yy})\sigma^R_{yy}$$
$$+\beta_1^2\epsilon_3\Big(\epsilon_0\sigma^R_{yy}+\mu_0\sigma^L_{yy}(\sigma^R_{xy}\sigma^R_{yx}-\sigma^R_{xx}\sigma^R_{yy})\Big)\Big)\omega^3$$
$$+\epsilon_0^2(\beta_3+\beta_1\epsilon_3)\mu_0^2\sigma^L_{yy}\sigma^R_{yy}\omega^4\Big],$$

and

$$\beta_1\equiv+\sqrt{k_x^2-\frac{\omega^2}{c^2}},\qquad \beta_3\equiv+\sqrt{k_x^2-\epsilon_3\frac{\omega^2}{c^2}}. \tag{4.37}$$

Equation (4.36) encodes the fully coupled hybrid surface modes supported by the two parallel layers in the presence of a perpendicular magnetic field. By substituting Eq. (4.37) in Eq. (4.36), it is possible to obtain the dispersion relation $\omega=\omega(k_x)$ of the surface mode. The resulting dispersion is the general hybrid surface mode supported by two parallel anisotropic conducting sheets. In the case of a single sheet immersed in vacuum, the dispersion relation reduces to the much simpler form

$$\left(\frac{2}{\beta_1}+i\,\frac{\sigma_{xx}}{\epsilon_0\omega}\right)\left(2\,\beta_1-i\,\frac{\mu_0\omega}{2}\,\sigma_{yy}\right)-\frac{\mu_0}{2\,\epsilon_0}\,\sigma_{xy}^2=0. \tag{4.38}$$

which, as anticipated earlier, shows the TM and TE modes to be inevitably coupled due to the presence of off-diagonal terms in the conductivity tensor.

4.3.2 Eigenmodes of the 2DEG sheet

Using the dispersion relations in Eqs. (4.36) and (4.38) together with the field–matching matrix formulated in Eq. (4.33), we determine the electromagnetic surface modes supported by both the single-layer and two-layer configurations. The material response enters through the surface conductivity tensors of the individual sheets.

For the 2DEG in an external magnetic field, we employ the gyrotropic conductivity model given in Eq. (4.29) in the lossless limit and with $k_{/\!/} = k_x$, while for the metallic sheet we use a Drude-type lossless gyrotropic conductivity. In particular, we used the conductivity of graphene, which takes the form

$$\boldsymbol{\sigma}(\omega) = \begin{pmatrix} \sigma_{xx}(\omega) & \sigma_{xy}(\omega) \\ -\sigma_{xy}(\omega) & \sigma_{xx}(\omega) \end{pmatrix},$$

$$\sigma_{xx}(\omega) = i\,\frac{e^2 E_F}{\pi\hbar^2}\,\frac{\omega}{\omega^2 - \omega_{\mathrm{cyc}}^2},$$

$$\sigma_{xy}(\omega) = \frac{e^2 E_F}{\pi\hbar^2}\,\frac{\omega_{\mathrm{cyc}}}{\omega^2 - \omega_{\mathrm{cyc}}^2},$$

where E_F denotes the Fermi energy and ω_{cyc} stands for the cyclotron frequency. For the *single-layer configuration*, the resulting field distribution is shown in Fig. 4.2. Extending the same formalism to a *two-layer structure*, where the electromagnetic fields in the intermediate region are expressed as a superposition of upward- and downward-decaying evanescent waves, leads to the coupled-mode profiles shown in Fig. 4.3. Since the purpose of this configuration is to anticipate the analysis presented in the following section—which focuses on the coupling between the 2DEG layer and a metallic half-space—we choose the dielectric constant of the upper medium to be $\epsilon_3 = -10$. This value effectively captures the qualitative electromagnetic response of a metallic environment, allowing us to highlight the key features of metal-induced mode hybridization without introducing the full complexity of a realistic cavity geometry. Notably, because both conducting sheets and the lower half space exhibit metal-like optical responses in the frequency range of interest, while the remaining part of the space is a dielectric (vacuum), the resulting field-line patterns in both configurations closely resemble those of conventional surface plasmon polaritons. The characteristic confinement and directional flow of the fields clearly reflect the effective plasmonic nature of the 2DEG–metal system.

4.4 Cavity Resonators

In this section we propose and analyze minimal experimental configurations to excite gravitons and observe how they modify the eigenmodes of a cavity hosting a 2DEG, producing a frequency shift that can, in principle, be experimentally detected. We consider three representative setups.

The first configuration is the most natural one from an electromagnetic perspective and consists of coupling the FQH layer to a parallel metallic slab in the presence of a uniform external magnetic field B, giving rise to magnetoplasmon–graviton

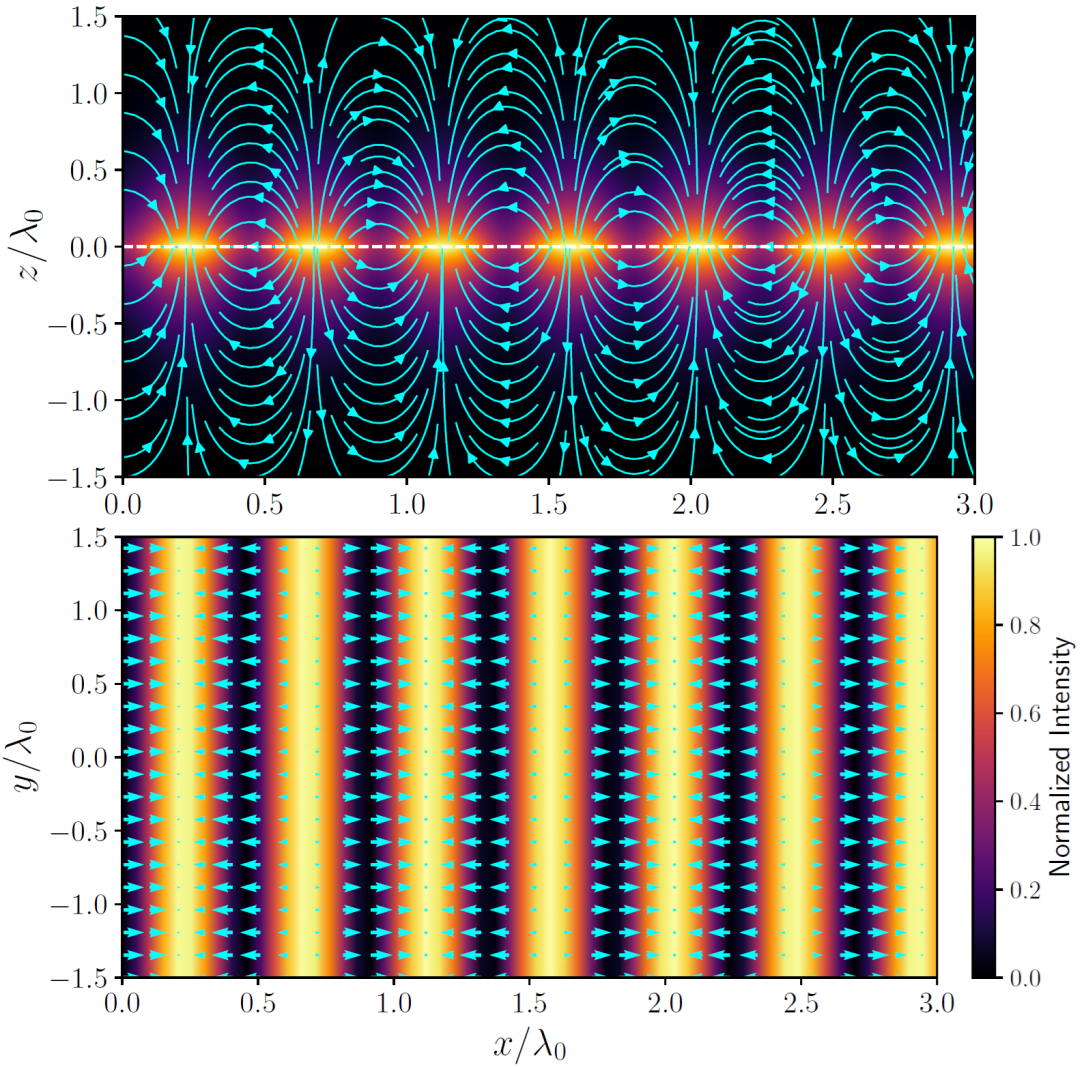

FIGURE 4.2: Electric field distribution in the xz (top panel) and xy (bottom panel) planes for the single-layer 2DEG configuration under the FQH regime. Spatial coordinates are normalized to the vacuum wavelength. The parameters used are $\omega = 2 \times 10^{11}$ Hz and $\Lambda = 10^{-10}\,\mathrm{m}^3/\mathrm{s}$.

hybridization. While this setup is conceptually appealing, for the realistic parameters considered here the resulting frequency shift turns out to be too small to be experimentally resolved.

We therefore proceed to analyze two electrode-based resonator geometries, which allow for a much stronger control of the electric-field gradients at the 2DEG position. In the second setup the graviton chiralities are not resolved, whereas in the third configuration they are selectively addressed and distinctly resolved. These latter two configurations yield substantially larger frequency shifts and therefore represent the most promising routes toward experimental detection of graviton-induced cavity effects. Finally, we also analyze a fourth configuration consisting of a spherical plasmonic nanoparticle.

To begin with, one must find a way to estimate the frequency shift $\Delta\omega_c$ of the

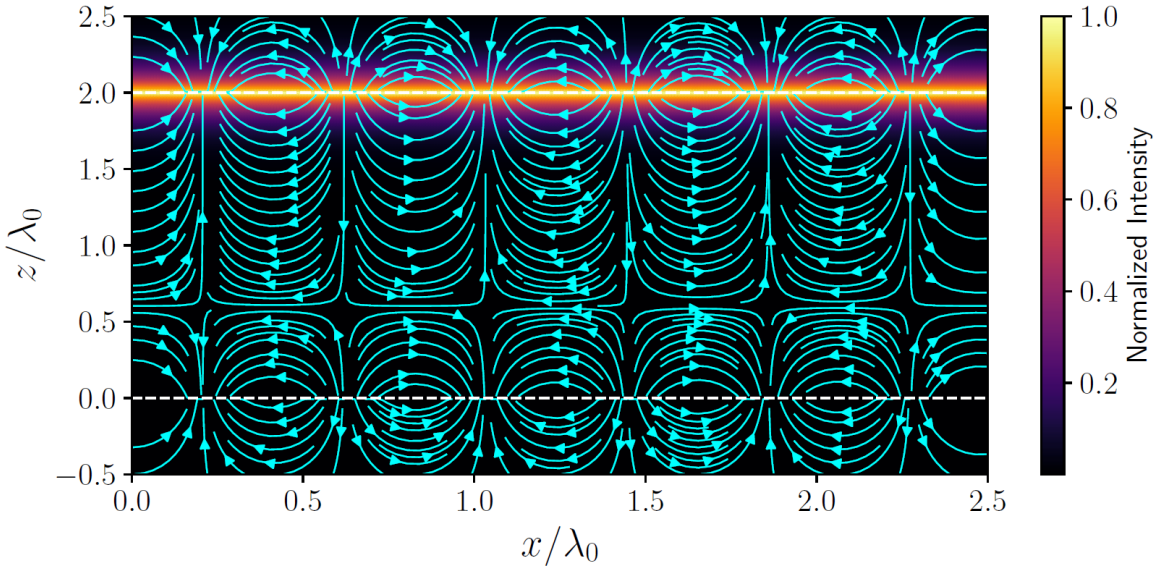

FIGURE 4.3: Electric field distribution in the xz plane for the two-layer configuration consisting of a 2DEG under the FQH regime (at $z = 0$) coupled to a metallic graphene sheet. Spatial coordinates are normalized to the vacuum wavelength. The parameters used are $\omega = 2 \times 10^{11}$ Hz, $E_F = 0.1$ eV, $\epsilon_3 = -10$, and $\Lambda = 1 \times 10^{-10}\,\mathrm{m^3\,s^{-1}}$.

cavity induced by the introduction of the 2DEG. Let ω_c be the eigenfrequency of the unperturbed cavity. The most convenient approach is to treat $\Delta\omega_c$ as a small perturbation of ω_c, thereby constructing a perturbative theory. The value of $\Delta\omega_c$ obtained from the calculations is bounded below by the experimental resolution with which a frequency shift can be detected, and above by the self-consistency of the perturbative theory itself: if the calculations were to yield $\Delta\omega_c \sim \omega_c$, the theory would no longer be valid. In the most favorable scenario, one may conservatively assume $\Delta\omega_c \approx 0.1\,\omega_c$ as an upper bound for the frequency shift, beyond which the perturbative description would no longer be reliable.

Given an unperturbed cavity of volume $\mathcal{V}$ with a real, isotropic dielectric function $\epsilon(\mathbf{r})$, into which an isotropic element is introduced that modifies the profile of the dielectric function by an amount $\Delta\epsilon(\mathbf{r})$, the frequency shift can be estimated as [Joannopoulos et al., 2008; Cognée et al., 2019; Gérard, 2003]

$$\Delta\omega_c = -\frac{\omega_c}{2}\frac{\int_{\mathcal{V}} \Delta\epsilon(\mathbf{r})\,|\mathbf{E}(\mathbf{r})|^2\,\mathrm{d}^3\mathbf{r}}{\int_{\mathcal{V}} \epsilon(\mathbf{r})\,|\mathbf{E}(\mathbf{r})|^2\,\mathrm{d}^3\mathbf{r}} + O\left(\Delta\epsilon^2\right). \tag{4.39}$$

where $\mathbf{E}(\mathbf{r})$ is the electric field of the unperturbed cavity. In the case where the inclusion consists of an anisotropic medium placed in a region of the cavity originally filled with vacuum, the numerator of Eq. (4.39) becomes

$$\epsilon_0 \int_{\mathcal{V}} (\overleftrightarrow{\chi}_I\,\mathbf{E}) \cdot \mathbf{E}^*\,\mathrm{d}^3\mathbf{r}, \tag{4.40}$$

where $\overleftrightarrow{\chi}_I$ is the susceptibility tensor of the inclusion. Therefore, the only nonzero

contribution to the integral arises from the portion of the volume occupied by the inclusion.

At this stage it is convenient to introduce a quantity that will play a central role in the following analysis and that allows one to characterize the *chiral nature* of the coupling between the cavity field and the FQH liquid. Given an in-plane electric field $\mathbf{E}_{/\!/}(\mathbf{r})$ at the position of the 2DEG, we define the *quadrupolar response density* as

$$\mathcal{R}(\mathbf{r}) \equiv \left(\overleftrightarrow{\chi}_I \cdot \mathbf{E}_{/\!/}(\mathbf{r})\right) \cdot \mathbf{E}^*_{/\!/}(\mathbf{r}), \tag{4.41}$$

which measures the local electromagnetic energy associated with the quadrupolar response of the FQH layer. Since the susceptibility tensor in Eq. (4.23) is gyrotropic, $\mathcal{R}(\mathbf{r})$ is, in general, sensitive to the handedness of the electric-field gradients. Whether this chirality is effectively resolved or averaged out depends entirely on the spatial and phase structure of the cavity field, and will be examined explicitly for the different resonator geometries discussed below.

Before examining some noteworthy practical cases, it is necessary to make one final remark. Equation (4.39) is strictly valid only for media characterized by Hermitian response functions [Cognée et al., 2019], which, as shown in Chapter 2, are associated with the conservation of electromagnetic energy. However, the form of the susceptibility in Eq. (4.23) is in general non-Hermitian and implies the presence of losses, which are encoded in the phenomenological damping parameter γ. In order to highlight the basic mechanism of the graviton–cavity coupling and to obtain simple analytical expressions for the frequency shift and the Rabi splitting, throughout this section we shall first work in the idealized lossless limit $\gamma \to 0^+$, so that the response is effectively Hermitian and Eq. (4.39) can be consistently applied. All frequency shifts reported below are therefore to be understood in this idealized limit.

In realistic FQH systems, however, the graviton mode has a finite linewidth γ, which sets an important constraint on the experimental observability of the effect. In practice, the graviton-induced cavity shift must satisfy the condition

$$|\Delta\omega_c| \gtrsim \gamma \tag{4.42}$$

in order to be spectroscopically resolved. Thus, while the present analysis focuses on the lossless limit to expose the underlying physics, finite losses will ultimately determine the experimental feasibility of graviton detection.

Importantly, we define the graviton resonance frequency as $\Delta_G \equiv \omega_2 - \omega_0$, where the subscript G refers to the graviton excitation. Theoretical predictions place this energy scale in the range of a few tenths of a terahertz [Bacciconi et al., 2025]. It is therefore reasonable to tune the cavity frequency ω_c such that

$$\Delta_G - \omega_c \approx 10^{11}\,\text{Hz}. \tag{4.43}$$

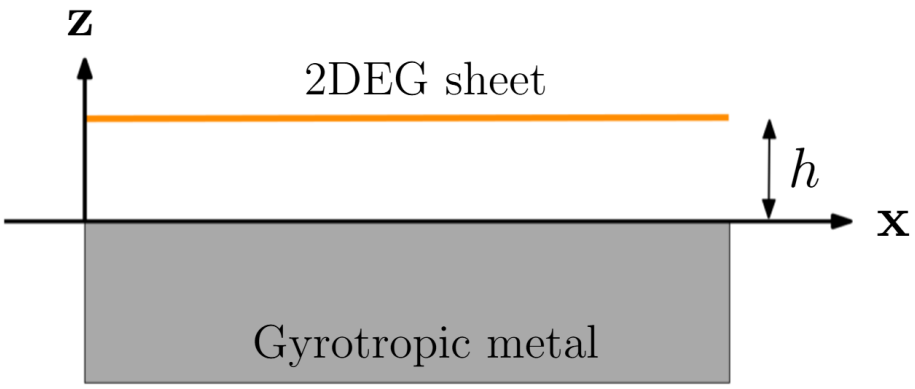

FIGURE 4.4: Outline of the configuration, where the external magnetic field is oriented as $\hat{z}$.

Moreover, for a $\nu = 1/3$ Laughlin liquid, the quantity $\tilde{n}\,|\langle 0|r_+^2|2\rangle|^2$ takes the universal value $l_B^2/6\pi$ [Provenzano et al., 2026]. As a result, one obtains

$$\Lambda(\nu = 1/3) = \frac{e}{48\pi\,\epsilon_0\,B}.$$

For a typical magnetic field strength $B \sim 10\,\mathrm{T}$, this yields the numerical estimate

$$\Lambda(\nu = 1/3) = 1.2 \times 10^{-11}\,\mathrm{m^3 s^{-1}}. \tag{4.44}$$

In all configurations analyzed in the following sections, the graviton-induced frequency shift $\Delta\omega_c$ will be estimated using Eqs. (4.43) and (4.44).

4.4.1 Coupling with magnetoplasmons

Given that very strong magnetic fields are required to observe the effects of the FQH regime in the 2DEG—typically on the order of 10 T—it is natural to expect that such a field also affects the cavity response itself. Indeed, even for a simple isotropic metal or semiconductor subjected to a strong magnetic field, the permittivity becomes anisotropic, exhibiting gyrotropic behavior. If Surface Plasmon–Polaritons (SPPs) can propagate along an interface between vacuum and a metal, when the system is immersed in an external magnetic field these excitations are known as *magnetoplasmons* [Singh and Sarswat, 2023; Pellegrini et al., 2016; Hu, Zhang, and Wang, 2015; Kushwaha, 2001]. Therefore, in this section we shall estimate the frequency shift of the cavity's eigenmode (i.e., the magnetoplasmon) caused by the introduction of the FQH layer at a distance h from the interface between the gyrotropic metal and the vacuum, as shown in Fig. 4.4. The electric-field distribution in this configuration is qualitatively analogous to that shown in Fig. 4.3, given the same metallic behavior of its components.

In the standard case of SPPs at a metal–dielectric interface, only TM-polarized waves can propagate along the interface. When an external magnetic field is applied,

as in the present situation, the polarizations become mixed and can no longer be treated independently. Thus, the magnetic field of a generic surface wave can be written as

$$\mathbf{H}_{\pm} = \left(\mathcal{H}_x, \mathcal{H}_y, \mathcal{H}_z^{\pm}\right) e^{\mp\beta_{\pm} z} e^{i(k_x x - \omega_c t)}, \tag{4.45}$$

where we have chosen $\hat{x}$ as the propagation direction, and the $\pm$ sign refers to the upper half-space $z > 0$, corresponding to vacuum, or to the lower half-space $z < 0$, where the gyrotropic metal is located. The latter is described by the dielectric tensor

$$\boldsymbol{\epsilon}_g = \begin{pmatrix} \epsilon_g(\omega) & ig(\omega) & 0 \\ -ig(\omega) & \epsilon_g(\omega) & 0 \\ 0 & 0 & \epsilon_B(\omega) \end{pmatrix}, \tag{4.46}$$

where $g \propto B$, and in the limit $B \to 0$ the tensor reduces to a matrix proportional to the identity. Since the components ϵ_{ij} of the unperturbed cavity depend on the frequency ω, the denominator in Eq. (4.39) must be modified to account for dispersion. In this case, assuming negligible losses, we may use Brillouin's formula for the electromagnetic energy density in dispersive anisotropic media and generalize the denominator as follows:

$$\int_{\mathcal{V}} \epsilon(\mathbf{r})\, |\mathbf{E}(\mathbf{r})|^2 \, \mathrm{d}^3\mathbf{r} \;\; \to \;\; \int_{\mathcal{V}} \left(\frac{\mathrm{d}}{\mathrm{d}\omega} \Big[\omega\, \boldsymbol{\epsilon}(\mathbf{r}, \omega) \Big] \cdot \mathbf{E} \right)_{\omega=\omega_c} \cdot \mathbf{E}^* \, \mathrm{d}^3\mathbf{r}, \tag{4.47}$$

which ensures that the energy remains positive even when $\epsilon_{ij} < 0$. After some algebra, using the dispersion relations in the two half-spaces, applying the matching conditions, and integrating over z from $-\infty$ to $+\infty$, one obtains the final result:

$$\frac{\Delta\omega_c}{\omega_c} \approx - \left. \frac{\dfrac{\Lambda k_x^2}{2(\Delta_G - \omega_c)} \Big(1 + |\mathcal{A}|^2 + 2\,\mathrm{Im}[\mathcal{A}]\Big)\, e^{-2\beta_+ h}}{\dfrac{1}{\beta_+}(1 + |\mathcal{A}|^2 + |\mathcal{B}|^2) + \dfrac{1}{\beta_-}\left[\dfrac{\mathrm{d}(\omega\epsilon_g)}{\mathrm{d}\omega} + \dfrac{\mathrm{d}(\omega\epsilon_B)}{\mathrm{d}\omega} |\mathcal{B}|^2 - 2\, \dfrac{\mathrm{d}(\omega g)}{\mathrm{d}\omega}\, \mathrm{Im}[\mathcal{A}] \right]} \right|_{\omega=\omega_c} \tag{4.48}$$

where

$$\mathcal{A} \equiv \frac{k_x^2 - \beta_-^2 - \frac{\omega_c^2}{c^2}\epsilon_g}{i\frac{\omega_c^2}{c^2} g}, \qquad \mathcal{B} \equiv \frac{ik_x\beta_-}{\frac{\omega_c^2}{c^2}\epsilon_B}.$$

For typical values of the parameters involved, $h \sim 100\,\mathrm{nm}$, the exponential is practically equal to unity. Therefore, given the result in Eqs. (4.43) and (4.44), it turns out that a good estimate for the shift in energy is on the order of $\Delta\omega_c/\omega_c \approx 10^{-10}$, which is too low to be detected experimentally.

One might wonder whether the graviton–magnetoplasmon coupling could be enhanced by working at larger in-plane wavevectors k_x, since the graviton-induced

susceptibility scales as $k_{/\!/}^2$. However, the effective graviton description adopted in this work is valid only in the long-wavelength regime

$$|\mathbf{k}|\, l_B \ll 1, \tag{4.49}$$

where the graviton emerges as a well-defined neutral spin–2 mode separated from the magnetoroton continuum [Bacciconi et al., 2025]. For $|\mathbf{k}|\, l_B \sim 1$ the graviton hybridizes with higher-energy neutral excitations and the single-mode description breaks down. For this reason, increasing k beyond the long-wavelength regime does not provide a controlled route toward a strong graviton–magnetoplasmon coupling.

Although the resulting frequency shifts in this configuration are too small to be resolved with present experimental capabilities, this setup is conceptually appealing. It represents a completely natural realization of a graviton–photon hybrid system, where the electromagnetic mode is itself gyrotropic due to the external magnetic field. The limitations found here highlight the need for alternative resonator geometries that selectively enhance electric-field gradients at the 2DEG layer. For this reason, in the remainder of this section we focus on electrode-based resonators, which, while less natural from a purely electromagnetic perspective, provide substantially larger and potentially observable graviton-induced frequency shifts.

4.4.2 Two-electrode resonator

Given the small estimated relative frequency shift obtained in the previous section, we now turn to a configuration in which the cavity is formed by two spherical electrodes placed in vacuum. These electrodes determine both the spatial profile and the resonance frequency ω of the electric field throughout the cavity, as shown in Fig. 4.5. We investigate how the insertion of an infinite 2DEG layer, identified with the $z = 0$ plane, modifies the eigenmode frequencies of the system.

More precisely, the two electrodes constitute only the capacitive element of a larger lumped-element LC resonator. The inductive part of the circuit is provided by an external inductor, which fixes the bare cavity frequency ω together with the electrode capacitance. Throughout this section, we assume that the inductive element is not affected by the presence of the 2DEG. As a consequence, the graviton-induced frequency shift $\Delta\omega$ arises solely from the modification of the electric energy stored in the electrode–2DEG geometry.

Outside the electrodes, the electric field is the same as that of two opposite charges $+q$ and $-q$, namely

$$\begin{aligned}\mathbf{E}(\mathbf{r},t) =& \frac{q}{4\pi\epsilon_0}\left(\frac{(x+d)\hat{x}+y\hat{y}+(z-L)\hat{z}}{\left((x+d)^2+y^2+(z-L)^2\right)^{3/2}}\right.\\ &\left.-\frac{(x-d)\hat{x}+y\hat{y}+(z-L)\hat{z}}{\left((x-d)^2+y^2+(z-L)^2\right)^{3/2}}\right)e^{-i\omega_c t},\end{aligned} \tag{4.50}$$

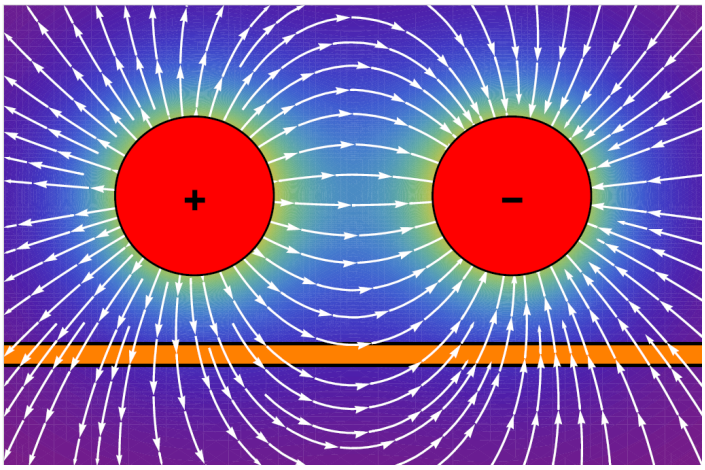

FIGURE 4.5: Instantaneous spatial distribution of the electric field of two spherical electrodes in the xz plane.

where L is the vertical distance between the center of the electrodes and the plane, and $2d$ is the distance between the two centers. The exponential term represents the temporal oscillation of the unperturbed mode. If the electrodes are much smaller than the overall size of the cavity, we can identify the integration volume $\mathcal{V}$ with $\mathbb{R}^3$ in the theoretical estimations. In this case, the integral in Eq. (4.40) becomes

$$\begin{aligned} &\epsilon_0 \int_{\mathbb{R}^3} (\overleftrightarrow{\chi}_I \mathbf{E}) \cdot \mathbf{E}^* \, \mathrm{d}^3\mathbf{r} = \\ &-\frac{\epsilon_0 \Lambda}{\Delta_G - \omega_c} \times \int_{\mathbb{R}^2} \left\{ \begin{pmatrix} 1 & i \\ -i & 1 \end{pmatrix} \cdot \left[\nabla_{/\!/}^2 \mathbf{E}_{/\!/}(z=0) \right] \right\} \cdot \mathbf{E}_{/\!/}^*(z=0) \; \mathrm{d}^2\mathbf{r} = \\ &-\frac{\epsilon_0 \Lambda}{\Delta_G - \omega_c} \left(\frac{q}{4\pi\epsilon_0} \right)^2 \mathcal{I}(d, L), \end{aligned} \tag{4.51}$$

where $\mathbf{E}_{/\!/}(z=0) = (E_x(z=0), E_y(z=0))$ is a two-component vector, the double integral is performed over the plane $z=0$ and $\mathcal{I}(d, L)$ is an integral whose value depends only on the lengths previously defined.

As for the denominator of Eq. (4.39), it is equal to

$$\int_{\mathcal{V}} \epsilon(\mathbf{r}) \, |\mathbf{E}(\mathbf{r})|^2 \, \mathrm{d}^3\mathbf{r} = \frac{q^2}{4\pi\epsilon_0} \left(\frac{1}{R} - \frac{1}{2d} \right), \tag{4.52}$$

where we treated the two electrodes as two spherical surfaces with a uniform surface charge density, i.e. as two spherical shells.[3]

[3] In this case we have not taken into account conductive effects that could be treated using image charges. However, a more refined analysis shows that the electrostatic energy would be higher by a few percent compared to the value reported in Eq. (4.52).

Thus, neglecting higher-order terms, Eq. (4.39) becomes

$$\Delta\omega_c \approx -\frac{\frac{\Lambda\omega_c}{\Delta_G-\omega_c}\,\mathcal{I}(d,L)}{8\pi\left(\frac{1}{R}-\frac{1}{2d}\right)}. \tag{4.53}$$

If $L = d = 10^{-7}\,\mathrm{m}$, then $\mathcal{I} \approx 4.92 \times 10^{28}\,\mathrm{m}^{-4}$. Furthermore, if $R = d/2$ as in the case outlined in Fig. 4.5, the relative frequency shift becomes

$$\frac{\Delta\omega_c}{\omega_c} \approx -\left(1.3 \times 10^{20}\,\mathrm{m}^{-3}\right) \cdot \frac{\Lambda}{\Delta_G-\omega_c}. \tag{4.54}$$

Thus, under the conditions described in Eqs. (4.43) and (4.44), this configuration yields a relative frequency shift of approximately $\Delta\omega_c/\omega_c \approx 1.56 \times 10^{-2}$. Moreover, by suitably tuning ω_c and the separation L between the electrodes and the 2DEG sheet, this ratio can be increased up to values of order 10^{-1}, making the effect experimentally observable.

The key difference between this configuration and the one analyzed in Section 4.4.1 lies in the spatial structure of the electromagnetic fields. In the electrode-based geometry, reducing the distance between the electrodes and the FQH layer enhances the coupling due to the algebraic r^{-2} dependence of the electric field. By contrast, in the interface-based configuration the field decays exponentially away from the interface, so that decreasing the separation only leads to a saturation of the field amplitude. This fundamental difference explains why the coupling strength cannot be substantially improved in the magnetoplasmonic case, whereas it can be significantly enhanced in the electrode-based setup.

We now evaluate the quadrupolar response density $\mathcal{R}(\mathbf{r})$ for the two–electrode configuration introduced above. Despite the intrinsically gyrotropic nature of the 2DEG susceptibility, the electric field generated by two oppositely charged electrodes does not carry a well-defined global chirality. The resulting field gradients contain both left- and right-handed components, which contribute symmetrically to the quadrupolar response.

As a consequence, the quantity

$$\mathcal{R}(\mathbf{r}) = \left(\overleftrightarrow{\chi}_I \cdot \mathbf{E}_{/\!/}(\mathbf{r})\right) \cdot \mathbf{E}^*_{/\!/}(\mathbf{r})$$

is insensitive to the phase pattern of the electrode oscillations. This behavior is illustrated in Fig. 4.6, where reversing the effective chirality of the drive leaves the response unchanged.

Therefore, while the two–electrode resonator yields a sizable graviton-induced frequency shift, it does not allow one to resolve the intrinsic chirality of the graviton mode. This limitation naturally motivates the introduction of resonator geometries with explicitly chiral electromagnetic fields, discussed in the following section.

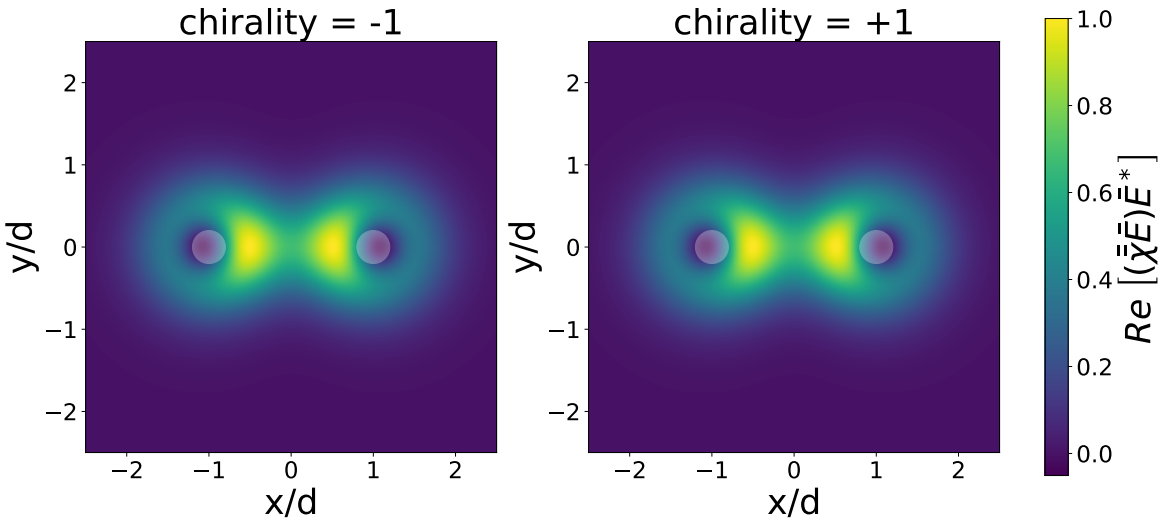

FIGURE 4.6: Quadrupolar response map of an infinite $\nu = 1/3$ FQH layer for a configuration with two point-like electrodes (represented by opaque circles) located at a distance $L = d$ from the FQH plane. The chirality of the electromagnetic excitation is encoded in the relative phases of the oscillating charges. In this geometry, however, the response is insensitive to the choice of chirality, reflecting the absence of chirality resolution in the two–electrode configuration.

4.4.3 Oscillating four–electrode resonator

In order to resolve the intrinsic chirality of the quadrupolar graviton mode, we now consider a resonator geometry that generates an explicitly chiral electromagnetic field at the position of the FQH layer. To this end, we propose a configuration inspired by [Andberger et al., 2024], consisting of four electrodes arranged in a square-like geometry. Such a structure supports two degenerate resonant modes with orthogonal linear polarizations, which can equivalently be interpreted as modes with opposite circular chirality.

Each electrode is modeled as a point charge oscillating as $q_j(t) = q\, e^{-i\omega_c t + is\phi_j}$, where $\phi_j = j\pi/2$ $(j = 0, 1, 2, 3)$ labels the electrode position, and $s = \pm 1$ determines the chirality of the electromagnetic mode. The electrodes are located at positions $(d, 0, L)$, $(0, d, L)$, $(-d, 0, L)$, and $(0, -d, L)$, respectively.

In this geometry, the electric field gradients at the FQH plane possess a well-defined handedness. As a result, the quadrupolar response density in Eq. (4.41) becomes sensitive to the chirality of the cavity mode.

This behavior is illustrated in Fig. 4.7, where the spatial distribution of $\mathcal{R}(\mathbf{r})$ is shown for the two opposite chiralities $s = \pm 1$. The top panels display the quadrupolar response density, while the bottom panels show the corresponding instantaneous electric-field configurations. In contrast to the two–electrode case, reversing the chirality of the drive produces a markedly different response, demonstrating that

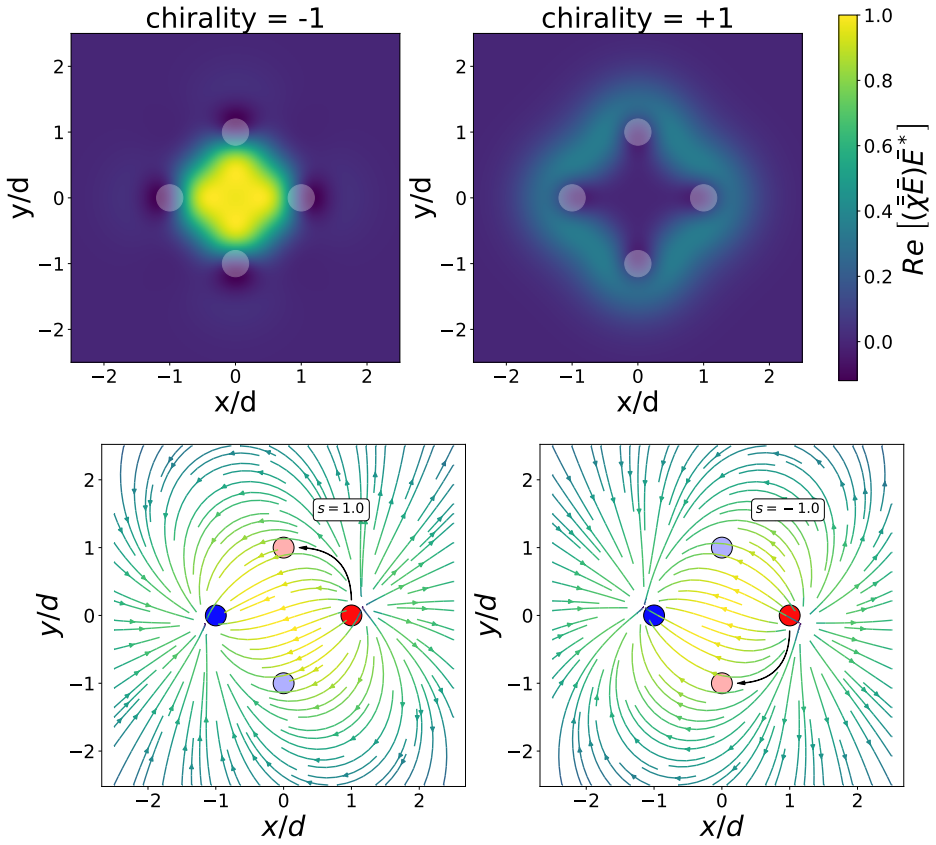

FIGURE 4.7: Top: Quadrupolar response density of a $\nu = 1/3$ FQH layer for a configuration with four point-like electrodes located at a distance $L = d$ from the FQH plane. The chirality of the electromagnetic excitation is encoded in the relative phases of the oscillating charges. Bottom: Instantaneous in-plane electric-field configuration at $\omega_c t = 0.1\,\pi$ for the two opposite chiralities, illustrating the handedness of the field.

this configuration selectively couples to the chiral quadrupolar susceptibility of the FQH graviton mode.

For this resonator geometry, the electric energy stored in the cavity evaluates to

$$\int_{\mathcal{V}} \epsilon(\mathbf{r})\,|\mathbf{E}(\mathbf{r})|^2\,\mathrm{d}^3\mathbf{r} = \frac{q^2}{4\pi\epsilon_0}\left(\frac{2}{R} + \frac{1-2\sqrt{2}}{d}\right), \tag{4.55}$$

leading to the relative frequency shift

$$\frac{\Delta\omega_c}{\omega_c} \approx -\left(2.08\times 10^{20}\,\mathrm{m}^{-3}\right)\frac{\Lambda}{\Delta_G - \omega_c}. \tag{4.56}$$

Under the conditions discussed in Eqs. (4.43) and (4.44), this yields a relative frequency shift of approximately $\Delta\omega_c/\omega_c \approx 2.5\times 10^{-2}$, which is slightly larger than that obtained in the two–electrode configuration and is now associated with a well-defined chirality of the electromagnetic excitation.

4.4.4 Plasmonic Nanoparticle

Finally, as an alternative resonator geometry, we consider a plasmonic nanoparticle placed in the near field of the FQH layer, at a distance d from the plane. The motivation for this configuration is to exploit the strong electric-field gradients associated with localized surface plasmons in order to enhance the quadrupolar graviton–photon coupling.

We model the nanoparticle as a metallic sphere of radius R, described by a Drude-type dielectric function

$$\epsilon(\omega) = \epsilon_\infty \left(1 - \frac{\omega_p^2}{\omega^2}\right), \tag{4.57}$$

embedded in a dielectric medium with permittivity ϵ_d. In the quasi-static limit, the sphere supports a dipolar plasmonic eigenmode whose resonance frequency is determined by the Fröhlich condition [Maier, 2007; Barnes, 2016; Locarno and Brinks, 2023]

$$\epsilon(\omega_c) + 2\epsilon_d = 0 \quad \Rightarrow \quad \omega_c = \omega_p \sqrt{\frac{\epsilon_\infty}{\epsilon_\infty + 2\epsilon_d}}. \tag{4.58}$$

At this frequency, the electromagnetic field is uniform inside the nanoparticle and decays algebraically outside as $|\mathbf{E}| \sim r^{-3}$. This slow spatial decay produces large in-plane field gradients at the position of the FQH layer, as illustrated in Fig. 4.8, making this configuration particularly favorable for quadrupolar coupling.

Following the perturbative approach introduced in Section 4.4, in the configuration shown in Fig. 4.8(a) the graviton-induced frequency shift of the plasmonic resonance can be estimated as

$$\frac{\Delta\omega_c}{\omega_c} = \frac{45}{8}\frac{R^3}{d^6}\frac{\Lambda}{(\Delta_G - \omega_c)\left[\dfrac{\mathrm{d}}{\mathrm{d}\omega}\Big(\omega\,\epsilon(\omega)\Big) + 2\epsilon_d\right]\Big|_{\omega=\omega_c}}. \tag{4.59}$$

In the configuration depicted in Fig. 4.8(b), corresponding to a polarization parallel to the FQH plane, the resulting frequency shift is exactly one half of this value.

This result highlights a key qualitative difference with respect to the magnetoplasmon configuration discussed in Section 4.4.1. Here, the coupling strength scales algebraically as d^{-6}, reflecting the power-law decay of the plasmonic near field. As a consequence, the relative frequency shift can be significantly enhanced by reducing the nanoparticle–2DEG separation.

For realistic parameters in the terahertz regime and submicron separations, the resulting relative frequency shift can reach values of order 10^{-1}, comparable to those obtained for the two- and four-electrode resonators discussed in Sections 4.4.2 and 4.4.3. This makes plasmonic nanostructures another promising platform for the experimental detection of graviton–polaritons in the terahertz domain.

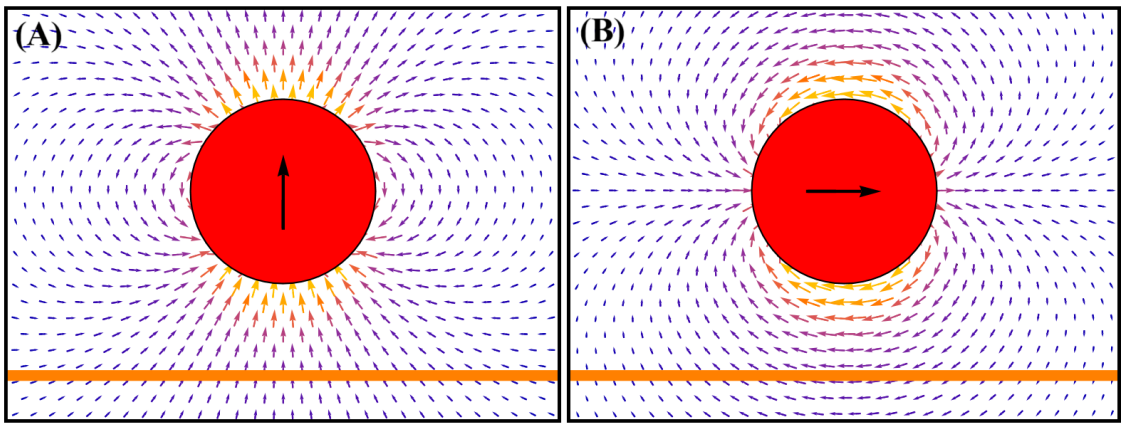

FIGURE 4.8: Schematic representation of the field of a nanoparticle for (a) polarization along $\hat{z}$ and (b) along $\hat{x}$.

4.5 Conclusions

This chapter provides an explicit macroscopic formulation of graviton–polaritons in fractional quantum Hall liquids and identifies concrete electromagnetic signatures that can be accessed with realistic resonator geometries. The main original contribution is the derivation of an effective, quadrupolar electric susceptibility for a 2DEG in the FQH regime, Eq. (4.23), which captures the graviton response as a gyrotropic and spatially dispersive correction to Maxwell's equations. This result places the graviton mode on the same formal footing as surface plasmons and magneto-optical excitations, and makes it possible to treat graviton–photon hybridization using standard electromagnetic tools.

Using this susceptibility, we showed that FQH layers support hybrid surface modes whose electromagnetic structure is essentially plasmonic, despite their microscopic origin being a neutral spin–2 excitation. This establishes that graviton physics is not confined to purely quantum probes, but can leave measurable imprints on classical surface eigenmodes through well-defined modifications of their dispersion and field confinement.

A central quantitative result of this chapter is the evaluation of graviton-induced cavity frequency shifts for different resonator configurations. In magnetoplasmon-based setups, where the electromagnetic mode is itself gyrotropic due to the external magnetic field, the coupling to the graviton is found to be intrinsically weak. Even under favorable assumptions, the resulting relative shifts remain of order 10^{-10} and cannot be significantly enhanced by tuning geometric parameters, because the electromagnetic field amplitude saturates exponentially as the 2DEG approaches the interface. This identifies a fundamental limitation of magnetoplasmon–graviton coupling and shows that this route remains far from any realistic experimental target.

By contrast, electrode-based resonators lead to a qualitatively different scaling. In these configurations, the graviton couples to strongly inhomogeneous near fields with algebraic spatial decay, allowing the relative frequency shift $\Delta\omega_c/\omega_c$ to be

increased by tuning the cavity frequency and the electrode–2DEG separation. Within the regime of validity of the perturbative treatment, the predicted shifts reach the percent level and can be pushed toward values of order 10^{-1}, making the effect in principle observable. This represents, to our knowledge, the first explicit demonstration that graviton–polaritons can produce cavity shifts of experimentally relevant magnitude.

Finally, the four-electrode geometry introduced here constitutes a further step beyond existing proposals, as it allows one to resolve the chirality of the graviton mode itself. While simpler two-electrode resonators already yield sizable shifts, they average over left- and right-handed components of the field. The chiral four-electrode configuration instead couples selectively to the handed quadrupolar response of the FQH liquid, providing a direct electromagnetic probe of graviton chirality.

For completeness, we have also discussed in an alternative plasmonic route Section 4.4.4 based on localized resonances of metallic nanoparticles. While more idealized, this configuration illustrates how strongly confined dipolar near fields can further enhance the graviton–photon coupling and provides a complementary perspective on the scaling of graviton-induced frequency shifts in plasmonic systems.

Taken together, these results show that while graviton–magnetoplasmon coupling remains far from the experimental usefulness, carefully engineered near-field resonators offer a viable and controllable path toward detecting graviton–polaritons and their chiral structure using purely electromagnetic measurements.

Chapter 5

Conclusions and Outlook

5.1 Global Perspective and Narrative of the Thesis

The work presented in this thesis develops a progressive line of thought that starts from classical macroscopic electromagnetism and culminates in the electromagnetic description of graviton–polaritons in fractional quantum Hall liquids. From the outset, the guiding idea has been to build a bridge between apparently distant topics—such as surface plasmon–polaritons, gyrotropic materials, and spin–2 excitations in 2DEGs—by placing them within a single framework based on response functions and symmetries.

A key feature of this thesis is its didactical architecture. The material is intentionally organized so that a reader with a standard background in classical electromagnetism and condensed matter physics can follow a gradual ascent from familiar concepts to more advanced and modern topics. The structure is not simply chronological in terms of the underlying research, but conceptual:

- Chapter 1 introduces electromagnetic surface waves in standard configurations (SPPs, Dyakonov waves, Tamm waves) as a common language and physical motivation.
- Chapter 2 critically reviews the theory of electromagnetic response functions and their classification, placing emphasis on symmetries (time reversal, reciprocity, and energy conservation) and on how they constrain permissible constitutive tensors.
- Chapter 3 applies this framework to the case of gyrotropic and hyperbolic media, showing how their anisotropies combine to generate new nonreciprocal surface waves both at a single interface and in periodic 1D structures.
- Chapter 4 pushes the same logic into the realm of strongly correlated quantum systems, constructing an effective quadrupolar optical response for an FQH liquid and using it to describe a new phenomenon (*graviton–polaritons*) and their possible experimental detection.

In this way, the thesis is also intended as a didactical path: from generic linear response, through the classification of electromagnetic media, to concrete physical

realizations in metamaterials and quantum Hall systems. The same conceptual tools — constitutive tensors, spatial dispersion, gyrotropy, and mode-matching at interfaces — reappear in increasingly sophisticated contexts, allowing the reader to consolidate understanding while encountering more advanced phenomena.

In the following sections, we summarize the main scientific contributions of each chapter and discuss how they fit together into a unified perspective on light–matter interaction in complex media.

5.2 Summary of the Main Scientific Contributions

5.2.1 Electromagnetic response functions and symmetry-based classification

The background conceptual framework is presented in Chapter 2, which provides a systematic and general discussion of response functions in macroscopic electromagnetism. The emphasis is not on any specific material model but rather on the logical organization of constitutive relations and on the role of symmetry principles in constraining them.

Starting from the most general linear relation between fundamental and induction fields, the chapter examines how the three key physical assumptions—time-reversal invariance, Lorentz reciprocity, and energy conservation—restrict the admissible structure of the response tensors. In particular, it introduces a clear and genuinely didactical classification of electromagnetic media into five distinct subsets, based solely on which of these three symmetries they satisfy. Three subsets correspond to media obeying exactly one of the symmetries, one subset contains those satisfying all three simultaneously, and the remaining one includes systems that violate all of them. This organization provides a systematic and physically transparent map of the landscape of electromagnetic media. From the standpoint of the author, this classification is optimal: it is minimal, unambiguous, and avoids common misconceptions that often arise when discussing reciprocity and related concepts.

As an application of the general framework, the final part of the chapter presents two novel electromagnetic configurations—one reciprocal and one nonreciprocal—illustrating how symmetry dictates the allowed propagation of electromagnetic surface waves. In the reciprocal case, propagation occurs in both directions along the interface, whereas in the nonreciprocal configuration it is strictly unidirectional. These examples, treated in a fully self-contained manner, serve as didactical case studies that a reader may use as templates for analyzing other systems.

Overall, Chapter 2 serves a dual purpose:

1. It establishes a *pedagogical ordering of concepts*, beginning from generic linear response and progressively refining it by introducing symmetry constraints and non-Hermitian effects.

2. It introduces and analyzes two new electromagnetic configurations that concretely illustrate how the symmetry-based classification governs surface-wave behavior.

This conceptual foundation is essential for the remainder of the thesis. Both the gyro–hyperbolic structures studied in Chapter 3 and the graviton–polariton system developed in Chapter 4 are interpreted through the lens of this classification of media and their response functions.

As an additional original contribution, Appendix A includes a brief but instructive discussion of the connection between the two formal approaches most commonly used in the literature on electrodynamics in continuous media. The discussion is carried out in the most general setting of bianisotropic materials and extends the analysis presented in [Agranovich and Gartstein, 2009].

5.2.2 Gyro–hyperbolic surface waves and photonic crystals

Chapter 3 is devoted to surface waves and bulk modes in systems combining gyrotropic and hyperbolic media. Building on the symmetry-based classification of Chapter 2, this chapter provides explicit examples of how the two kinds of anisotropy are woven together in realistic structures to produce nonreciprocal propagation and exotic mode profiles.

The first part of Chapter 3 considers a single interface between a gyroelectric medium (in a Voigt configuration) and a uniaxial material. When the uniaxial material is tuned into a hyperbolic regime, the interface supports surface modes with several distinctive properties:

- TE and TM modes still decouple, but only TM-polarized waves can form surface states under the assumed conditions. The dispersion relations for the evanescent components are derived analytically, and the conditions for their existence are made fully explicit.

- The presence of gyrotropy, encoded in the off-diagonal parameter g of the dielectric tensor, splits the forward and backward branches of the dispersion relation, leading to non-degenerate modes with opposite propagation directions — a clear manifestation of nonreciprocity in the sense of Chapter 2.

- The anisotropy of the hyperbolic medium induces a *tilt* in the electric-field lines on the anisotropic side, akin to the profile of Zenneck waves, even in the absence of material losses. This geometrical structure of the fields is analyzed analytically and numerically, highlighting the role of the off-diagonal component ϵ_{yz}.

- The Poynting vector is computed in closed form, and the conditions under which the group velocity can become negative (backward waves) are identified. This connects the sign of the group velocity to the interplay between gyrotropy, anisotropy, and surface confinement.

The chapter then moves to experimentally relevant platforms by proposing an interface consisting of indium antimonide (InSb) under a static magnetic field and a graphene-based asymmetric hyperbolic metamaterial (AHMM). Using realistic dispersions for InSb and for layered graphene structures, the chapter shows:

- How the surface mode can be excited in an Otto configuration using a high-index prism.
- That the reflectivity spectra of such a structure are strongly asymmetric with respect to the sign of the incidence angle, in direct correspondence with the nonreciprocal dispersion.
- That, despite the presence of losses in realistic materials, the surface mode retains a propagation length substantially larger than its wavelength, making experimental detection feasible.

The second part of Chapter 3 extends the analysis to one-dimensional photonic crystals composed of alternating gyroelectric and uniaxial layers. Among the main results:

- A general expression for the Bloch wave number K_B for TM modes is derived, highlighting how gyrotropy and anisotropy enter through a compact parameter Z and how they modify the photonic band structure.
- When the uniaxial layers are in a hyperbolic regime, the crystal supports *intermediate surface waves* within the band gaps separating bulk bands. Depending on the relative values of the plasma frequencies $\omega_{p,\perp}$ and $\omega_{p,\parallel}$, these intermediate modes can have either positive or negative group velocity (forward or backward propagation).
- The field distributions of these new modes are shown to have significantly larger penetration depths than conventional Tamm waves, suggesting that they can mediate energy transport via surface channels rather than bulk propagation.
- Gyrotropy is shown to deform the bulk bands in a controllable way, enabling magnetic tuning of the photonic band structure and, consequently, of the allowed frequency ranges for both bulk and surface modes.
- Finite-size structures are analyzed using the Berreman formalism, and the Goos–Hänchen shift is computed, revealing large positive or negative lateral shifts correlated with the excitation of forward or backward surface modes.

From a pedagogical viewpoint, Chapter 3 illustrates the full "life cycle" of a surface mode: from the analytic derivation at a simple interface, to its embedding in a realistic material platform, its evolution in a periodic structure, and its signature in measurable quantities (reflectivity, GHS) in finite systems. It thus serves as a comprehensive example of how the classification of media in Chapter 2 translates into concrete structures.

5.2.3 Quadrupolar optics and graviton–polaritons in FQH liquids

Chapter 4 extends the response–function viewpoint of this thesis to a strongly correlated quantum fluid: a two-dimensional electron gas in the fractional quantum Hall (FQH) regime, where the relevant neutral excitation at long wavelength is a chiral spin–2 "graviton" mode. The chapter shows how this microscopic geometric excitation can be encoded in a macroscopic electromagnetic response and how it hybridizes with cavity fields to form graviton–polaritons.

The first main result is the derivation of an effective electric susceptibility for a strictly two-dimensional system whose low-energy optical response is dominated by a single quadrupolar transition with angular momentum $L_z = -2$. In the long-wavelength limit this leads to a sheet susceptibility of the form

$$\overleftrightarrow{\chi}(\omega, \mathbf{k}) = \frac{\tilde{n} q^2}{8\,\epsilon_0\,\hbar}\,\frac{|\langle 0|r_+^2|2\rangle|^2\,k_{/\!/}^2}{\omega_2 - \omega_0 - \omega - i\gamma}\begin{pmatrix} 1 & i \\ -i & 1 \end{pmatrix}\delta(z)$$

which is simultaneously gyrotropic and temporally and spatially dispersive. This structure encapsulates, in a compact macroscopic tensor, the chiral quadrupole character of the FQH graviton and the fact that only electric fields with strong in-plane gradients can efficiently excite it. In this way, a microscopic spin–2 mode in a quantum Hall liquid is recast as an effective nonlocal, gyrotropic medium in the language of macroscopic electrodynamics.

From this susceptibility, the chapter extracts a surface conductivity tensor for the FQH layer and uses it to determine the electromagnetic surface eigenmodes supported by different geometries. A general dispersion relation is derived for hybrid surface waves at the interface between two arbitrarily anisotropic conducting sheets, and in the single-sheet limit it reduces to Eq. (4.38), where TE and TM fields are unavoidably mixed by the off-diagonal gyrotropic response. Applying this formalism to a 2DEG in the FQH regime (described by the quadrupolar conductivity of Eq. (4.29)) and to a parallel graphene sheet with gyrotropic Drude conductivity, the thesis identifies magnetoplasmon–like surface modes with strong subwavelength confinement whose field profiles match those expected for plasmonic structures, but now enriched by the chiral, quadrupolar physics of the graviton.

The second main contribution of Chapter 4 is a quantitative study of how this graviton-induced response modifies the eigenfrequencies of electromagnetic resonators. Using a perturbative cavity-shift formula adapted to anisotropic, possibly dispersive media, the chapter evaluates the relative frequency shift $\Delta\omega_c/\omega_c$ for several architectures that place the FQH layer in tailored electric-field environments. A magnetoplasmonic configuration, in which the 2DEG is coupled to a gyrotropic metal supporting surface magnetoplasmons, is shown to produce shifts well below current experimental sensitivity and not improvable within the controlled long-wavelength regime. In contrast, electrode-based resonators and plasmonic inclusions provide much stronger gradients: for a two-electrode LC resonator and for a nearby

plasmonic nanoparticle tuned in the terahertz range, the same framework predicts graviton-induced shifts of order 10^{-2} or larger for $\nu = 1/3$ and achievable values of B, bringing the effect into a regime that is, in principle, experimentally accessible.

Finally, the chapter introduces a four-electrode chiral resonator designed to probe directly the handedness of the graviton mode. By driving four electrodes with phase shifts that implement $s = \pm 1$ chiral cavity modes, and evaluating the quadrupolar response density $(\overleftrightarrow{\chi}\ \mathbf{E}) \cdot \mathbf{E}$ on the 2DEG plane, the chapter demonstrates that the 2DEG layer responds differently to opposite chiral drives and that this configuration yields a relative frequency shift slightly larger than in the two-electrode case. This provides a concrete electromagnetic signature of the graviton chirality and a realistic route to distinguishing its coupling to left- and right-handed cavity excitations.

Altogether, Chapter 4 shows that graviton–polaritons in FQH liquids can be captured by a well-defined nonlocal susceptibility, embedded into Maxwell's equations, and that suitably engineered resonator geometries—especially multi-electrode and plasmonic structures—can convert this geometric quantum response into measurable shifts of cavity spectra.

5.3 Outlook and Future Research Directions

The results obtained in this thesis naturally suggest a number of future research directions, both on the side of classical photonics and on the side of strongly correlated quantum systems.

Gyro–hyperbolic photonics and nonreciprocal devices

On the classical side, gyro–hyperbolic structures of the kind analyzed in Chapter 3 offer a versatile platform for nonreciprocal photonic functionalities in the terahertz and mid-infrared regimes. Several directions for future development naturally emerge:

- **Nonreciprocal surface-waveguides.** The strong asymmetry of the dispersion relations obtained in Chapter 3 can be exploited to design unidirectional surface-wave channels, either along simple anisotropic interfaces or on the boundaries of periodic structures, enabling robust edge transport.

- **Magnetically tunable sensors.** Because gyrotropy modifies both the photonic bands and the position of surface branches, small variations of the external magnetic field can induce large changes in reflectivity, phase response, or the Goos–Hänchen shift. This sensitivity suggests applications in THz sensing, where high tunability and directional selectivity are desirable.

- **Total-reflector regimes.** The identification of parameter ranges in which a one-dimensional gyro–hyperbolic photonic crystal behaves as a *total reflector*—exhibiting unity reflectivity for all incidence angles and for a broad frequency window, even in the absence of material losses—opens an especially intriguing direction. This phenomenon indicates that multilayered anisotropic stacks can be engineered to suppress every bulk channel while simultaneously eliminating leakage through surface modes, effectively creating a lossless, broadband mirror with nonreciprocal features.

The analytical tools developed in Chapter 3, together with the emergence of intermediate surface waves characterized by unusually large penetration depths, provide a solid foundation for such device-oriented investigations. In particular, these modes demonstrate that information and energy can be guided *via surface-wave channels rather than bulk bands*, offering an alternative mechanism for signal transport in anisotropic photonic architectures.

Graviton–polaritons and quantum geometry

The study of graviton–polaritons is still in its infancy, and the results of Chapter 4 highlight only the first steps toward a broader electromagnetic theory of quantum geometry. Much remains to be explored, both on the quantum side and on the electrodynamic implementation side. Several promising avenues naturally emerge:

- **Beyond a single quadrupolar mode.** The susceptibility obtained in Chapter 4 captures the dominant long-wavelength quadrupolar transition. A natural next step is to incorporate additional neutral excitations, such as edge excitations and effects of Landau-level mixing. This analysis may uncover additional polaritonic branches and clarify the role of geometric degrees of freedom at finite momentum.

- **Toward experimental realization.** The electrode–based resonators and plasmonic nanoparticle configurations analyzed in Chapter 4 identify concrete electromagnetic environments in which graviton–polariton coupling produces frequency shifts of experimentally relevant magnitude. A natural continuation of this work is the search for suitable material platforms and cavity architectures capable of maximizing the quadrupolar interaction to reach the strong coupling regime. This perspective builds directly on the broader trajectory of the current research, which evolved from the study of electromagnetic waves in hyperbolic and gyrotropic media to the formulation of a macroscopic, anisotropic susceptibility for FQH graviton modes. With this susceptibility now available, one can systematically design and test resonator geometries—such as multi–electrode structures or plasmonic cavities—that enhance the appropriate field gradients and selectively address the chiral nature of the excitation. A detailed experimental–feasibility analysis, combining full-wave simulations, realistic material

parameters and THz spectroscopy constraints, naturally emerges as the next step and forms the foundation for a dedicated publication, especially in view of ongoing discussions with experimental groups interested in implementing graviton–polariton detection.

5.4 Final Remarks

This thesis has followed a continuous line of reasoning: starting from the general structure of electromagnetic response functions and their classification according to symmetry (Chapter 2), it has moved through classical examples of surface waves in gyrotropic and hyperbolic media (Chapter 3), and finally reached the realm of strongly correlated quantum matter, where graviton excitations and quadrupolar optics emerge (Chapter 4). Throughout this journey, the same conceptual tools have been used to understand increasingly sophisticated systems.

From a physical standpoint, the main message is that many seemingly exotic phenomena — nonreciprocal surface waves, backward modes, chiral spin–2 excitations — can be captured and unified within the framework of macroscopic electrodynamics, provided that one is willing to embrace the full tensorial and nonlocal structure of the electromagnetic response. From a didactical standpoint, the thesis aims to provide a clear route through this landscape, so that future readers and researchers can use the same logic to explore new systems and propose new experiments.

Appendix A

From EBDH approach to EBD approach

Let us start from Maxwell's equations, written in their standard macroscopic form as

$$\begin{cases} \nabla \cdot \mathbf{D} = \rho_{\mathrm{e}} + \rho_{\mathrm{f}}, \\ \nabla \cdot \mathbf{B} = 0, \\ \nabla \times \mathbf{E} = -\dfrac{\partial \mathbf{B}}{\partial t}, \\ \nabla \times \mathbf{H} = \mathbf{J}_{\mathrm{e}} + \mathbf{J}_{\mathrm{f}} + \dfrac{\partial \mathbf{D}}{\partial t}. \end{cases} \tag{A.1}$$

In electrodynamics, the splitting of induced currents into magnetization and polarization parts is not unique. In fact, the constitutive relations

$$\begin{aligned} \mathbf{D} &= \epsilon_0 \mathbf{E} + \mathbf{P}, \\ \mathbf{H} &= \mu_0^{-1} \mathbf{B} - \mathbf{M} \end{aligned}$$

imply that Maxwell's equations are invariant under the following transformations:

$$\begin{aligned} \mathbf{P} &\longrightarrow \mathbf{P} + \nabla \times \mathbf{W}, \\ \mathbf{M} &\longrightarrow \mathbf{M} - \frac{\partial \mathbf{W}}{\partial t}, \end{aligned}$$

where $\mathbf{W}$ is an arbitrary vector function $\mathbf{W} \in \mathcal{C}^2(\mathbb{R}^4)$ of space and time. This means that $\mathbf{D}$ and $\mathbf{H}$ are not uniquely defined either, and vary according to the specific choice of $\mathbf{W}$. Although the field equations themselves are invariant under these transformations, the boundary conditions are not, and therefore must be transformed consistently.

Keeping this in mind, let us consider the general constitutive equations in the *Post* formalism:

$$\begin{aligned} \mathbf{D} &= \boldsymbol{\epsilon} \cdot \mathbf{E} + \boldsymbol{\xi} \cdot \mathbf{B}, \\ \mathbf{H} &= \boldsymbol{\zeta} \cdot \mathbf{E} + \boldsymbol{\mu}^{-1} \cdot \mathbf{B}, \end{aligned} \tag{A.2}$$

where $(\mathbf{E}, \mathbf{B})$ are treated as the fundamental field variables. Equations (A.1)–(A.2) define the so-called *EBDH* approach, in which all four fields are considered simultaneously. The aim of this section is to establish a connection with the *EBD* approach,

commonly used in the Russian literature.

Consider the curl equation for $\mathbf{H}$,

$$\nabla \times \mathbf{H} = \mathbf{J}_\mathrm{e} + \mathbf{J}_\mathrm{f} + \frac{\partial \mathbf{D}}{\partial t}. \tag{A.3}$$

Let us introduce the quantity

$$\left(\mathbf{I} - \mu_0 \boldsymbol{\mu}^{-1}\right) \frac{\mathbf{B}}{\mu_0} - \boldsymbol{\zeta} \cdot \mathbf{E}.$$

It has the same dimensions as $\mathbf{H}$, so its curl can be added to both sides of Eq. (A.3) without any physical change:

$$\begin{aligned} \nabla \times \underbrace{\left[\mathbf{H} + \left(\mathbf{I} - \mu_0 \boldsymbol{\mu}^{-1}\right) \frac{\mathbf{B}}{\mu_0} - \boldsymbol{\zeta} \cdot \mathbf{E}\right]}_{= \frac{\mathbf{B}}{\mu_0}, \text{ from Eq. (A.2)}} \\ = \mathbf{J}_\mathrm{e} + \mathbf{J}_\mathrm{f} + \frac{\partial \mathbf{D}}{\partial t} + \nabla \times \left[\left(\mathbf{I} - \mu_0 \boldsymbol{\mu}^{-1}\right) \frac{\mathbf{B}}{\mu_0} - \boldsymbol{\zeta} \cdot \mathbf{E}\right]. \end{aligned}$$

We now move to oscillating electromagnetic fields, for which $\partial_t \to -i\omega$. This makes the right-hand side of Eq. (A.3) become

$$\mathbf{J}_\mathrm{e} + \mathbf{J}_\mathrm{f} - i\omega\, \mathbf{D} + \nabla \times \left[\left(\mathbf{I} - \mu_0 \boldsymbol{\mu}^{-1}\right) \frac{\mathbf{B}}{\mu_0} - \boldsymbol{\zeta} \cdot \mathbf{E}\right].$$

This motivates the definition of a new, effective displacement field:

$$\mathbf{D} \equiv \mathbf{D} + \frac{i}{\omega} \nabla \times \left[\left(\mathbf{I} - \mu_0 \boldsymbol{\mu}^{-1}\right) \frac{\mathbf{B}}{\mu_0} - \boldsymbol{\zeta} \cdot \mathbf{E}\right], \tag{A.4}$$

whose divergence equals that of $\mathbf{D}$, since their difference is the curl of a vector field. Therefore, Maxwell's equations for the new induced fields take the form

$$\begin{cases} \nabla \cdot \mathbf{D} = \rho_\mathrm{e} + \rho_\mathrm{f}, \\ \nabla \cdot \mathbf{B} = 0, \\ \nabla \times \mathbf{E} = i\omega\, \mathbf{B}, \\ \nabla \times \dfrac{\mathbf{B}}{\mu_0} = \mathbf{J}_\mathrm{e} + \mathbf{J}_\mathrm{f} - i\omega\, \mathbf{D}, \end{cases} \tag{A.5}$$

where the dependence on $\mathbf{H}$ has disappeared. This procedure thus leads to a fully

equivalent representation of Maxwell's equations,[1] in which **B** entirely replaces **H** as the magnetic field variable — hence the name *EBD* — while the new displacement field **D** collects all magnetic and magnetoelectric corrections through the four response tensors:

$$\begin{aligned}\mathbf{D} \;\equiv\; \boldsymbol{\epsilon}_{\text{eff}}\cdot\mathbf{E} &= \mathbf{D} + \frac{i}{\omega}\nabla\times\left[\left(\mathbf{I}-\mu_0\boldsymbol{\mu}^{-1}\right)\frac{\nabla\times\mathbf{E}}{i\mu_0\omega} - \boldsymbol{\zeta}\cdot\mathbf{E}\right] \\ &= \boldsymbol{\epsilon}\cdot\mathbf{E} + \frac{1}{i\omega}\boldsymbol{\xi}\cdot(\nabla\times\mathbf{E}) + \frac{i}{\omega}\nabla\times\left[\left(\mathbf{I}-\mu_0\boldsymbol{\mu}^{-1}\right)\frac{\nabla\times\mathbf{E}}{i\mu_0\omega} - \boldsymbol{\zeta}\cdot\mathbf{E}\right].\end{aligned}$$

Hence, the response of the system can be entirely summarized by the effective dielectric tensor $\boldsymbol{\epsilon}_{\text{eff}}$, which, however, depends on the spatial derivatives — or equivalently, in the case of electromagnetic waves, on the components of the wave vector. This artificial introduction of spatial dispersion implies that both the field boundary conditions and the form of the Poynting vector must be reformulated accordingly, which is generally a non-trivial task [Semchenko, Tretyakov, and Serdyukov, 1996; Serdyukov et al., 2001b].

As a limiting case, for the propagation of electromagnetic waves in simple isotropic media, the effective dielectric tensor reduces to

$$\epsilon_{\text{eff},ij}(\omega,\mathbf{k}) = \epsilon_\perp(\omega,k)\left[\delta_{ij} - \frac{k_i k_j}{k^2}\right] + \epsilon_\parallel(\omega,k)\frac{k_i k_j}{k^2},$$

where

$$\epsilon_\perp = \epsilon(\omega), \qquad \epsilon_\parallel = \epsilon(\omega) + \left(\frac{1}{\mu_0} - \frac{1}{\mu}\right)\frac{k^2}{\omega^2},$$

as described and used in Refs. [Landau and Lifshitz, 1984; Agranovich and Ginzburg, 1984; Agranovich and Gartstein, 2009; Toptygin, 2015].

[1] In this case, the vector **W** that allows one to move from one approach to the other is given by

$$\mathbf{W} = \frac{i}{\omega}\left[\left(\mathbf{I}-\mu_0\boldsymbol{\mu}^{-1}\right)\frac{\mathbf{B}}{\mu_0} - \boldsymbol{\zeta}\cdot\mathbf{E}\right].$$

Appendix B

Interface Conditions

Given H_x in Eq. (3.29), it is trivial to evaluate E_y and E_z using Maxwell's equations. Additionally, they imply that H_x and E_y are continuous functions along the boundaries, whereas E_z is not, due to the discontinuity of the dielectric function. The continuity of both H_x and E_y on the boundaries on the two boundaries marked by red arrows in Fig. 3.5(b) leads to

$$c_{m-1} + d_{m-1} = a_m e^{ik_g L} + b_m e^{-ik_g L}, \tag{B.1}$$

$$c_m e^{ik_u d_u} + d_m e^{-ik_u d_u} = a_m e^{ik_g d_u} + b_m e^{-ik_g d_u}, \tag{B.2}$$

$$\begin{aligned} &\frac{i\epsilon_v}{\epsilon_\parallel \epsilon_\perp}\left[d_{m-1}(\epsilon_{zz}k_u + \epsilon_{zz}k_y) + c_{m-1}(\epsilon_{zz}k_y - \epsilon_{zz}k_u)\right] = \\ &= a_m\left(ik_g - \frac{g}{\epsilon_g}k_y\right)e^{ik_g L} - b_m\left(ik_g + \frac{g}{\epsilon_g}k_y\right)e^{-ik_g L}, \end{aligned} \tag{B.3}$$

$$\begin{aligned} &\frac{i\epsilon_v e^{ik_u d_u}}{\epsilon_\parallel \epsilon_\perp}\left[c_m(\epsilon_{zz}k_u + \epsilon_{yz}k_y) + d_m(\epsilon_{yz}k_y - \epsilon_{zz}k_u)e^{-2ik_u d_u}\right] = \\ &= a_m\left(ik_g - \frac{g}{\epsilon_g}k_y\right)e^{ik_g d_u} - b_m\left(ik_g + \frac{g}{\epsilon_g}k_y\right)e^{-ik_g d_u}, \end{aligned} \tag{B.4}$$

where we defined

$$\epsilon_v \equiv \frac{\epsilon_g^2 - g^2}{\epsilon_g}.$$

The components of the wave vectors obey the following dispersion relations:

$$\epsilon_{yy}k_y^2 + \epsilon_{zz}k_u^2 + 2k_y k_u \epsilon_{yz} = \frac{\omega^2}{c^2}\epsilon_\parallel \epsilon_\perp.$$

$$k_g^2 + k_y^2 = \epsilon_v \frac{\omega^2}{c^2}.$$

Let us use a_m and b_m as free variables and recast the system in Eqs. (B.1) to (B.4) into the following form

$$\begin{pmatrix} c_{m-1} \\ d_{m-1} \end{pmatrix} = \mathbf{P}^{-1}\mathbf{Q} \begin{pmatrix} a_m \\ b_m \end{pmatrix}, \quad \begin{pmatrix} c_m \\ d_m \end{pmatrix} = \mathbf{R}^{-1}\mathbf{S} \begin{pmatrix} a_m \\ b_m \end{pmatrix},$$

where $\mathbf{P}, \mathbf{Q}, \mathbf{R}, \mathbf{S}$ are 2×2 matrices [Yeh, 2005]. The last two equations imply

$$\begin{pmatrix} c_{m-1} \\ d_{m-1} \end{pmatrix} = \mathbf{P}^{-1}\mathbf{Q}\,\mathbf{S}^{-1}\mathbf{R} \begin{pmatrix} c_m \\ d_m \end{pmatrix}. \tag{B.5}$$

The matrix

$$\mathbf{P}^{-1}\mathbf{Q}\,\mathbf{S}^{-1}\mathbf{R} \equiv \begin{pmatrix} A & B \\ C & D \end{pmatrix}$$

is unimodular because it relates the field amplitudes of equivalent layers of two consecutive cells [Yariv and Yeh, 2002; Yeh, 2005].

Appendix C

Derivation of the Matrix Equation and Dispersion Relation

Referring to Fig. 4.1, the dispersion relation in each bulk is

$$k_x^2 + k_{mz}^2 = \epsilon_m \frac{\omega^2}{c^2}, \tag{C.1}$$

where $m = 1, 2, 3$ is the index that characterizes the medium and each ϵ_m have no dimension. Since all bulk media are isotropic, Maxwell's equations become

$$\begin{aligned} \mathbf{k}_m \cdot \mathbf{E}_m &= 0, \\ \mathbf{k}_m \cdot \mathbf{B}_m &= 0, \\ \mathbf{k}_m \times \mathbf{E}_m &= \omega \mathbf{B}_m, \\ \mathbf{k}_m \times \mathbf{B}_m &= -\frac{\omega}{c^2} \epsilon_m \mathbf{E}_m. \end{aligned}$$

From the third equation we obtain

$$\mathbf{B}_m = \frac{1}{\omega} \mathbf{k}_m \times \mathbf{E}_m = \frac{1}{\omega} \begin{pmatrix} -k_{mz} E_{my} \\ k_{mz} E_{mx} - k_x E_{mz} \\ k_x E_{my} \end{pmatrix} e^{i(k_x x - \omega t)}. \tag{C.2}$$

In this configuration, the continuity of B_z at the interface is equivalent to that of E_y. Recalling that

$$\mathbf{k}_m \cdot \mathbf{E}_m = 0 \qquad \Longrightarrow \qquad k_x E_{mx} + k_{mz} E_{mz} = 0, \tag{C.3}$$

a better expression for the y component of the magnetic field is found, which, apart from the exponential factor, becomes

$$B_{my} = \frac{1}{\omega} \left(k_{mz} E_{mx} - k_x E_{mz} \right) = \frac{1}{\omega} \left(k_{mz} E_{mx} + \frac{k_x^2}{k_{mz}} E_{mx} \right) = \frac{\omega \, \epsilon_m}{c^2 k_{mz}} E_{mx}. \tag{C.4}$$

Taking into account that the k_z associated with the backward propagating mode in medium 2 should be written with the negative sign, after some algebra we find:

$$\mathbf{B}_1(z) = \frac{1}{\omega}\left(-k_{1z}\,\mathcal{E}_y^1,\ \frac{\omega^2\epsilon_1}{c^2 k_{1z}}\,\mathcal{E}_x^1,\ k_x\,\mathcal{E}_y^1 \right) e^{ik_{1z}z},$$

$$\begin{aligned}\mathbf{B}_2(z) = \frac{1}{\omega}\Bigg(& -k_{2z}\,\mathcal{E}_y^{2+}e^{ik_{2z}z} + k_{2z}\,\mathcal{E}_y^{2-}e^{-ik_{2z}z}, \\ & \frac{\omega^2\epsilon_2}{c^2 k_{2z}}\,\mathcal{E}_x^{2+}e^{ik_{2z}z} - \frac{\omega^2\epsilon_2}{c^2 k_{2z}}\,\mathcal{E}_x^{2-}e^{-ik_{2z}z}, \\ & k_x\,\mathcal{E}_y^{2+}e^{ik_{2z}z} + k_x\,\mathcal{E}_y^{2-}e^{-ik_{2z}z} \Bigg),\end{aligned}$$

$$\mathbf{B}_3(z) = \frac{1}{\omega}\left(-k_{3z}\,\mathcal{E}_y^3,\ \frac{\omega^2\epsilon_3}{c^2 k_{3z}}\,\mathcal{E}_x^3,\ k_x\,\mathcal{E}_y^3 \right) e^{ik_{3z}z}.$$

The eight continuity conditions at the interfaces $z = 0$ and $z = d$ are

$$\begin{aligned}\mathbf{E}_{1,\parallel}(z=d) - \mathbf{E}_{2,\parallel}(z=d) &= 0, \\ \mathbf{E}_{2,\parallel}(z=0) - \mathbf{E}_{3,\parallel}(z=0) &= 0, \\ \mathbf{B}_{1,\parallel}(z=d) - \mathbf{B}_{2,\parallel}(z=d) &= \mu_0 \mathcal{S}(z=d)\times\hat{n}, \\ \mathbf{B}_{2,\parallel}(z=0) - \mathbf{B}_{3,\parallel}(z=0) &= \mu_0 \mathcal{S}(z=0)\times\hat{n},\end{aligned}$$

where the symbol $\parallel$ denotes the components along the interfaces, i.e., x and y, $\hat{n}$ is directed as $\hat{z}$, and $\mathcal{S}$ is the surface current given by

$$\begin{aligned}\mathcal{S}(z=d) &= \overleftrightarrow{\sigma}_R\ \mathbf{E}_\parallel(z=d), \\ \mathcal{S}(z=0) &= \overleftrightarrow{\sigma}_L\ \mathbf{E}_\parallel(z=0).\end{aligned}$$

Here, both $\mathcal{S}$ and $\mathbf{E}_\parallel$ are two-component vectors, and the conductivity tensors are

$$\overleftrightarrow{\sigma}_{R/L} = \begin{pmatrix} \sigma_{xx}^{R/L} & \sigma_{xy}^{R/L} \\ \sigma_{yx}^{R/L} & \sigma_{yy}^{R/L} \end{pmatrix}. \tag{C.5}$$

It does not matter which medium index is used for $\mathbf{E}_\parallel$ at the interface, because the tangential electric field is continuous by construction. After some algebra, we obtain the following system:

$$\begin{aligned} -\mathcal{E}_x^1\,e^{-\beta_1 d} + \mathcal{E}_x^{2+}\,e^{\beta_2 d} + \mathcal{E}_x^{2-}\,e^{-\beta_2 d} &= 0, \\ -\mathcal{E}_y^1\,e^{-\beta_1 d} + \mathcal{E}_y^{2+}\,e^{\beta_2 d} + \mathcal{E}_y^{2-}\,e^{-\beta_2 d} &= 0, \\ \mathcal{E}_x^{2+} + \mathcal{E}_x^{2-} - \mathcal{E}_x^3 &= 0, \\ \mathcal{E}_y^{2+} + \mathcal{E}_y^{2-} - \mathcal{E}_y^3 &= 0,\end{aligned}$$

$$\begin{aligned}
\beta_1\,\mathcal{E}_y^1\,e^{-\beta_1 d} + \beta_2\,\mathcal{E}_y^{2+}\,e^{\beta_2 d} - \beta_2\,\mathcal{E}_y^{2-}\,e^{-\beta_2 d} \\
-i\mu_0\omega\left(\sigma_{yx}^R\,\mathcal{E}_x^1\,e^{-\beta_1 d} + \sigma_{yy}^R\,\mathcal{E}_y^1\,e^{-\beta_1 d}\right) = 0, \\
-\beta_2\,\mathcal{E}_y^{2+} + \beta_2\,\mathcal{E}_y^{2-} + \beta_3\,\mathcal{E}_y^3 - i\mu_0\omega\left(\sigma_{yx}^L\,\mathcal{E}_x^3 + \sigma_{yy}^L\,\mathcal{E}_y^3\right) = 0, \\
\frac{\epsilon_1}{\beta_1}\,\mathcal{E}_x^1\,e^{-\beta_1 d} + \frac{\epsilon_2}{\beta_2}\,\mathcal{E}_x^{2+}\,e^{\beta_2 d} - \frac{\epsilon_2}{\beta_2}\,\mathcal{E}_x^{2-}\,e^{-\beta_2 d} \\
+\frac{i}{\epsilon_0\,\omega}\left(\sigma_{xx}^R\,\mathcal{E}_x^1\,e^{-\beta_1 d} + \sigma_{xy}^R\,\mathcal{E}_y^1\,e^{-\beta_1 d}\right) = 0, \\
-\frac{\epsilon_2}{\beta_2}\,\mathcal{E}_x^{2+} + \frac{\epsilon_2}{\beta_2}\,\mathcal{E}_x^{2-} + \frac{\epsilon_3}{\beta_3}\,\mathcal{E}_x^3 + \frac{i}{\epsilon_0\,\omega}\left(\sigma_{xx}^L\,\mathcal{E}_x^3 + \sigma_{xy}^L\,\mathcal{E}_y^3\right) = 0,
\end{aligned}$$

where we have used the following notation:

$$k_{1z} = +\,i\,\beta_1 \equiv +\,i\,\sqrt{k_x^2 - \epsilon_1\,\frac{\omega^2}{c^2}}, \tag{C.6}$$

$$k_{2z} = -\,i\,\beta_2 \equiv -\,i\,\sqrt{k_x^2 - \epsilon_2\,\frac{\omega^2}{c^2}}, \tag{C.7}$$

$$k_{3z} = -\,i\,\beta_3 \equiv -\,i\,\sqrt{k_x^2 - \epsilon_3\,\frac{\omega^2}{c^2}}. \tag{C.8}$$

The choices made for k_{1z} and k_{3z} ensure wave confinement, while the sign chosen for k_{2z} is conventional and does not affect the result.

In a more compact form, the system can be written as:

$$\left(\begin{array}{c|c} A & B \\ \hline C & D \end{array}\right)\begin{pmatrix} \mathcal{E}_x^3 \\ \mathcal{E}_x^{2+} \\ \mathcal{E}_x^{2-} \\ \mathcal{E}_x^1 \\ \mathcal{E}_y^3 \\ \mathcal{E}_y^{2+} \\ \mathcal{E}_y^{2-} \\ \mathcal{E}_y^1 \end{pmatrix} = \begin{pmatrix} 0 \\ 0 \\ 0 \\ 0 \\ 0 \\ 0 \\ 0 \\ 0 \end{pmatrix},$$

where

$$A = \begin{bmatrix} -1 & 1 & 1 & 0 \\ \frac{\epsilon_3}{\beta_3} + \frac{i\,\sigma_{xx}^L}{\epsilon_0\,\omega} & -\frac{\epsilon_2}{\beta_2} & \frac{\epsilon_2}{\beta_2} & 0 \\ 0 & \frac{\epsilon_2}{\beta_2}\,e^{\beta_2 d} & -\frac{\epsilon_2}{\beta_2}\,e^{-\beta_2 d} & \left(\frac{\epsilon_1}{\beta_1} + \frac{i\,\sigma_{xx}^R}{\epsilon_0\,\omega}\right) e^{-\beta_1 d} \\ 0 & e^{\beta_2 d} & e^{-\beta_2 d} & -e^{-\beta_1 d} \end{bmatrix},$$

$$B = \begin{bmatrix} 0 & 0 & 0 & 0 \\ \frac{i\,\sigma_{xy}^L}{\epsilon_0\,\omega} & 0 & 0 & 0 \\ 0 & 0 & 0 & \frac{i\,\sigma_{xy}^R}{\epsilon_0\,\omega} e^{-\beta_1 d} \\ 0 & 0 & 0 & 0 \end{bmatrix}, \qquad C = \begin{bmatrix} 0 & 0 & 0 & 0 \\ -i\mu_0\omega\sigma_{yx}^L & 0 & 0 & 0 \\ 0 & 0 & 0 & -i\mu_0\omega\sigma_{yx}^R e^{-\beta_1 d} \\ 0 & 0 & 0 & 0 \end{bmatrix},$$

$$D = \begin{bmatrix} -1 & 1 & 1 & 0 \\ \beta_3 - i\mu_0\omega\sigma_{yy}^L & -\beta_2 & \beta_2 & 0 \\ 0 & \beta_2\,e^{\beta_2 d} & -\beta_2\,e^{-\beta_2 d} & \left(\beta_1 - i\mu_0\omega\sigma_{yy}^R\right) e^{-\beta_1 d} \\ 0 & e^{\beta_2 d} & e^{-\beta_2 d} & -e^{-\beta_1 d} \end{bmatrix}.$$

The block structure of the matrix immediately illustrates a key physical point: in the absence of Hall response ($\sigma_{xy} = \sigma_{yx} = 0$), the off-diagonal blocks B and C vanish, and the TE and TM sectors decouple completely. The matrix A then governs the dispersion of TM modes, while the matrix D governs that of TE modes. As soon as $\sigma_{xy} \neq 0$, however, the blocks B and C become nonzero and the determinant no longer factorizes, signaling the intrinsic TE–TM mixing induced by the anisotropic conductivity.

The cancellation of the determinant of the 8×8 matrix gives the dispersion relation of the eigenmodes of the system, shown in Eq. (4.36).

To check some limiting cases, let us briefly see what happens to Eq. (4.36) for the TE and TM modes separately, in the case of $\sigma_{xy}^{R/L} = 0$.

- **TM case:** $\det[A] = 0$ implies

$$e^{-2\beta_2 d}\left(\frac{\epsilon_1}{\beta_1} - \frac{\epsilon_2}{\beta_2} + \frac{i\sigma_{xx}^R}{\epsilon_0\omega}\right)\left(\frac{\epsilon_3}{\beta_3} - \frac{\epsilon_2}{\beta_2} + \frac{i\sigma_{xx}^L}{\epsilon_0\omega}\right) = \left(\frac{\epsilon_1}{\beta_1} + \frac{\epsilon_2}{\beta_2} + \frac{i\sigma_{xx}^R}{\epsilon_0\omega}\right)\left(\frac{\epsilon_3}{\beta_3} + \frac{\epsilon_2}{\beta_2} + \frac{i\sigma_{xx}^L}{\epsilon_0\omega}\right).$$

  In the limit $d \to \infty$ the coupling factor $e^{-2\beta_2 d}$ vanishes, and, as expected, the dispersion equation decouples into the two equations for the individual interfaces [Bludov et al., 2013].

- **TE case:** $\det[D] = 0$ implies

$$e^{-2\beta_2 d}\left(\beta_3 - \beta_2 - i\mu_0\omega\sigma_{yy}^L\right)\left(\beta_1 - \beta_2 - i\mu_0\omega\sigma_{yy}^R\right) = \left(\beta_3 + \beta_2 - i\mu_0\omega\sigma_{yy}^L\right)\left(\beta_1 + \beta_2 - i\mu_0\omega\sigma_{yy}^R\right).$$

  Again, in the limit $d \to \infty$ the dispersion equation decouples into the two equations for the individual interfaces [Bludov et al., 2013].

Bibliography

Agranovich, Vladimir M. and Vitaly Ginzburg (1984). *Crystal Optics with Spatial Dispersion and Excitons*. URL: https://api.semanticscholar.org/CorpusID:117065552.

Agranovich, V.M. and Yu.N. Gartstein (2009). "Electrodynamics of metamaterials and the Landau–Lifshitz approach to the magnetic permeability". In: *Metamaterials* 3.1, pp. 1–9. ISSN: 1873-1988. DOI: https://doi.org/10.1016/j.metmat.2009.02.002.

Akahane, Y. et al. (2003). "High-Q photonic nanocavity in a two-dimensional photonic crystal". In: *Nature* 425.6961, pp. 944–947. DOI: 10.1038/nature02063.

Akjouj, Abdellatif et al. (Jan. 2021). "Optical Tamm states in semiinfinite layered photonic crystals". In: pp. 489–527. ISBN: 9780128193884. DOI: 10.1016/B978-0-12-819388-4.00029-0.

Alagappan, G. et al. (Jan. 2006a). "One-dimensional anisotropic photonic crystal with a tunable bandgap". In: *Journal of The Optical Society of America B-optical Physics* 23. DOI: 10.1364/JOSAB.23.000159.

Alagappan, G et al. (Sept. 2006b). "Symmetry properties of two-dimensional anisotropic photonic crystals". In: *Journal of the Optical Society of America. A, Optics, image science, and vision* 23, pp. 2002–13. DOI: 10.1364/JOSAA.23.002002.

Alexander, Furs and Leonid Barkovsky (2006). "A new type of surface polaritons at the interface of the magnetic gyrotropic media". In: *Journal of Physics A: Mathematical and Theoretical* 40.2, p. 309. DOI: 10.1088/1751-8113/40/2/010.

— (Apr. 2008). "Surface Polaritons at the Planar Interface of Twinned Dielectric Gyrotropic Media". In: *Electromagnetics* 28, pp. 146–161. DOI: 10.1080/02726340801921452.

Ali, Asif, Abhijit Mitra, and Brahim Aïssa (2022). "Metamaterials and Metasurfaces: A Review from the Perspectives of Materials, Mechanisms and Advanced Metadevices". In: *Nanomaterials* 12.6, p. 1027. DOI: 10.3390/nano12061027.

Altman, C. and K. Suchy (Jan. 2011). *Reciprocity, Spatial Mapping and Time Reversal in Electromagnetics*. DOI: 10.1007/978-94-007-1530-1.

Andberger, Johan et al. (2024). "Terahertz chiral subwavelength cavities breaking time-reversal symmetry via ultrastrong light–matter interaction". In: *Phys. Rev. B* 109, p. L161302. DOI: 10.1103/PhysRevB.109.L161302.

Anker, Jeffrey N. et al. (2008). "Biosensing with plasmonic nanosensors". In: *Nature Materials* 7, pp. 442–453. DOI: 10.1038/nmat2162.

Arlouski, Aliaksandr and Andrey Novitsky (Feb. 2024). "Planar Bilayer PT-Symmetric Systems and Resonance Energy Transfer". In: *Photonics* 11, p. 169. DOI: 10.3390/photonics11020169.

Artmann, K. (1948). "Berechnung der Seitenversetzung des totalreflektierten Strahles". In: *Annalen der Physik* 437.1-2, pp. 87–102. DOI: https://doi.org/10.1002/andp.19484370108.

Asadchy, Viktar S. et al. (2020). "Tutorial on Electromagnetic Nonreciprocity and its Origins". In: *Proceedings of the IEEE* 108.10, pp. 1684–1727. DOI: 10.1109/JPROC.2020.3012381.

Azzam, R. M. A. and N. M. Bashara (1977). *Ellipsometry and Polarized Light*. Amsterdam: North-Holland. ISBN: 9780444850034.

Bacciconi, Zeno et al. (2025). "Theory of Fractional Quantum Hall Liquids Coupled to Quantum Light and Emergent Graviton-Polaritons". In: *Physical Review X* 15, p. 021027. DOI: 10.1103/PhysRevX.15.021027.

Bang, S., S. So, and J. Rho (2019). "Realization of broadband negative refraction in visible range using vertically stacked hyperbolic metamaterials". In: *Scientific Reports* 9, p. 14093. DOI: 10.1038/s41598-019-50434-3.

Barnes, William (Aug. 2016). "Particle plasmons: Why shape matters". In: *American Journal of Physics* 84, pp. 593–601. DOI: 10.1119/1.4948402.

Barvestani, Jamal, M. Kalafi, and A. Vala (Nov. 2007). "Surface Optical Waves in Semi-Infinite One-Dimensional Photonic Crystals Containing Alternating Layers of Positive and Negative Media with a Cap Layer". In: *Acta Physica Polonica A - ACTA PHYS POL A* 112. DOI: 10.12693/APhysPolA.112.1089.

Bashiri, J. et al. (Aug. 2019). "Bloch surface waves engineering in one-dimensional photonic crystals with a chiral cap layer". In: *Journal of the Optical Society of America B* 36, p. 2106. DOI: 10.1364/JOSAB.36.002106.

Belov, P. A. et al. (2003). "Strong spatial dispersion in wire media in the very large wavelength limit". In: *Phys. Rev. B* 67 (11), p. 113103. DOI: 10.1103/PhysRevB.67.113103.

Berreman, Dwight (Apr. 1972). "Optics in Stratified and Anisotropic Media: 4×4 Matrix Formulation". In: *Journal of The Optical Society of America* 62. DOI: 10.1364/JOSA.62.000502.

Bludov, Yuliy et al. (Apr. 2013). "A PRIMER ON SURFACE PLASMON-POLARITONS IN GRAPHENE". In: *International Journal of Modern Physics B* 27. DOI: 10.1142/S0217979213410014.

Bogdanov, Andrey and R.A. Suris (Sept. 2012). "Effect of the anisotropy of a conducting layer on the dispersion law of electromagnetic waves in layered metal-dielectric structures". In: *JETP Letters* 96. DOI: 10.1134/S0021364012130036.

Born, Max and Emil Wolf (2019). *Principles of Optics*. 7th (expanded) ed. See Ch. 15: Optics of Crystals. Cambridge University Press. ISBN: 9781108477437.

Boyd, Robert W. (2008). *Nonlinear Optics, Third Edition*. 3rd. USA: Academic Press, Inc. ISBN: 0123694701.

Brar, Victor W. et al. (2014). "Hybrid Surface-Phonon-Plasmon Polariton Modes in Graphene/Monolayer h-BN Heterostructures". In: *Nano Letters* 14.7. PMID: 24874205, pp. 3876–3880. DOI: 10.1021/nl501096s.

Buddhiraju, Siddharth et al. (2020). "Nonreciprocal Metamaterial Obeying Time-Reversal Symmetry". In: *Phys. Rev. Lett.* 124 (25), p. 257403. DOI: 10.1103/PhysRevLett.124.257403.

Caldwell, J. D. et al. (2014). "Sub-diffractional, volume-confined polaritons in the natural hyperbolic material hexagonal boron nitride". In: *Nature Communications* 5, p. 5221. DOI: 10.1038/ncomms6221.

Caloz, Christophe et al. (2018). "Electromagnetic Nonreciprocity". In: *Phys. Rev. Appl.* 10 (4), p. 047001. DOI: 10.1103/PhysRevApplied.10.047001.

Camley, R.E. (1987). "Nonreciprocal surface waves". In: *Surface Science Reports* 7.3, pp. 103–187. ISSN: 0167-5729. DOI: https://doi.org/10.1016/0167-5729(87)90006-9.

Chebykin, A. V. et al. (2011). "Nonlocal effective medium model for multilayered metal-dielectric metamaterials". In: *Phys. Rev. B* 84 (11), p. 115438. DOI: 10.1103/PhysRevB.84.115438.

Cheng, D.K. and Jin-Au Kong (1968). "Covariant descriptions of bianisotropic media". In: *Proceedings of the IEEE* 56.3, pp. 248–251. DOI: 10.1109/PROC.1968.6268.

Cho, Hanlyun et al. (Sept. 2021). "Experimental demonstration of broadband negative refraction at visible frequencies by critical layer thickness analysis in a vertical hyperbolic metamaterial". In: *Nanophotonics* 10, p. 000010151520210337. DOI: 10.1515/nanoph-2021-0337.

Chochol, Jan et al. (Sept. 2016). "Magneto-optical properties of InSb for terahertz applications". In: *AIP Advances* 6. DOI: 10.1063/1.4968178.

Cognée, K. G. et al. (2019). "Mapping complex mode volumes with cavity perturbation theory". In: *Optica* 6.3, pp. 269–273. DOI: 10.1364/OPTICA.6.000269. URL: https://opg.optica.org/optica/abstract.cfm?URI=optica-6-3-269.

Cojocaru, E. (2015). "Dyakonov hybrid surface waves at the isotropic-biaxial media interface". In: *J. Opt. Soc. Am. A* 32.5, pp. 782–789. DOI: 10.1364/JOSAA.32.000782.

Collin, Robert E. (2004). "Hertzian dipole radiation over a lossy earth or sea: some early and late 20th-century controversies". In: *IEEE Antennas and Propagation Magazine* 46.2, pp. 64–79. DOI: 10.1109/MAP.2004.1305535.

Costa, Joao T., Mario G. Silveirinha, and Andrea Alù (2011). "Poynting vector in negative-index metamaterials". In: *Phys. Rev. B* 83 (16), p. 165120. DOI: 10.1103/PhysRevB.83.165120.

Crassee, Iris et al. (2011). "Giant Faraday rotation in single- and multilayer graphene". In: *Nature Physics* 7.1, pp. 48–51. DOI: 10.1038/nphys1816.

Crossley, W. A. and G. W. Day (1969). "Faraday Rotation in Rare-Earth Iron Garnets". In: *Physical Review* 181.3, pp. 896–905. DOI: 10.1103/PhysRev.181.896.

Dai, S. et al. (2015). "Subdiffractional focusing and guiding of polaritonic rays in a natural hyperbolic material". In: *Nature Communications* 6, p. 6963. DOI: 10.1038/ncomms7963.

Dubinov, Alexander et al. (Apr. 2011). "Terahertz surface plasmons in optically pumped graphene structures". In: *Journal of physics: Condensed matter* 23, p. 145302. DOI: 10.1088/0953-8984/23/14/145302.

D'yakonov, M. I. (1988). "New type of electromagnetic wave propagating at an interface". In: *Soviet Physics JETP* 67.4, pp. 714–716.

Dyakonov, Michel (Jan. 1988). "New type of electromagnetic wave propagating at an interface". In: *Journal of Experimental and Theoretical Physics* 94, p. 119.

Fabrizio, Mauro and Angelo Morro (June 2003). *Electromagnetism of Continuous Media: Mathematical Modelling and Applications*. Oxford University Press. DOI: 10.1093/acprof:oso/9780198527008.001.0001.

Feng, Liang, Ramy El-Ganainy, and Li Ge (Dec. 2017). "Non-Hermitian photonics based on parity–time symmetry". In: *Nature Photonics* 11.12, pp. 752–762. DOI: 10.1038/s41566-017-0031-1.

Feng, Shuai et al. (2005). "Sensitivity of surface states to the stack sequence of one-dimensional photonic crystals". In: *Journal of Optics A: Pure and Applied Optics* 7.8, p. 374. DOI: 10.1088/1464-4258/7/8/004.

Ferrari, Lorenzo et al. (Nov. 2014). "Hyperbolic metamaterials and their applications". In: *Progress in Quantum Electronics* 40. DOI: 10.1016/j.pquantelec.2014.10.001.

Fesenko, Volodymyr et al. (June 2008). "One-dimensional anisotropic photonic crystals based on anisotropic porous silicon". In: pp. 457–459. ISBN: 978-1-4244-2284-5. DOI: 10.1109/MMET.2008.4581029.

Forcella, Davide, Claire Prada, and Rémi Carminati (2017). "Causality, Nonlocality, and Negative Refraction". In: *Phys. Rev. Lett.* 118 (13), p. 134301. DOI: 10.1103/PhysRevLett.118.134301.

Garcia-Vidal, F. J., C. Ciuti, and T. W. Ebbesen (2021). "Manipulating Matter by Strong Coupling to Vacuum Fields". In: *Science* 373.6551, eabd0336. DOI: 10.1126/science.abd0336.

Gérard, Jean-Michel (2003). "Solid-State Cavity-Quantum Electrodynamics with Self-Assembled Quantum Dots". In: *Single Quantum Dots: Fundamentals, Applications, and New Concepts*. Berlin, Heidelberg: Springer Berlin Heidelberg, pp. 269–314. ISBN: 978-3-540-39180-7. DOI: 10.1007/978-3-540-39180-7_7. URL: https://doi.org/10.1007/978-3-540-39180-7_7.

Girvin, S. M., A. H. MacDonald, and P. M. Platzman (1986). "Magneto-Roton Theory of Collective Excitations in the Fractional Quantum Hall Effect". In: *Physical Review B* 33, pp. 2481–2494. DOI: 10.1103/PhysRevB.33.2481.

Golenitskii, Kirill, Kirill Koshelev, and Andrey Bogdanov (June 2016). "Tamm-Langmuir surface waves". In: *Physical Review A* 94. DOI: 10.1103/PhysRevA.94.043815.

Goos, F. and H. Hänchen (1947). "Ein neuer und fundamentaler Versuch zur Totalreflexion". In: *Annalen der Physik* 436.7-8, pp. 333–346. DOI: 10.1002/andp.19474360704.

Gorlach, Maxim A. and Pavel A. Belov (2014). "Effect of spatial dispersion on the topological transition in metamaterials". In: *Phys. Rev. B* 90 (11), p. 115136. DOI: 10.1103/PhysRevB.90.115136.

Grecu, D. (1973). "Plasma Frequency of the Electron Gas in Layered Structures". In: *Phys. Rev. B* 8 (5), pp. 1958–1961. DOI: 10.1103/PhysRevB.8.1958.

Halas, N. J. (2010). "Plasmonics: An Emerging Field Fostered by Nano Letters". In: *Nano Letters* 10.10, pp. 3816–3822. DOI: 10.1021/nl1032342.

Haldane, F. D. M. (1983). "Fractional Quantization of the Hall Effect: A Hierarchy of Incompressible Quantum Fluid States". In: *Physical Review Letters* 51, pp. 605–608. DOI: 10.1103/PhysRevLett.51.605.

— (2011). "Geometrical Description of the Fractional Quantum Hall Effect". In: *Physical Review Letters* 107, p. 116801. DOI: 10.1103/PhysRevLett.107.116801.

Hasan, M. Z. and C. L. Kane (2010). "Colloquium: Topological insulators". In: *Rev. Mod. Phys.* 82 (4), pp. 3045–3067. DOI: 10.1103/RevModPhys.82.3045.

He, Jinlong, Jin Yi, and Sailing He (2006). "Giant negative Goos-Hänchen shifts for a photonic crystal with a negative effective index". In: *Opt. Express* 14.7, pp. 3024–3029. DOI: 10.1364/OE.14.003024.

Homola, Jiří (2008). "Surface plasmon resonance sensors for detection of chemical and biological species". In: *Chemical Reviews* 108.2, pp. 462–493. DOI: 10.1021/cr068107d.

Hu, Bin, Ying Zhang, and Qi Wang (Nov. 2015). "Surface magneto plasmons and their applications in the infrared frequencies". In: *Nanophotonics* 4. DOI: 10.1515/nanoph-2014-0026.

Huang, Hui et al. (Jan. 2007). "Surface modes at the interfaces between isotropic media and uniaxial plasma". In: *Progress In Electromagnetics Research* 76. DOI: 10.2528/PIER07062005.

Imada, M. et al. (1999). "Coherent two-dimensional lasing action in surface-emitting photonic crystal lasers". In: *Applied Physics Letters* 75.2, pp. 316–318. DOI: 10.1063/1.124361.

Inoue, Kuon and Kazuo Ohtaka (Jan. 2004). *Photonic Crystals: Physics, Fabrication and Applications*. Vol. 94. ISBN: 978-3-642-05816-5. DOI: 10.1007/978-3-540-40032-5.

Iorsh, I. et al. (Nov. 2012). "Hyperbolic metamaterials based on multilayer graphene structures". In: *Physical Review B* 87. DOI: 10.1103/PhysRevB.87.075416.

Jackson, John David (1999). *Classical Electrodynamics*. 3rd. New York: Wiley. ISBN: 978-0-471-30932-1.

Jacob, Z., L. V. Alekseyev, and E. Narimanov (2006). "Optical hyperlens: far-field imaging beyond the diffraction limit". In: *Optics Express* 14, pp. 8247–8256. DOI: 10.1364/OE.14.008247.

Jacob, Z. et al. (2010). "Engineering photonic density of states using metamaterials". In: *Applied Physics B* 100, pp. 215–218. DOI: 10.1007/s00340-010-4096-5.

Jacob, Zubin and Evgenii E. Narimanov (2008). "Optical hyperspace for plasmons: Dyakonov states in metamaterials". In: *Applied Physics Letters* 93.22, p. 221109. DOI: 10.1063/1.3037208.

Jain, J. K. (1989). "Composite-Fermion Approach for the Fractional Quantum Hall Effect". In: *Physical Review Letters* 63, pp. 199–202. DOI: 10.1103/PhysRevLett.63.199.

Jalas, Dirk et al. (2013). "What is—and what is not—an optical isolator". In: *Nature Photonics* 7.8, pp. 579–582. DOI: 10.1038/nphoton.2013.185.

Jangal, F. et al. (Jan. 2016). "Observation of Zenneck-Like Waves over a Metasurface Designed for Launching HF Radar Surface Wave". In: *International Journal of Antennas and Propagation* 2016, pp. 1–5. DOI: 10.1155/2016/6184959.

Joannopoulos, J. D. et al. (2008). *Photonic Crystals: Molding the Flow of Light*. 2nd ed. Princeton University Press. DOI: 10.2307/j.ctvcm4gz9.1.

John, S. (1987). "Strong localization of photons in certain disordered dielectric superlattices". In: *Physical Review Letters* 58.23, pp. 2486–2489. DOI: 10.1103/PhysRevLett.58.2486.

Kavokin, A., I. Shelykh, and G. Malpuech (2005). "Optical Tamm states for the fabrication of polariton lasers". In: *Applied Physics Letters* 87.26, p. 261105. DOI: 10.1063/1.2136414.

Kidwai, O., S. V. Zhukovsky, and J. E. Sipe (2012). "Effective-medium approach to planar multilayer hyperbolic metamaterials: strengths and limitations". In: *Physical Review A* 85, p. 053842. DOI: 10.1103/PhysRevA.85.053842.

Kim, Minhyung (2015). "Metamaterials and Imaging". In: *Nano Convergence* 2.14, pp. 1–13. DOI: 10.1186/s40580-015-0053-7.

Kim, Sunnam and Seiji Kurihara (Apr. 2018). "Liquid Crystals for Responsible Photonic Crystals". In: ISBN: 978-953-51-3961-4. DOI: 10.5772/intechopen.72654.

Knight, J. C. (2003). "Photonic crystal fibres". In: *Nature* 424.6950, pp. 847–851. DOI: 10.1038/nature01940.

Kong, Jin Au (1970). "Reciprocity relationships for bianisotropic media". In: *Proceedings of the IEEE* 58.12, pp. 1966–1967. DOI: 10.1109/PROC.1970.8079.

— (1972). "Theorems of bianisotropic media". In: *Proceedings of the IEEE* 60.9, pp. 1036–1046. DOI: 10.1109/PROC.1972.8851.

Kosaka, H. et al. (1998). "Superprism phenomena in photonic crystals". In: *Physical Review B* 58.16, R10096–R10099. DOI: 10.1103/PhysRevB.58.R10096.

Koshelev, K. L. and A. A. Bogdanov (2015). "Temperature-tunable semiconductor metamaterial". In: *Phys. Rev. B* 92 (8), p. 085305. DOI: 10.1103/PhysRevB.92.085305.

Kou, Liangzhi et al. (Apr. 2017). "Two Dimensional Topological Insulators: Progress and Prospects". In: *The journal of physical chemistry letters* 8. DOI: 10.1021/acs.jpclett.7b00222.

Krishnamoorthy, H. N. S. et al. (2012). "Topological transitions in metamaterials". In: *Science* 336, pp. 205–209. DOI: 10.1126/science.1219171.

Kushwaha, Manvir S. (2001). "Plasmons and magnetoplasmons in semiconductor heterostructures". In: *Surface Science Reports* 41.1, pp. 1–416. ISSN: 0167-5729. DOI: https://doi.org/10.1016/S0167-5729(00)00007-8. URL: https://www.sciencedirect.com/science/article/pii/S0167572900000078.

Lai, H. M. and S. W. Chan (2002). "Large and negative Goos–Hänchen shift near the Brewster dip on reflection from weakly absorbing media". In: *Opt. Lett.* 27.9, pp. 680–682. DOI: 10.1364/OL.27.000680.

Lakhtakia, Akhlesh, Tom Mackay, and Chenzhang Zhou (Sept. 2020). "Electromagnetic surface waves at exceptional points". In: *European Journal of Physics* 42. DOI: 10.1088/1361-6404/abb6c7.

Landau, L. D. and E. M. Lifshitz (1984). *Electrodynamics of Continuous Media*. Pergamon.

Lannebère, Sylvain et al. (2025). "Chiral-Gain Photonics". In: *Laser & Photonics Reviews* 19.7, p. 2400881. DOI: https://doi.org/10.1002/lpor.202400881.

Laughlin, R. B. (1983). "Anomalous Quantum Hall Effect: An Incompressible Quantum Fluid with Fractionally Charged Excitations". In: *Physical Review Letters* 50, pp. 1395–1398. DOI: 10.1103/PhysRevLett.50.1395.

Lee, M. and P. M. Fauchet (2007). "Two-dimensional silicon photonic crystal based biosensing platform for protein detection". In: *Optics Express* 15.8, pp. 4530–4535. DOI: 10.1364/OE.15.004530.

Levy, Miguel et al. (2019). "Faraday rotation in iron garnet films beyond elemental substitution". In: *Optica* 6.5, pp. 642–650. DOI: 10.1364/OPTICA.6.000642.

Li, P. et al. (2015). "Hyperbolic phonon-polaritons in boron nitride for near-field optical imaging and focusing". In: *Nature Communications* 6, p. 7507. DOI: 10.1038/ncomms8507.

Liang, Jiehui et al. (2024). "Evidence for Chiral Graviton Modes in Fractional Quantum Hall Liquids". In: *Nature* 628.8006, pp. 78–83. DOI: 10.1038/s41586-024-07201-w.

Lindell, Ismo et al. (1994). *Electromagnetic waves in chiral and bi-isotropic media*. English. United Kingdom: Artech House. ISBN: 9780890066843.

Lindell, Ismo V. (1992). *Methods for Electromagnetic Field Analysis*. New York: IEEE Press. ISBN: 978-0-7803-1024-2.

Liou, Shiuan-Fan et al. (2019). "Chiral Gravitons in Fractional Quantum Hall Liquids". In: *Physical Review Letters* 123, p. 146801. DOI: 10.1103/PhysRevLett.123.146801.

Lipworth, Gabriel et al. (2014). "Magnetic Metamaterial Superlens for Increased Range Wireless Power Transfer". In: *Scientific Reports* 4, p. 3642. DOI: 10.1038/srep03642.

Liscidini, Marco and J. E. Sipe (2009). "Analysis of Bloch-surface-wave assisted diffraction-based biosensors". In: *Journal of the Optical Society of America B* 26.2, pp. 279–289. DOI: 10.1364/JOSAB.26.000279.

Liu, Zhaowei et al. (2007). "Far-Field Optical Hyperlens Magnifying Sub-Diffraction-Limited Objects". In: *Science* 315.5819, p. 1686. DOI: 10.1126/science.1137368.

Locarno, Marco and Daan Brinks (July 2023). "Analytical calculation of plasmonic resonances in metal nanoparticles: A simple guide". In: *American Journal of Physics* 91.7, pp. 538–546. ISSN: 0002-9505. DOI: 10.1119/5.0094967. eprint: https:

//pubs.aip.org/aapt/ajp/article-pdf/91/7/538/20105217/538_1_5.0094967.pdf. URL: https://doi.org/10.1119/5.0094967.

Luo, C. et al. (2004). "All-angle negative refraction without negative index". In: *Science* 305.5685, pp. 847–848. DOI: 10.1103/PhysRevB.65.201104.

Mackay, Tom G. and Akhlesh Lakhtakia (2019). *Electromagnetic Anisotropy and Bianisotropy*. DOI: https://doi.org/10.1142/11351.

Maier, Stefan A. (2007). *Plasmonics: Fundamentals and Applications*. New York: Springer. ISBN: 9780387331508. DOI: 10.1007/0-387-37825-1.

Manzoor, Khawer et al. (May 2022). "Goos–Hänchen shift observed from stratified medium". In: *The European Physical Journal D* 76. DOI: 10.1140/epjd/s10053-022-00409-3.

Martorell, J., D. Sprung, and G. Morozov (2006). "Surface TE waves on 1D photonic crystals". In: *Journal of Optics A: Pure and Applied Optics* 8.8, p. 630. DOI: 10.1088/1464-4258/8/8/003.

Mekis, A. et al. (1996). "High transmission through sharp bends in photonic crystal waveguides". In: *Physical Review Letters* 77.18, pp. 3787–3790. DOI: 10.1103/PhysRevLett.77.3787.

Melrose, D. B. and R. C. McPhedran (1991). *Electromagnetic Processes in Dispersive Media*. DOI: https://doi.org/10.1017/CBO9780511600036.

Moncada-Villa, E., A. Fernández-Domínguez, and Juan Cuevas (Apr. 2019). "Magnetic-field controlled anomalous refraction in doped semiconductors". In: *Journal of the Optical Society of America B* 36, p. 935. DOI: 10.1364/JOSAB.36.000935.

Narimanov, Evgenii E. (2014). "Photonic Hypercrystals". In: *Phys. Rev. X* 4 (4), p. 041014. DOI: 10.1103/PhysRevX.4.041014.

Nefedov, Igor and L. Melnikov (June 2015). "Plasmonic Terahertz Amplification in Graphene-Based Asymmetric Hyperbolic Metamaterial". In: *Photonics* 2, pp. 594–603. DOI: 10.3390/photonics2020594.

Nefedov, Igor et al. (Sept. 2013). "Total absorption in asymmetric hyperbolic media". In: *Scientific reports* 3, p. 2662. DOI: 10.1038/srep02662.

Noda, S. et al. (2000). "Full three-dimensional photonic band-gap crystals at near-infrared wavelengths". In: *Science* 289.5479, pp. 604–606. DOI: 10.1126/science.289.5479.604.

Nosich, Alexander (Mar. 1994). "Radiation Conditions, Limiting Absorption Principle and General Relations in Open Waveguide Scattering". In: *Journal of Electromagnetic Waves and Applications - J ELECTROMAGNET WAVE APPLICAT* 8, pp. 329–353. DOI: 10.1163/156939394X00902.

Notomi, M. (2000). "Theory of light propagation in strongly modulated photonic crystals: Refraction-like behavior in the vicinity of the photonic band gap". In: *Physical Review B* 62.16, pp. 10696–10705. DOI: 10.1103/PhysRevB.62.10696.

Oruganti, Sai et al. (Jan. 2020). "Experimental Realization of Zenneck Type Wave-based Non-Radiative, Non-Coupled Wireless Power Transmission". In: *Scientific Reports* 10, p. 925. DOI: 10.1038/s41598-020-57554-1.

Painter, O. et al. (1999). "Two-dimensional photonic band-gap defect mode laser". In: *Science* 284.5411, pp. 1819–1821. DOI: 10.1126/science.284.5421.1819.

Parimi, P. V. et al. (2003). "Imaging by flat lens using negative refraction in photonic crystals". In: *Nature* 426.6965, pp. 404–404. DOI: 10.1038/426404a.

Pellegrini, Giovanni et al. (2016). "Magnetoplasmonics". In: DOI: 10.1007/978-94-017-9780-1_100980.

Pendry, John B. (2000). "Negative Refraction Makes a Perfect Lens". In: *Physical Review Letters* 85.18, pp. 3966–3969. DOI: 10.1103/PhysRevLett.85.3966.

Pendry, John B., Luis Martín-Moreno, and Francisco J. García-Vidal (2004). "Mimicking Surface Plasmons with Structured Surfaces". In: *Science* 305.5685, pp. 847–848. DOI: 10.1126/science.1098999.

Plum, E. et al. (2009). "Metamaterial with negative index due to chirality". In: *Physical Review B* 79.3, p. 035407. DOI: 10.1103/PhysRevB.79.035407.

Poddubny, A. et al. (2013). "Hyperbolic metamaterials". In: *Nature Photonics* 7, pp. 948–957. DOI: 10.1038/nphoton.2013.243.

Polo, J. A. and Akhlesh Lakhtakia (Mar. 2011). "Surface electromagnetic waves: A review". In: *Laser & Photonics Reviews* 5, pp. 234 –246. DOI: 10.1002/lpor.200900050.

Polo, J. A., Sudarshan Nelatury, and Akhlesh Lakhtakia (Oct. 2007). "Surface waves at a biaxial bicrystalline interface". In: *Journal of the Optical Society of America A* 24, pp. 2974–9. DOI: 10.1364/JOSAA.24.002974.

Polo, J.A., T. Mackay, and Akhlesh Lakhtakia (May 2013). "Electromagnetic Surface Waves: A Modern Perspective". In: pp. 1–293.

Prosandeev, Sergey et al. (2013). "Natural optical activity and its control by electric field in electrotoroidic systems". In: *Phys. Rev. B* 87 (19), p. 195111. DOI: 10.1103/PhysRevB.87.195111.

Proskurin, Igor et al. (2017). "Optical chirality in gyrotropic media: symmetry approach". In: *New Journal of Physics* 19.6, p. 063021. DOI: 10.1088/1367-2630/aa6acd.

Provenzano, Daniele B. and Giuseppe C. La Rocca (2023). "Interface mode between gyroelectric and hyperbolic media". In: *J. Opt. Soc. Am. B* 40.1, pp. 172–177. DOI: 10.1364/JOSAB.476753.

— (2024). "Bulk and surface modes in a one-dimensional gyro-uniaxial photonic crystal". In: *Phys. Rev. A* 110 (3), p. 033514. DOI: 10.1103/PhysRevA.110.033514.

Provenzano, Daniele B. et al. (2026). "Chiral quadrupolar optics of fractional quantum Hall liquids". Manuscript in preparation.

Pérez Huerta, Jose et al. (Feb. 2018). "Reflectivity of 1D photonic crystals: A comparison of computational schemes with experimental results". In: *International Journal of Modern Physics B* 32, p. 1850136. DOI: 10.1142/S0217979218501369.

Qing, De-Kui and Gang Chen (2004). "Goos–Hänchen shifts at the interfaces between left- and right-handed media". In: *Opt. Lett.* 29.8, pp. 872–874. DOI: 10.1364/OL.29.000872.

Raether, Heinz (1988). *Surface Plasmons on Smooth and Rough Surfaces and on Gratings*. Vol. 111. Springer Tracts in Modern Physics. Berlin, Heidelberg: Springer. DOI: 10.1007/BFb0048317.

Russell, P. St. J. (2003). "Photonic crystal fibers". In: *Science* 299.5605, pp. 358–362. DOI: 10.1126/science.1079280.

Sakurai, J. J. and Jim Napolitano (2011). *Modern Quantum Mechanics*. 2nd. San Francisco: Addison-Wesley.

Saleh, Bahaa E. A. and Malvin Carl Teich (2019). *Fundamentals of Photonics*. 3rd. Hoboken, NJ: Wiley. ISBN: 9781119506874.

Schulenberger, John R. and Calvin H. Wilcox (1971). "The limiting absorption principle and spectral theory for steady-state wave propagation in inhomogeneous anisotropic media". In: *Archive for Rational Mechanics and Analysis* 41.1, pp. 46–65. DOI: 10.1007/BF00250177.

Scully, Marlan O. and M. Suhail Zubairy (1997). *Quantum Optics*. Cambridge: Cambridge University Press. ISBN: 9780521435956.

Semchenko, Igor V., Sergei Tretyakov, and Anatoly Nickolaevich Serdyukov (1996). "Research on Chiral and Bianisotropic Media in Byelorussia and Russia in the Last Ten Years". In: 12, pp. 335–370. DOI: 10.2528/PIER94112800.

Serdyukov, A. N. et al. (2001a). *Electromagnetics of Bi-Anisotropic Materials: Theory and Applications*. Amsterdam: Gordon and Breach Science Publishers. ISBN: 9789056993276.

Serdyukov, Anatoly et al. (2001b). *Electromagnetics of bi-anisotropic materials: Theory and applications*. English. Gordon and Breach Science Publishers.

Shadrivov, I. V., A. A. Sukhorukov, and Y. S. Kivshar (2003). "Giant Goos–Hänchen effect at the reflection from left-handed metamaterials". In: *Applied Physics Letters* 83.13, pp. 2713–2715. DOI: 10.1063/1.1615678.

Shekhar, Prashant, Jon Atkinson, and Zubin Jacob (Jan. 2014). "Hyperbolic metamaterials: Fundamentals and applications". In: *Nano Convergence* 1. DOI: 10.1186/s40580-014-0014-6.

Sihvola, Ari (1999). *Electromagnetic Mixing Formulas and Applications*. Vol. 47. Electromagnetic Waves Series. London: Institution of Electrical Engineers (IEE). ISBN: 978-0-85296-772-0.

Singh, Rahulkumar Sunil and Prashant K Sarswat (2023). "From fundamentals to applications: The development of magnetoplasmonics for next-generation technologies". In: *Materials Today Electronics* 4, p. 100033. ISSN: 2772-9494. DOI: https://doi.org/10.1016/j.mtelec.2023.100033. URL: https://www.sciencedirect.com/science/article/pii/S2772949423000098.

Skivesen, N. et al. (2007). "Photonic-crystal waveguide biosensor". In: *Optics Express* 15.5, pp. 3169–3176. DOI: 10.1364/OE.15.003169.

Slobozhanyuk, A. P. et al. (2015). "Purcell effect in hyperbolic metamaterial resonators". In: *Physical Review B* 92, p. 195127. DOI: 10.1103/PhysRevB.92.195127.

Smith, D. R., J. B. Pendry, and M. C. K. Wiltshire (2004). "Metamaterials and Negative Refractive Index". In: *Science* 305.5685, pp. 788–792. DOI: 10.1126/science.1096796.

Smith, D. R. and D. Schurig (2004). "Negative refraction in indefinite media". In: *Journal of the Optical Society of America B* 21, pp. 1032–1043. DOI: 10.1364/JOSAB.21.001032.

Soboleva, I. V., V. V. Moskalenko, and A. A. Fedyanin (2012). "Giant Goos-Hänchen Effect and Fano Resonance at Photonic Crystal Surfaces". In: *Phys. Rev. Lett.* 108 (12), p. 123901. DOI: 10.1103/PhysRevLett.108.123901.

Srinivasan, Karthik and Bethanie J. H. Stadler (2022). "Review of integrated magneto-optical isolators with rare-earth iron garnets for polarization diverse and magnet-free isolation in silicon photonics [Invited]". In: *Optical Materials Express* 12.2, pp. 697–716. DOI: 10.1364/OME.447398.

Stockman, M. I. (2011). "Nanoplasmonics: Past, Present, and Glimpse into Future". In: *Optics Express* 19.22, pp. 22029–22106. DOI: 10.1364/OE.19.022029.

Stormer, H. L. (1999). "Nobel Lecture: The Fractional Quantum Hall Effect". In: *Reviews of Modern Physics* 71, pp. 875–889. DOI: 10.1103/RevModPhys.71.875.

Takayama, O, A A Bogdanov, and A V Lavrinenko (2017). "Photonic surface waves on metamaterial interfaces". In: *Journal of Physics: Condensed Matter* 29.46, p. 463001. DOI: 10.1088/1361-648X/aa8bdd.

Takayama, Osamu et al. (2009). "Observation of Dyakonov Surface Waves". In: *Physical Review Letters* 102.4, p. 043903. DOI: 10.1103/PhysRevLett.102.043903.

Toptygin, I. N. and K. Levina (Feb. 2016). "Energy-momentum tensor of the electromagnetic field in dispersive media". In: *Physics Uspekhi* 59.2, pp. 141–152. DOI: 10.3367/UFNe.0186.201602c.0146.

Toptygin, Igor N. (2015). *Electromagnetic Phenomena in Matter*. John Wiley & Sons. DOI: doi.org/10.1002/9783527693474.

Tsui, D. C., H. L. Stormer, and A. C. Gossard (1982). "Two-Dimensional Magnetotransport in the Extreme Quantum Limit". In: *Physical Review Letters* 48, pp. 1559–1562. DOI: 10.1103/PhysRevLett.48.1559.

Veselago, Viktor G. (1968). "The electrodynamics of substances with simultaneously negative values of ϵ and μ." In: *Soviet Physics Uspekhi* 10.4, p. 509. DOI: 10.1070/PU1968v010n04ABEH003699.

Vinogradov, A. et al. (June 2010). "Surface states in photonic crystals". In: *Physics-Uspekhi* 53, p. 243. DOI: 10.3367/UFNe.0180.201003b.0249.

Vytovtov, Konstantin and Lyudmila Mospan (2011). "One-dimensional anisotropic photonic crystal as a key element for nonreciprocal optical devices based not on the Faraday effect". In: *2011 41st European Microwave Conference*, pp. 818–821. DOI: 10.23919/EuMC.2011.6101915.

Wang, Changbiao (2015). "Self-consistent theory for a plane wave in a moving medium and light-momentum criterion". In: *Canadian Journal of Physics* 93.12, pp. 1510–1522. ISSN: 0008-4204. DOI: https://doi.org/10.1139/cjp-2015-0167.

Wang, Li-Gang, Hong Chen, and Shi-Yao Zhu (Nov. 2005). "Large negative Goos–Hänchen shift from a weakly absorbing dielectric slab". In: *Optics Letters* 30, pp. 2936–2938. DOI: 10.1364/OL.30.002936.

Wang, Pengfei, Xiaoqin Zhang, and Minghua Sun (2022). "Molecular Plasmonics with Metamaterials". In: *Chemical Reviews* 122.20, pp. 17681–17727. DOI: 10.1021/acs.chemrev.2c00333.

Wang, Tong-Biao et al. (Aug. 2009). "Electromagnetic surface modes in one-dimensional photonic crystals with dispersive metamaterials". In: *JOSA B* 26, pp. 1635–1640. DOI: 10.1364/JOSAB.26.001635.

Yablonovitch, E. (1987). "Inhibited spontaneous emission in solid-state physics and electronics". In: *Physical Review Letters* 58.20, pp. 2059–2062. DOI: 10.1103/PhysRevLett.58.2059.

Yang, Kun (2024). "Graviton-Like Excitation Observed with Predicted Chirality in Fractional Quantum Hall Liquids". In: *The Innovation* 5.4, p. 100641. DOI: 10.1016/j.xinn.2024.100641.

Yariv, A. and P. Yeh (2002). *Optical Waves in Crystals: Propagation and Control of Laser Radiation*. Wiley Series in Pure and Applied Optics. Wiley. ISBN: 9780471430810.

Yeh, P. (2005). *Optical Waves in Layered Media*. Wiley Series in Pure and Applied Optics. Wiley. ISBN: 9780471731924.

Yeh, Pochi, Amnon Yariv, and Chi-Shain Hong (1977). "Electromagnetic propagation in periodic stratified media. I. General theory". In: *Journal of the Optical Society of America* 67.4, pp. 423–438. DOI: 10.1364/JOSA.67.000423.

Yermakov, O. Y. et al. (2015). "Hybrid waves localized at hyperbolic metasurfaces". In: *Phys. Rev. B* 91 (23), p. 235423. DOI: 10.1103/PhysRevB.91.235423.

Zangwill, Andrew (2012). *Modern Electrodynamics*. Cambridge University Press.

Zayats, Anatoly V., Igor I. Smolyaninov, and Alexei A. Maradudin (2005). "Nano-optics of surface plasmon polaritons". In: *Physics Reports* 408.3–4, pp. 131–314. DOI: 10.1016/j.physrep.2004.11.001.

Zenneck, J. (Mar. 1907). "Über die Fortpflanzung ebener elektromagnetischer Wellen längs einer ebenen Leiterfläche und ihre Beziehung zur drahtlosen Telegraphie". In: *Annalen der Physik* 328, pp. 846 –866. DOI: 10.1002/andp.19073281003.

Zhao, Xiaoying, Yi luo, and Lezhu Zhou (2007). "Study On The Photonic Crystal Made By Gyrotropic Medium". In: *2007 International Nano-Optoelectronics Workshop*, pp. 144–145. DOI: 10.1109/INOW.2007.4302923.

Zhou, Chenzhang, Tom Mackay, and Akhlesh Lakhtakia (July 2020). "Two Dyakonov–Voigt surface waves guided by a biaxial–isotropic dielectric interface". In: *Scientific Reports* 10, p. 12894. DOI: 10.1038/s41598-020-69727-z.

Zvezdin, A. K. and V. A. Kotov (1997). *Modern Magnetooptics and Magnetooptical Materials*. Bristol, UK: Institute of Physics Publishing. ISBN: 9780750303620.

Zyablovsky, A. et al. (Nov. 2014). "PT-symmetry in optics". In: *Physics-Uspekhi* 57, pp. 1063–1082. DOI: 10.3367/UFNe.0184.201411b.1177.